DOCTORAL THESIS:
INTERPRETATION OF THERMAL CONDUCTIVITY AND TOROIDAL MOMENTUM TRANSPORT IN DIII-D TAKING INTO ACCOUNT IOL AND PINCH VELOCITY

A Dissertation
Presented to
The Academic Faculty

By

Jonathan Roveto

In Partial Fulfillment
of the Requirements for the Degree
Doctor of Philosophy in the
George W. Woodruff School of Mechanical Engineering
Nuclear and Radiological Engineering

Georgia Institute of Technology

December 2021

DOCTORAL THESIS:
INTERPRETATION OF THERMAL CONDUCTIVITY AND TOROIDAL MOMENTUM TRANSPORT IN DIII-D TAKING INTO ACCOUNT IOL AND PINCH VELOCITY

Thesis committee:

Dr. Weston M. Stacey
Reagent's Professor
Nuclear and Radiological Engineering
Georgia Institute of Technology

Dr. Dan Kotlyar
Professor
Nuclear and Radiological Engineering
Georgia Institute of Technology

Dr. Steven Biegalski
Professor and Chair
Nuclear and Radiological Engineering
Georgia Institute of Technology

Dr. Theresa Wilks
Research Scientist
Massachusettes Institute of Technology

Dr. Bojan Petrovic
Professor
Nuclear and Radiological Engineering
Georgia Institute of Technology

Dr. Richard Groebner
Research Scientist
General Atomics - DIII-D

Dr. Shaun Haskey
Research Scientist
Princeton Plasma Physics Lab

Date approved: December 1, 2020

I could either watch it happen or be a part of it

Elon Musk

For my parents.

ACKNOWLEDGMENTS

I would like to thank all the members of my thesis committee for their help in preparation of this work and for taking the substantial time required as committee members to complete this process. I'd like to especially thank Dr. Groebner for his advice, help, and fruitful discussions over the years. He provided valuable advice and helped guide the work contained in this dissertation. I'd also like to thank Dr. Wilks for her help and discussions during her time at MIT and as a fellow graduate student at the Fusion Research Center. I'd like to thank Dr. Haskey for providing data and advice from an experimentalist's perspective over the years as well. Most importantly, I'd like to thank my advisor, Dr. Stacey, for his support and advice during my doctoral research as well as his leadership of the Fusion Research Center.

I'd also like to thank Dr. Matthias Knolker and Dr. Xi Chen for providing data on QH-mode and SH-mode shots used in this thesis.

Special thanks are due to the friends and colleagues who made this work possible. I'd like to thank Max Hill, Andrew Bopp, Richard King, and J.P. Floyd for helping me understand the true value of graduate work, as well as all the Moe's Mondays that we enjoyed together.

I'd like to thank my loving girlfriend, Christina Tabor, as well as my parents for their unending love and support throughout this process. The PhD process, at times, is seemingly unending and requires special sacrifices by loved ones, and the support that I have felt has been both unwaivering and unending.

Finally, I'd also like to thank the Starbucks on Johnson Ferry and Paper Mill Rd for letting me work hundreds of hours during many phases of my research in their store while often buying nothing more than a coffee.

TABLE OF CONTENTS

LIST OF TABLES

LIST OF FIGURES

SUMMARY

The objective of this PhD research is to improve the methodology used to interpret the diffusive radial particle flux and the conductive radial heat flux from the experimentally inferred total radial particle and energy fluxes, respectively, in order to more accurately infer experimental values for the heat conductivity and particle diffusion coefficients, respectively. The difficulty lies in the fact that the experimental radial particle, momentum, and energy fluxes are determined by phenomena other than diffusion, viscosity, and conduction, respectively. The contributions of these "other phenomena" must be subtracted from the "experimental" radial fluxes to obtain diffusive radial particle fluxes that can be used to interpret particle diffusivities and conductive radial energy fluxes, which can be used to interpret thermal conductivities.

The improved methodology is employed to interpret particle diffusion and heat conductivity coefficients in several DIII-D shots in different confinement regimes and compare with theoretical models.

The Georgia Tech GTEDGE2 transport interpretation code, with improved Ion Orbit Loss (IOL) models for neutral beam and thermalized ions in the edge plasma, and the GTNEUTPY neutral particle transport code, are applied to several DIII-D shots to enable comparisons of various theoretical particle diffusion coefficient and thermal conductivity models with experiment in multiple operating regimes (L-mode, H-mode, RMP, QH-mode, and SH-mode). GTEDGE2 corrects for non-diffusive radial particle flux contributions and non-conductive radial heat flux contributions (including IOL, the convective outflow of plasma energy, viscous heating, transport of rotational energy, and work done by the flowing plasma against the pressure tensor) when determining the experimental radial particle and heat fluxes.

This code is used in this research to examine differences in these particle diffusion and heat conductivity coefficients among shots in different operating regimes when correcting

for the various non-diffusive and non-conductive phenomena. The experimental results are compared with various theoretical models for particle and energy transport, including neoclassical, ion temperature gradient (ITG) modes, drift-Alfven transport, and gyro-Bohm transport. This research also obtains a toroidal viscous drag and a pinch velocity using IOL-corrected radial particle fluxes, therein demonstrating the importance of non-diffusive particle transport.

We find that the effects of IOL on the interpretation of the radial ion heat flux are significant in the edge plasma. Furthermore, correcting for convective heating and work done by the plasma on the pressure tensor is seen to in general substantially reduce the inferred radial ion conductive heat flux. Importantly, we also find that viscous heating, which is driven by asymmetries in the toroidal and poloidal rotation velocities, can be an important heat transfer mechanism that must be corrected for when inferring transport coefficients. We find that, upon correcting for these non-conductive heat transport mechanisms, some combination of neoclassical and ITG transport may be able to explain ion heat transport in the edge plasma. We also show that the particle pinch is an important driver of transport in the edge plasma. We hope that future research will apply the IOL methodology found in the GTEDGE2 code while also correcting for the above-described non-conductive heat transport phenomena and taking measures to estimate rotational asymmetries to determine the viscous heating, which we believe is an important non-conductive heat transport mechanism.

CHAPTER 1

FUSION OVERVIEW

1.1 Fusion Program

Fusion reactors have the potential to generate large amounts of clean, safe energy from a relatively replenishable source: heavy hydrogen. Einstein's famous formula $E = mc^2$ describes the amount of energy that can be released through, among other things, nuclear fusion. In current fusion research, deuterium and tritium (hydrogen ions with 1 neutron and 2 neutrons, respectively) are the expected fuels for power reactors. For the case of a deuterium ion fusing with a tritium ion to form an alpha particle and a neutron (a "D-T reaction"), the amount of energy released is 17.6 MeV. Of this energy, 3.5 MeV is in the form of kinetic energy of the resulting alpha particle (a helium nucleus with 2 neutrons), and 14.1 MeV is in the form of kinetic energy of the neutron. As shown in Figure 1.1[1], the fusion cross section of the D-T fusion reaction is significantly higher than other potential fusion reactions at temperatures currently achievable ($\lesssim$ 20 keV or approximately $200,000,000°C$). As a result, all fusion reactors currently under development plan to generate fusion primarily via the D-T reaction.

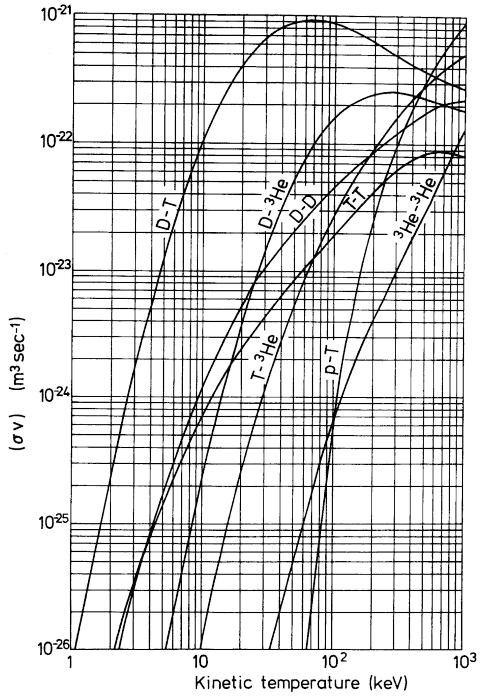

Figure 1.1: Fusion Reactivity, $\langle \sigma v \rangle_{fus}\,(m^3 s^{-1})$. Note that the D-T reaction is the easiest to achieve. Reproduced with permission from [1].

1.2 Tokamaks

This research focuses on the leading *tokamak* reactor concept, in which a heavy hydrogen plasma is confined in the shape of a torus using strong magnetic fields. The term *tokamak* was coined by Igor Golovin [2] and is a transliteration of the russian acronym that stands for either "toroidal chamber with magnetic coils" or "toroidal chamber with axial magnetic fields". Figure 1.2 is a diagram of the important aspects of a tokamak reactor.

Tokamak reactors confine a plasma in a vacuum vessel using magnetic fields. Since the ions and electrons in a plasma are by definition disassociated, they strongly respond to externally applied electric and magnetic fields. In addition, charged particles attempt to follow magnetic field lines. Multiple types of magnetic fields are thus applied to confine

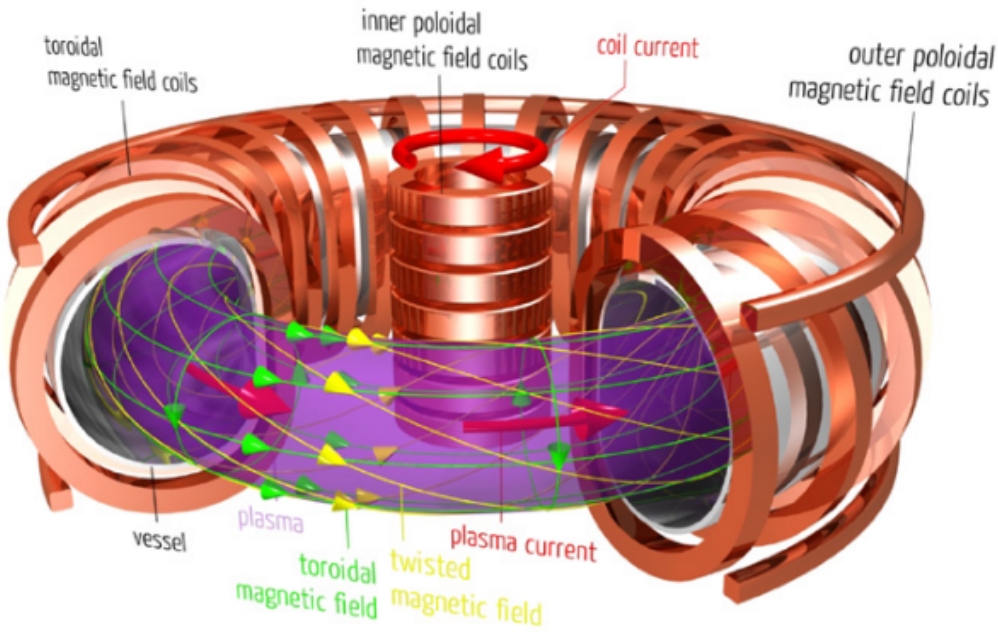

Figure 1.2: Diagram of a tokamak reactor and the important systems, coils, and currents. Reproduced with permission from [3].

the plasma. The strongest of these magnetic fields (on the order of $1 \sim 10$ T) is the toroidal magnetic field (green arrows in Figure 1.2), which is generated by the toroidal magnetic field coils. This strong toroidal magnetic field guides the plasma to remain within the vessel. If these toroidal magnetic field lines were straight, the plasma could be confined indefinitely. However, since the vessel must close on itself, the toroidal field lines must curve following the vessel. From Maxwell's equations, this causes a drifting of the plasma ions and electrons, which ultimately would result in the plasma losing confinement (i.e., plasma ions and electrons impinging on the vessel wall).

This, along with other types of "drifts", necessitates other magnetic fields to improve confinement and performance. As an example, a current is created in the plasma (red arrows

within the plasma in Figure 1.2) by a central solenoid that flows along the plasma. This solenoid-induced current produces a poloidal magnetic field that is superimposed over the toroidal magnetic field. This resulting spiraling magnetic field (yellow arrows in Figure 1.2) confines the plasma within the vessel.

1.3 Plasma Shaping, ELMs, H-mode, and Beyond

It turns out that shaping the plasma can increase the performance of the reactor. Additional outer poloidal magnetic field coils, along with auxilary coils (not picured), are used to position and shape the plasma. It has been found that shaping the plasma in the form of a D can produce improved confinement of the plasma. The shaping can be defined by two parameters: the plasma elongation κ and the (upper and lower) triangularity $\delta^{upper}/\delta^{lower}$.

In the early 1980s, a new regime of tokamak operation was discovered at ASDEX [4]. This new regime, termed H-mode or high-performance/high-confinement mode, in contrast to low-performance/low-confinement mode (L-mode), demonstrated improved plasma confinement and was accessed using high neutral-beam-injected (NBI) [1] power and sufficient densities and temperatures. A key feature of H-mode plasmas is the formation of a "pedestal" near the separatrix, as shown in Figure 1.3. It has been realized that the pedestal structure essentially represents the boundary condition for overall plasma performance and has been the subject of intense research [5]. However, with this improved confinement regime

[1] Neutral beam injectors, abbreviated NBI, accelerate charged atomic and molecular hydrogen (H^2+, H_2^2+, H_3^2+) to high energies ($> 70keV$ at DIII-D) through a so-called "neutralizer" and into the vessel to both fuel and heat the plasma.

comes the problem of edge localized modes (ELMs). A review of ELMs can be found in [6]. Briefly, ELMs are instabilities that result in losses of particles and energy to the tokamak vessel wall, with the greatest heat loads being directed to the divertor plates. Type-I ELMs are characterized by the sudden radial transport of a substantial amount of plasma particles and energy, constituting up to 10-15% of the plasma energy and density. These ELMs are detrimental to prolonged operation, as the divertor plates are unable to withstand such transient heatloads for the timescales required for long-term power reactor operation (divertor plates incapable of being utilized for many years would render commercial fusion plants uneconomical). Type-II ELMs, or "grassy" ELMs, are ELMs that occur at much higher frequencies than Type-I ELMs but produce far lower transport into the so-called scrape-off layer[2]. Grassy ELMs are thus not as detrimental to quasi-steady-state reactor operation and can be beneficial due to their ability to provide a small level of transport out of the plasma if controlled properly [7]. Type-III ELMs are similar to type-II ELMs in terms of their frequency and produce a modest amount of transport out of the plasma. In contrast to Type-I ELMs, however, their frequency decreases with increasing heating power.

In the late 1990s, DIII-D discovered a new operating regime that is free of ELMs: QH-mode or Quiescent H-mode [8]. This regime was initially accessed with NBI injection counter to the direction of the plasma current as well as cryopumping to reduce the plasma

[2]The scrape-off layer, or SOL, is the next-furthest layer out of the plasma radially from the core and edge. Particles that find themselves in the SOL are often swept into the divertor region. The border between the confined plasma and the SOL is called the "separatrix".

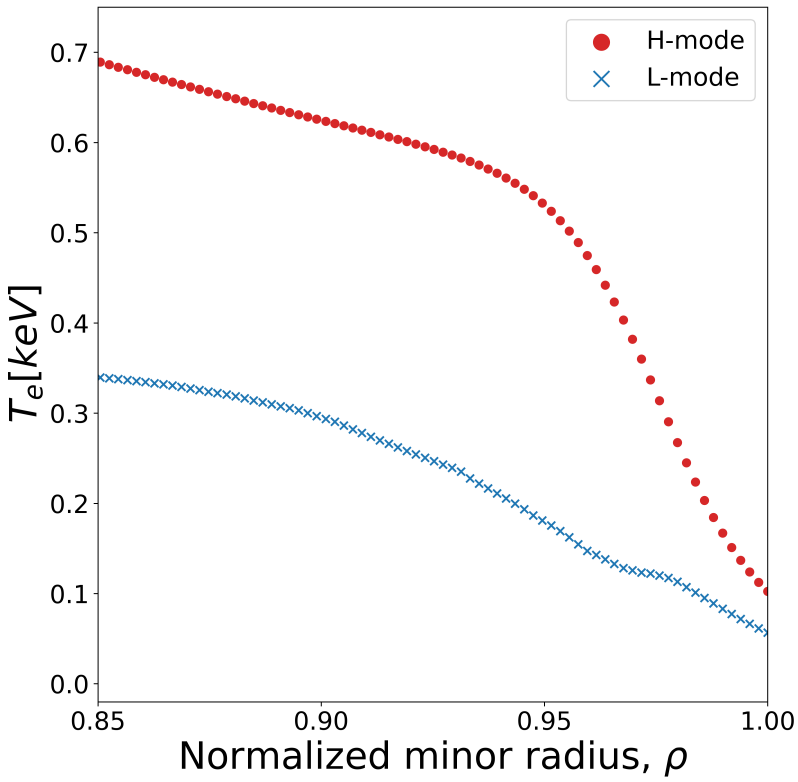

Figure 1.3: Electron temperature for shot 144977 in H-mode and L-mode at an instance of time (data collected temporally around an instance in time is referred to as data for a "timeslice"). Note the characteristic "pedestal" structure seen in the electron temperature in the last few centimeters of the plasma for the H-mode timeslice.

density. The term ‘quiescent’ describes the lack of ELMs in QH-mode plasmas: in initial testing, ELMs would be produced as the plasma was heated up using NBI; however, they would suddenly disappear, leaving only an edge harmonic oscillation (EHO) initially only picked up by magnetic pickup probes but with the plasma otherwise continuing to demonstrate H-mode-like performance. Additional experiments helped further characterize QH-mode. The work in [9] helped characterize the operational boundaries of QH-mode at DIII-D. It was also found that the edge density and temperature profiles seemed to saturate (i.e., they did not increase in magnitude or in terms of the gradient characterizing the pedestal) with increasing NBI power. It was also noted that the duration of the NBI was the limiting factor for the duration of QH-mode and that there did not appear to be a physics constraint on how long a discharge could remain in steady state.

Subsequent work (see, e.g., [10] [11]) on QH-mode at DIII-D demonstrated that this regime could be accessed and maintained at high densities, high enough to approach the Greenwald density fractions to be seen at the International Thermonuclear Experimental Reactor (ITER). Strong plasma shaping allowed access to these higher densities and allowed ITER-relevant parameters to be obtained. That work also helped validate the EPED model, which is a reduced physics model that predicts the pressure at the top of the pedestal (see, e.g., [12] [13] [14]).

The EPED model also predicted a new regime accessible through QH-mode: Super-H mode, or SH-mode. SH-mode is an improved operating regime accessed via the QH-mode

edge pathway and is characterized by substantially higher, ITER-relevant pedestal height and density [15]. A high pedestal pressure of $80kPa$ was obtained at Alcator C-Mod in SH-mode [16]. SH-mode is also characterized by ELMs, although it has been found that steady-state operation exhibits ELMs carrying only a modest amount of energy out of the plasma [17]. Recent work in [18] has demonstrated that SH-mode is also compatible with radiative divertors, which are beneficial in that they spread the heat loads on the divertor plates to larger surface areas, reducing the material and component stresses on the divertors.

Although much progress has been made, tokamaks still face several fundamental challenges. These include

- Materials-related challenges
- Disruption avoidance, detection, and mitigation
- Transport & rotation understanding
- Instabilities and their control

The subject of this thesis research falls into the third category. Transport in plasmas can be understood from 3 aspects: short-range forces, long-range forces, and anomalous transport. Short-range forces give rise to diffusive/conductive transport, which is the result of particle collisions and other short-range forces that produce radial particle and heat fluxes that are proportional to density and temperature gradients, respectively. Long-range forces are those produced by electromagnetic and $\vec{v} \times \vec{B}$ forces. Anomalous transport generally refers to non-classical transport caused by density and temperature fluctuations (turbulence) and other poorly understood phenomena. Current research generally does not consider

multiple factors that find importance in the edge plasma: ion orbit loss, non-conductive heat transfer other than convective heat transfer, and the pinch velocity. This research will show how these non-diffusive and non-conductive aspects can be corrected for and how they change the interpreted conductivity and diffusion coefficients. In the literature, theoretical calculations of $\chi_{r,j}$ are made and compared to $\chi_{r,j}$ inferred from experiment; however, the effects of IOL and other non-conductive transport mechanisms are not generally corrected for in these inferred $\chi_{r,j}$. In other words, theoretical calculations of $\chi_{r,j}$ are being compared against inferred $\chi_{r,j}$ that have not been corrected for non-conductive transport mechanisms. This research attempts to show why these corrections to the experimentally inferred $\chi_{r,j}$ are important to make.

1.4 Summary

Over the last six decades, many hard-fought scientific accomplishments in fusion science have been realized, and, as a result, the tokamak, with its shaped plasma, is generally seen as the most likely design to result in a functional power reactor. In this section, a brief overview of the underlying fusion reaction sought for use in nuclear fusion reactors was provided. Tokamaks, the main candidate and most heavily researched reactor variant, were discussed, and the challenges involved in perfecting them were enumerated. The various operating regimes that this thesis will look at were also briefly discussed. This research will focus on transport in the edge plasma, specifically on interpreting the conductive

heat and diffusive particle transport in the edge plasma, therein carefully accounting for non-conductive and non-diffusive transport mechanisms. The next chapter will present the specific objectives of this research.

CHAPTER 2

THESIS OBJECTIVES

2.1 Primary Objectives

The primary objectives of this doctoral thesis are as follows:

1. We will present an improved methodology for the interpretation, from experimental measurements and input conditions, of the particle diffusion coefficient, the thermal conductivity and the toroidal viscosity coefficient, therein taking into account that the experimental radial particle and energy fluxes are also determined by processes other than diffusion, conduction and viscosity, respectively.

2. We will apply this methodology to interpret transport coefficients for DIII-D shots in different confinement regimes.

3. We will present a comparison of the interpreted diffusion and thermal conduction coefficients to different theoretical models to demonstrate the significant differences in the comparisons and show that such comparisons must correct the inferred transport coefficients for phenomena such as IOL and other non-conductive and non-diffusive phenomena.

The main problem that we will attempt to address is the following. Experimentally

determined total radial energy and particle fluxes are due to many mechanisms other than short-range energy conduction and particle diffusion mechanisms (i.e., long-range forces, such as IOL, long-range electromagnetic forces, work done by the flowing plasma on the stress tensor, the outward flow of rotational energy, etc.). These other non-diffusive/non-conductive contributions must be determined theoretically and subtracted from the experimentally determined total radial particle and energy fluxes in order to obtain the radial conductive energy flux and diffusive particle flux, which can be used to evaluate the heat conductivity and particle diffusion coefficients for comparison with theory.

In chapter 5, we will use the particle and momentum balance equations to show that we can use experimentally obtained values to calculate a composite momentum loss frequency due to viscosity, inertia, charge exchange, and ionization, written $\nu_{d,j} \equiv \nu_j^{visc} + \nu_j^{iner} + \nu_j^{cx} + \nu_j^{ion}$, for the main plasma ions j (the impurities are indicated with the subscript k), which will allow us to write the total radial particle flux as the sum of a diffusive component and a non-diffusive component proportional to the "pinch velocity":

$$\Gamma_{r,j} \equiv < n_j v_{r,j} > = n_j D_{jj} \left(L_{n,j}^{-1} + L_{T,j}^{-1} \right) - n_j D_{jk} \left(L_{n,k}^{-1} + L_{T,k}^{-1} \right) + n_j v_{p,j} \qquad (2.1)$$

in which n_j is the ion density; $v_{r,j}$ is the radial ion velocity; D_{jj} and D_{jk} are the ion diffusion coefficients; $L_{n,j}^{-1} = -\frac{\partial n_j}{\partial r}/n_j)$ and $L_{T,j}^{-1} = (-\frac{\partial T_j}{\partial r}/T_j)$ are the inverse ion density and temperature scale lengths, respectively; $L_{n,k}^{-1} = (-\frac{\partial n_k}{\partial r}/n_k)$ and $L_{T,k}^{-1} = (-\frac{\partial T_k}{\partial r}/T_k)$ are the inverse impurity density and temperature scale lengths, respectively; and the pinch

velocity is given by

$$n_j v_{p,j} \equiv -\frac{M_{\phi,j}}{e_j B_\theta} - \frac{n_j E_\phi^A}{B_\theta} + \frac{n_j m_j \nu_{d,j}^*}{e_j B_\theta}\left(\frac{E_r}{B_\theta}\right) + \frac{n_j m_j f_p^{-1}}{e_j B_\theta}((\nu_{jk} + \nu_{d,j}^*)v_{\theta,j} - \nu_{jk} v_{\theta,k}) \quad (2.2)$$

where $M_{\phi,j}$ is the external toroidal momentum input (e.g., from neutral beam injection), B_θ is the poloidal magnetic field, E_ϕ^A is the toroidal electrostatic potential, m_j is the ion mass, $\nu_{d,j}^*$ is the above-mentioned composite momentum loss frequency, e_j is the ion charge, E_r is the radial electric field, $f_p = B_\theta / B_{\text{total}}$, ν_{jk} is the ion-impurity collision frequency, $v_{\theta,j}$ is the ion poloidal velocity, and $v_{\theta,k}$ is the impurity poloidal velocity. It can be shown that the total energy flow out of the plasma can be written

$$\vec{Q}_j = \frac{1}{2} n_j m_j (\vec{v}_j \cdot \vec{v}_j)\vec{v}_j + \frac{5}{2} p_j \vec{v}_j + \vec{v}_j \cdot \pi_j + \vec{q}_j \quad (2.3)$$

where $\vec{Q}_j$ is the total heat flux, $\frac{1}{2} n_j m_j (\vec{v}_j \cdot \vec{v}_j)\vec{v}_j$ is the flow of inertial energy, $\frac{5}{2} p_j \vec{v}_j = \frac{3}{2} n_j T_j v_{j,r} + n_j T_j v_{j,r}$ is the convective heat flux plus the work done by the flowing plasma against the pressure tensor, $\vec{v}_j \cdot \pi_j$ is the viscous heat flux, and $\vec{q}_j$ is the conductive heat flux. As we will show in section 5.2, we will subtract off the non-conductive radial heat flux components (i.e., the convective, inertial, pressure tensor work and viscous heat fluxes) from the radial component of the total heat flux to determine the experimentally interpreted radial conductive heat flux $q_{r,j}$.

Given the above, the interpretation of the experimental χ_r and D_r will be performed as follows. First, we use the experimental data from DIII-D to infer the total radial particle

flux (Γ_r^{tot}) and the total radial heat flux (Q_r^{tot}) to identify the radial particle and heat flux components that are not diffusive or conductive, respectively, in nature, i.e.,

$$\Gamma_{j,r}^{\text{diff}} = \Gamma_{j,r}^{\text{tot}} - \Gamma_{j,r}^{\text{non-diff}} \tag{2.4}$$

$$q_{j,r}^{\text{cond}} = Q_{j,r}^{\text{tot}} - Q_{j,r}^{\text{non-cond}} \tag{2.5}$$

where $q_{r,j}^{\text{cond}}$ is the radial conductive heat flux, through the use of particle, momentum, and energy balance equations. This involves correcting for the above non-diffusive and non-conductive transport mechanisms (IOL, convective heat flux, etc.). Once we know these non-diffusive and non-conductive components and given that the experimental diffusive particle flux and conductive heat flux are given by

$$\Gamma^{\text{diff,exp}} = -D\nabla n^{\text{exp}} \tag{2.6}$$

$$q^{\text{cond, exp}} = -\chi n^{\text{exp}} \nabla T^{\text{exp}} \tag{2.7}$$

with n^{exp} and T^{exp} being the experimental ion/electron densities and ion/electron temperatures, respectively, we can correctly calculate experimental particle diffusion and heat conductivity coefficients

$$D^{\text{exp}} = -\frac{\Gamma_j^{\text{tot}} - \Gamma_j^{\text{non-diff}}}{\nabla \mathbf{n}^{\text{exp}}} \tag{2.8}$$

$$\chi^{\text{exp}} = \frac{q^{\text{cond}}}{n^{\text{exp}} \nabla T^{\text{exp}}} = -\frac{Q_j^{\text{tot}} - Q_j^{\text{non-cond}}}{n^{\text{exp}} \nabla T^{\text{exp}}} \tag{2.9}$$

To obtain the radial components of Γ^{tot}, $\Gamma^{\text{non-diff}}$, Q^{tot}, and $Q^{\text{non-cond}}$, we take moments of the particle, momentum, and energy balance equations on the plasma for the ions and electrons, as shown in the next section.

We are performing this analysis in this manner to obtain more accurate evaluations of diffusive and conductive transport in plasmas, as well as determine the magnitude of the non-diffusive and non-conductive effects. With these values of χ and D, we will compare the various theoretical models to said values in an effort to identify the underlying transport mechanisms in various regimes (L-mode, H-mode, RMP, etc.). This would not be consistent using χ and D values obtained using radial particle and heat fluxes that are not corrected for non-diffusive and non-conductive mechanisms, as is presently done in many interpretations. This work essentially extends the work in [19] to a variety of operating regimes and compares with theoretical formulations for heat transport coefficients. In [19], it was shown that it is necessary to correct the total experimental radial heat flux to subtract out the effects of other non-conductive mechanisms such as thermal convection, the convection of rotational energy and ion orbit loss in order to reduce the total experimentally determined heat flux to the heat flux attributable to thermal conduction, which can be used to infer the thermal conductivity.

To address the first objective of this thesis, the GTEDGE2 code[1] has been updated to improve the interpretations of the experimental radial particle diffusion (D_r) and heat

[1]The GTEDGE2 code can be found at https://github.com/gt-frc/gt3

conductivity (χ_r) coefficients by correcting for non-diffusive and non-conductive phenomena. In contrast to GTEDGE, GTEDGE2 directly solves the particle, momentum, and energy balance equations in a 1-D slab geometry (in contrast to the power balance methodology of GTEDGE) for the full plasma ($0 < \rho < 1.0$). GTEDGE2 applies an Ion Orbit Loss (IOL) calculation to each species of ion injected via neutral beam injector (NBI) as well. Coupling to a neutrals recycling code is achieved with integration of GTNEUTPY, a parallelized Python port of the GTNEUT code based on the transmission-escape probability method[20]. This allows us to obtain particle and heat sources for calculating the particle and heat fluxes. Note that the GTEDGE2 code can run on a standard laptop computer in less than a minute if neutral recycling is not calculated (or has been previously calculated). GTNEUTPY can be run on the order of minutes if ionization rates and neutral densities are to be calculated.

To reiterate our task, when a given particle or heat flux is caused by a combination of several transport and non-transport mechanisms, say, A, B, and C, and one wishes to determine a transport coefficient for mechanism C, one must determine the contributions to the total flux due to mechanisms A and B and subtract them from the total transport flux in order to determine the transport flux due solely to mechanism C. To this end, we use the GTEDGE2 code to correct for IOL, which is a non-diffusive transport mechanism that affects the total radial particle flux and neutral beam heating; the convective radial heat flux; work done by the plasma on the confining pressure tensor; viscous heating; and the transport of rotational energy. These corrections for non-conductive mechanisms on the

experimentally inferred total radial heat flux allow us to obtain correct experimental radial heat conductivity coefficients.

Figure 2.1 provides an example of this; note that this type of graph will be used throughout this thesis. This graph shows the inferred heat fluxes for a moment in time for shot 163477, an upper single-null QH-mode shot. The top plot, given as ●, is the inferred total radial ion heat flux solved from energy balance without our IOL correction. It is common, although not always the case, to assume that this heat flux is equal to $q_{r,j}^{cond}$, i.e., all energy flowing out of the plasma from thermalized ions is conductive in nature and thus satisfies Fourier's law. This thesis demonstrates that this is not the case, i.e., a substantial amount of heat is transporting out in a non-conductive manner. The next plot, marked with $\times$, is the inferred total radial ion heat flux from energy balance but with the IOL correction for both thermal ions and for ions from NBI heating. We see that the IOL correction significantly reduces the total radial ion heat flux in the edge. We also want to present the other heat fluxes that we infer in this research for comparison. Ultimately, these other heat fluxes, which are non-conductive in nature, will be subtracted from the IOL-corrected total radial ion heat flux to determine the conductive heat flux: $q_{r,j}^{\text{cond}}$. The next plot, marked with +, is the inferred radial ion convective heat flux. The next plot, marked with ◆, is the heat flux resulting from the work done by the plasma on the pressure tensor. The next plot, marked with ▼, is the heat flux from the work done by the flowing plasma on the pressure tensor. The final plot, marked with ▲, is the heat flux from viscous heating. We see here

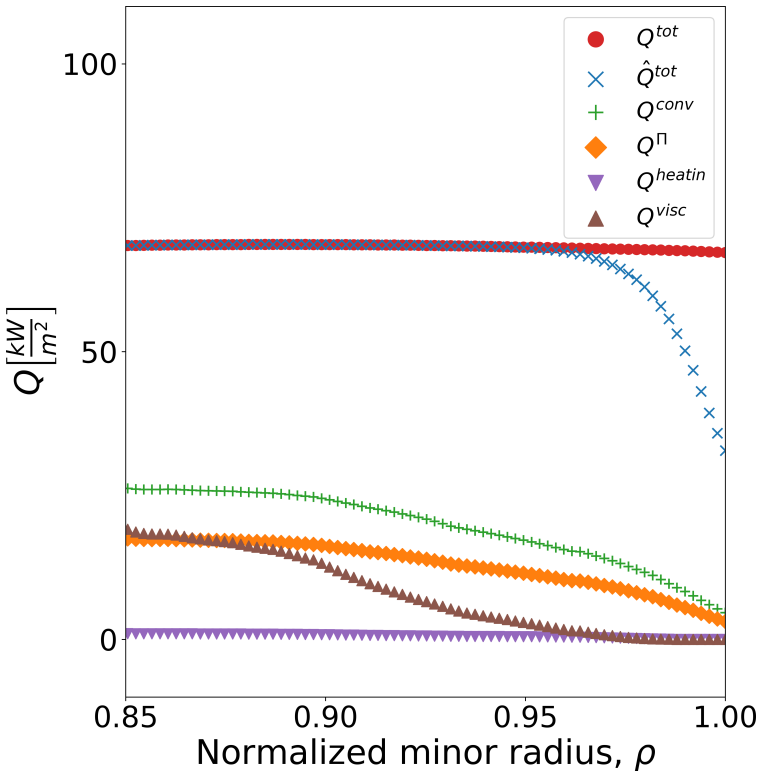

Figure 2.1: Inferred heat fluxes for shot 163477, an upper single-null QH-mode shot.

that the non-conductive heat fluxes are significant and should be subtracted from $\hat{Q}^{tot}$ so that the actual conductive heat flux, i.e., $q^{cond} = \hat{Q}^{tot} - Q^{conv} - Q^{\Pi} - Q^{heatin} - Q^{visc}$, can be used to infer $\chi_{r,j}$. Note that we will also find that in certain shots, these non-conductive heat fluxes are not significant.

We also calculate a composite momentum loss frequency (ν_d). To this end, we utilize the Stacey-Sigmar extension of the Braginskii gyroviscosity to toroidal field line geometry. This extension allows us to calculate a composite momentum loss frequency $\nu_{d,j} \equiv \nu_j^{visc} + \nu_j^{iner} + \nu_j^{cx} + \nu_j^{ion}$ due to viscosity, inertia, charge exchange, and ionization. This allows us to calculate a corrected experimental diffusive radial particle flux and thus a particle diffusion coefficient, also corrected for IOL. We are able to show that correcting for these non-

diffusive and non-conductive phenomena produces a significant difference in the inferred experimental diffusion and conductivity coefficients.

To address the second objective of this thesis, we will analyze various DIII-D shots using the GTEDGE2 code. These shots represent various operating regimes (L-mode, H-mode, RMP, reverse triangularity, QH-Mode, and SH-mode), and we will demonstrate the substantial effects of these non-diffusive and non-conductive phenomena on the inferred particle diffusion and heat conduction coefficients.

To address the third objective of this thesis, these inferred coefficients from the above operating regimes will be compared with theoretical models in order to demonstrate the substantial differences that may exist in the inferred transport coefficients when comparing to theoretical models. The theoretical models that will be analyzed include neoclassical, ion temperature gradient (ITG), and others.

2.2 Summary

This section reviewed the primary objectives of this research. The primary objectives of this research are to 1) obtain an improved interpretation of radial particle diffusion and heat conductivity coefficients in the edge plasma, therein correcting for non-diffusive and non-conductive mechanisms, which requires the development of a methodology for the interpretation of experimental viscosity coefficients from experimental data; 2) perform a comparison of various DIII-D shots in various regimes to study the effects of correcting

for the above non-conductive and non-diffusive mechanisms; and 3) use these improved energy conductivity coefficients in comparisons with theoretical models of conductive heat transport in tokamaks. It was noted that this research uses a composite momentum loss frequency to account for all sources of momentum loss of the plasma ions, allowing us to write the total particle flux as the sum of a diffusive component and a non-diffusive component, i.e., a component proportional to the pinch velocity. It was also shown that the total heat flux can be written as the sum of conductive and non-conductive terms, and an overview was provided on how the experimental data will be interpreted such that an experimental heat conductivity coefficient could be calculated. In the next section, a literature review of select research applicable to the work done here will be provided.

CHAPTER 3

LITERATURE REVIEW

3.1 Experimental Interpretation of Plasma Transport

Substantial work has been done to attempt to explain transport in tokamak plasmas. Importantly, research has focused on attempting to explain transport in the edge pedestal region of H-mode and other plasmas[21]. It has become clear that the edge pedestal region of H-mode plasmas dictates the boundary conditions of overall plasma performance; therefore, it is important to understand the heat and particle transport in the edge plasma [5] [22] [23] [24]. The work in [25] investigated the use of various transport interpretation codes to infer ion and electron heat conduction coefficients and particle diffusion coefficients. That work looked at multiple interpretive codes and found that interpretive codes such as the one the current research is based on are appropriate for interpreting heat conduction coefficients and particle diffusion coefficients in most of the edge plasma. The work also demonstrated that the recycling thermal neutral density in the "X-point" region and the ionization are two of the greatest uncertainties in this type of research.

[26] inferred diffusive heat conduction coefficients for various splits of the electron and ion heat fluxes, which are experimentally uncertain values. [27] derived a generalized pinch-diffusion relation based on momentum conservation for ion transport during ELM-

free, steady-state operation. [28] interpretted radial ion and electron heat conduction on data from two DIII-D, matched resonant magnetic perturbation (RMP) shots before and after ELMs occurred. That work hypothesized that the increased radial electron transport seen when these magnetic perturbations were applied was not the cause of the ELM suppression and that another transport mechanism must underly the ELM suppression seen; increased χ_e was found in both RMP and no-RMP cases during the build up to the ELM crash. In addition, that work was unable to find a good match between theoretical calculations of χ_i and the experimentally inferred values. The ITG predictions were closest to the experimentally inferred values, although a good match was not obtained for the entire edge plasma. The paleoclassical model of electron transport was found to be in good agreement at certain times. [29] investigated transport in an L-mode and two H-mode shots from DIII-D. For the L-mode shot, ETG and paleoclassical predictions achieved good agreement with the inferred χ_e. However, again, experimentally inferred values of χ_i did not match theoretical predictions except for a matching with thermal instability theory at the very far edge. For the H-mode shots, clear agreement was not obtained for any theory, although ITG transport achieved the best agreement out of the theoretical calculations.

Various efforts have been devoted to interpretting heat and particle transport as it relates to plasma rotation, the radial electric field, and ion orbit loss, the latter being a form of non-diffusive transport [30] [31] [32] [33] [34] [35] [36]. A recent overview of such work can be found in [37] and [38]. [39] and [40] showed that ion orbit loss (including X-

transport) and the particle "pinch" constitute two non-diffusive mechanisms for transport that are important in the edge plasma. That work looked at multiple DIII-D discharges to demonstrate the importance of these transport mechanisms. [41] developed a formalism for correcting the total ion radial heat flux for viscous heating based on Braginskii's formalism. The formalism utilized a Fourier expansion in θ of the poloidal and toroidal rotation velocities. Note that such asymmetries in the rotation velocities are difficult to measure experimentally but can be modeled (see, e.g., [42]). That formalism was applied to a DIII-D H-mode discharge. Calculations for up-down rotation velocity asymmetries of 1% - 10% were performed, and it was shown that such rotation velocity asymmetries can have a substantial effect on the inferred ion heat conductivity.

[31] utilized main ion toroidal velocity measurements to demonstrate a peaking of so-called "intrinsic rotation" ascribable to ion orbit loss near the separatrix, which confirmed predicted co-current rotation caused by ion orbit loss. The inclusion of ion orbit loss, which is a kinetic effect, into fluid theory to obtain the above result was demonstrated in [43]. These results were further supported by XGC0, a particle-in-cell drift-kinetic solver, simulations applied to a DIII-D shot in [44] as well as by XGC1 in [45]. Application of ion orbit loss into a fluid model for the edge plasma profile in [46] was used to provide a constraint for an equilibrium edge pressure profile found in H-mode plasmas. The above concepts have been applied to non-DIII-D plasmas as well. A geometric approach was used and applied to shots at ASDEX-Upgrade to model the ion orbit loss at the L-to-H transition

[47].

Heat and particle transport have been investigated in ASDEX-Upgrade. [48] investigated ion heat transport between ELMs. In that work, electron-cyclotron resonant heating deposition locations were varied to observe the effects on the ion heat transport. Their transport analysis using the ASTRA 1.5D transport code found that, when compared with calculations from the NEOART, NEO, and NCLASS codes, neoclassical predictions were close to inferred $\chi_{i,r}$ in the edge plasma and in good agreement in the edge transport barrier region. Their results also demonstrated the validity of the general assumption that conductive ion heat transport in the edge plasma is a local phenomenon, i.e., it is not affected by the core. Later, [49] looked at heat conductivity in the edge across an ELM cycle. They found that their experimentally inferred heat conductivity matched neoclassical predictions within their uncertainties in the edge plasma. However, transport appeared to be substantially higher than neoclassical theory would predict immediately following the ELM in the steep-gradient region of the pedestal.

3.2 Ion Radial Heat and Particle Transport

An early review and work on neoclassical transport in axisymmetric, toroidal reactors were conducted in [50] using a variational principle with the Fokker-Planck collision operator in the banana regime. This work took an approximation at lowest order in the inverse aspect ratio to derive ion and electron heat and particle fluxes. [51] extended the neoclassical

theory to collisional plasmas. Using a large aspect ratio approximation, the radial ion particle flux and radial ion and electron heat fluxes were given as

$$\Gamma_r = -\frac{n\rho_e^2}{\tau_e}\frac{8\pi^2}{l^2}\left[0.33p_e^{-1}\left(\frac{dp_e}{dr}+\frac{dp_i}{dr}\right)-\frac{0.27}{T_e}\frac{dT_e}{dr}\right] \tag{3.1}$$

$$q_{r,j} = -0.8\frac{n_j\rho_j^2}{\tau_j}\left(\frac{8\pi^2}{l^2}\right)\frac{dT_j}{dr} \tag{3.2}$$

$$q_{r,e} = -\frac{n_eT_e\rho_e^2}{\tau_e}\left(\frac{8\pi^2}{l^2}\right)\left[\frac{0.98}{T_e}\frac{dT_e}{dr}-\frac{0.27}{P_e}\left(\frac{dp_e}{dr}+\frac{dp_i}{dr}\right)\right] \tag{3.3}$$

where $\rho_e^2 \equiv 2m_ec^2T_e/e^2B_0^2$ and $\rho_j^2 \equiv 2m_jc^2T_j/e^2B_0^2$. This work was later modified in [52] by considering a finite aspect ratio and extended to include impurity species in [53] to obtain the Chang-Hinton neoclassical ion conductivity

$$\chi_i^{neo} = \epsilon^{\frac{1}{2}}\rho_{i,\theta}^2\nu_{i,i}[a_1g_1 + a_2(g_1-g_2)] \tag{3.4}$$

where impurities, collisional and finite inverse aspect ratio effects are accounted for by the as, and the effect of the Shavranov shift is accounted for by the gs. These coefficients are given by

$$
\begin{aligned}
a_1 &= \frac{0.66(1+1.54\alpha)+(1.88\sqrt{\epsilon}-1.54\epsilon)(1+3.75\alpha)}{1+1.03\sqrt{\mu_i^*}+0.31\mu_i^*} \\
a_2 &= \frac{0.59\mu_i^*\epsilon}{1+0.74\mu_i^*\epsilon^{\frac{2}{2}}}[1+\frac{1.33\alpha(1+0.60\alpha)}{1+1.79\alpha}] \\
g_1 &= \frac{1+\frac{3}{2}(\epsilon^2+\epsilon\Delta')+\frac{3}{8}\epsilon^3\Delta'}{1+\frac{1}{2}\epsilon\Delta'} \\
g_2 &= \frac{\sqrt{1-\epsilon^2}(1+\frac{\epsilon\Delta'}{2})}{1+\frac{\Delta'}{\epsilon}(\sqrt{1-\epsilon^2}-1)}
\end{aligned}
\tag{3.5}
$$

We will use Equation 3.4 in this thesis for one of our comparisons with our inferred $\chi_{r,j}$.

Experimental results have shown that heat and particle transport cannot be fully explained by neoclassical effects in the core (see [54][55]), although there are indications that neoclassical transport might not fully explain ion transport in DIII-D[56].

3.3 Turbulent Ion Transport

Transport above the neoclassical level is termed *anomalous* transport and is generally considered to be a result of turbulent fluctuations in magnetic fields, electric fields, and particle densities. Most of the effort in the study of such transport begins by considering electrostatic drift waves and the resulting $\vec{E}\times\vec{B}$ drifts. These drift waves are essentially ion acoustic waves in nonhomogenous plasmas, with ion pressure gradients and electrostatic potentials acting as the restoring forces.

Ion temperature gradient (ITG) modes represent a drift wave instability that is believed to be likely responsible for anomalous ion thermal transport. The toroidal ITG modes become unstable for $R/L_{T_j} > (R/L_{T_j})_{\text{crit}}$ and produce thermal ion transport. Early work

showed that, in the presence of large (but not excessive) magnetic shear, ion temperature gradients create unstable modes that lead to transport that is not damped out by Landau dampening [57]. Later computational work found the dominant nonlinear saturation mechanism to be nonlinear $\vec{E} \times \vec{B}$ convection of the ion pressure [58]. The authors also provided an approximation of χ_j^{ITG}. In more recent work, the GKS code was applied to DIII-D shots to study ITG and TEM modes [59]. That work found that, in L-mode plasmas, the GKS code predicted ITG modes in agreement with experimentally inferred ion heat diffusivity in the sense that increased transport was inferred when the critical gradient was surpassed. Additional work on ITG in DIII-D plasmas was done in [60]. In that work, evidence of a critical gradient in L- and H-mode plasmas at DIII-D was provided. It was shown that, in much of the plasma, the ion heat diffusivity rapidly increased at approximately the location corresponding to the critical gradient calculated by the IFS-PPPL model. The authors also scanned various parameters to find the most important parameters in determining this critical gradient in DIII-D discharges. It is important to note that much of this work is focused on the core plasma and is performed using highly complex, computationally expensive simulations such as in gyrokinetic codes. In contrast, the GTEDGE2 code, which focuses on the edge plasma ($0.85 < \rho < 1.0$) utilized in this thesis can be run on a standard consumer laptop on time scales of minutes.

Two other types of instabilities giving rise to ion transport are the drift Alfven modes and thermal instabilities. Drift Alfven instabilities are important in collsional edge plasma.

[61] showed that $\vec{E} \times \vec{B}$ sheer alone cannot stabilize these modes. An analytical model was developed in [62]:

$$\chi_i^{da} = \chi_i^{gb} \chi_\perp / \sqrt{\mu} \tag{3.6}$$

where the gyro-Bohm heat conductivity is $\chi_i^{gb} = \rho_s^2 c_s / L_{p_i}$, $\mu \approx -\frac{L_{p_i}}{qR}\sqrt{\frac{m_i T_e}{m_e T_i}}$ and

$$\chi_\perp = \left[\frac{(1+\beta_n^2)^{-3} + \nu_n^2}{1 + \beta_n^2 + \nu_n^{\frac{4}{3}}}\right]^{1/2} \tag{3.7}$$

in which $\beta_n \equiv \left(\frac{m_i}{m_e}\right)^{1/2} \beta \frac{qR}{L_{p_i}}$, $\beta = \frac{2\mu_0 n_e T_e}{B^2}$, $\nu_n \equiv \left(\frac{m_i}{m_e}\right)^{1/4} \frac{(qRL_{p_i})^{1/2}}{\lambda_e}$, and $\lambda_e - v_{\text{th,e}}/\nu_{e,i}$. We will compare this theoretical model to our inferred $\chi_{r,j}$ as part of the main results of this thesis.

3.4 Paleoclassical Electron Transport

For completeness, we touch briefly upon electron transport. Early work to explain electron transport provided the paleoclassical model of electron transport [63]. In the paleoclassical model, magnetic field diffusion on the scale of the electron collision time induced by Coulomb collisions causes radial transport of electrons. In the collisionless regime, which is more relevant to current and future reactors, the electron heat conduction coefficient can be approximated as

$$\chi_e^{paleo} \approx \frac{3}{2}\left(\frac{1}{\pi \bar{\delta}_e |q'|}\right)^{1/2} \frac{\eta_{||}^{nc}}{\mu_0} \tag{3.8}$$

where $\bar{\delta}_e$ is a normalized diffusive radial step, $q' = \frac{dq}{dr}$, and $\eta_{||}^{nc}/\eta_0$ is the neoclassical

parallel plasma resistivity. In the collisional regime,

$$\chi_e^{paleo} \approx \frac{3}{2}\frac{\eta_{||}^{nc}}{\eta_0}\frac{v_{T_e}}{\pi \bar{R} q}\frac{c^2}{w_p^2} \tag{3.9}$$

where $v_{T_e} = (2T_e/m_e)^{1/2}$ and $\bar{R} \approx R_0$.

The paleoclassical model was tested on numerous DIII-D shots in [64]. That work developed what the authors termed the paleoclassical-based pedestal model (PCBMP). In the model, paleoclassical transport was assumed to be the dominant transport mechanism in the edge pedestal, and values of χ_e^{paleo} were calculated. These values were then used to predict electron temperature and density gradients, which were compared to the experimentally measured gradients. The authors utilized the results to show that paleoclassical transport represented the minimum transport for electrons. The electron temperature gradients were not in agreement with those predicted by paleoclassical theory; additionally, the electron densities were sometimes greatly underpredicted (by as much as a factor of 2), implying another transport mechanism at play or further refinement of the theory being necessary.

3.5 Turbulent Electron Transport

The paleoclassical model does not sufficiently explain electron transport in tokamaks. One such transport mechanism is transport from electron temperature gradient (ETG) modes. A review of ETG modes and results on DIII-D shots can be found in [65]. Unlike other transport mechanisms, ETG modes are not believed to be greatly suppressed by $\vec{E} \times \vec{B}$

shear. In addition, ETG turbulence only produces electron heat transport. Early work in [66] used gyrokinetic simulations in the core to show that ETG turbulence could produce levels of anomalous transport seen experimentally and is associated with radially extended "streamers". However, [67] was unable to find evidence of a critical gradient in DIII-D discharges in two experiments probing the region $\rho < 0.6$. The experiments varied the electron heat flux and electron temperature inverse scale lengths at two radial locations using electron cyclotron heating. That work put upper limits on the relative scale length that were almost half of the plasma radius. On the other hand, [68] found evidence for ETG-driven transport in Tore Supra.

3.6 Summary

In this section, a literature review of relevant research on ion and electron transport in DIII-D and similar tokamaks was provided. Substantial work has been done to explain ion and electron transport in tokamak plasmas. Neoclassical transport has been found to be the minimum transport experienced in the plasma. On the other hand, it is clear that turbulence in the plasma can play an important role in transport, especially in the core, and various, sometimes conflicting results have been found. In the next chapter, we will begin the discussion of mechanisms that can be responsible for non-diffusive and non-conductive transport by presenting the physics behind ion orbit loss.

CHAPTER 4

ION ORBIT LOSS

4.1 Ion Orbit Loss

IOL is one mechanism whereby ions can be transported out of the plasma on loss orbits in a non-diffusive manner, i.e., these ions and their energy are transporting out of the plasma due to long-range, electromagnetic forces. Following [69], we use the conservation of canonical toroidal angular momentum

$$RmV_{\|}f_{\phi} + e\psi = R_0 mV_{\|0}f_{\phi 0} + e\psi_0 \tag{4.1}$$

to define an orbit on which an ion introduced at location "0" on flux surface ψ_0 with parallel velocity $V_{\|0}$ is constrained. Here, $f_{\phi} = \frac{B_{\phi}}{B^{\text{total}}}$, R is the major radius, and ψ is the flux surface. Conservation of energy and poloidal angular momentum give

$$\frac{1}{2}m(V_{\|}^2 + V_{\perp}^2) + e\phi = const = \frac{1}{2}m(V_{\|0}^2 + V_{\perp 0}^2) = e\phi_0 \equiv \frac{1}{2}mV_0^2 + e\phi_0 \tag{4.2}$$

$$\frac{mV_{\perp}^2}{2B} = const = \frac{mV_{\perp 0}^2}{2B_0} \tag{4.3}$$

We also require from the above conservation equations that

$$V_{\parallel} = \pm V_0 \left[1 - \left| \frac{B}{B_0} \right| (1 - \xi_0^2) + \frac{2e}{m V_0^2} (\phi - \phi_0) \right]^{1/2} \tag{4.4}$$

in which ϕ is the electrostatic potential and $\xi_0 = V_{\parallel 0}/V_0$ is the cosine of the initial guiding center velocity relative to the toroidal magnetic field direction. Plugging Equation 4.4 into Equation 4.2, squaring, and noting that $v_0 = \sqrt{v_{\parallel 0}^2 + v_{\perp 0}^2}$, leads to a quadratic equation in the initial ion velocity:

$$\begin{aligned} v_0^2 \left[\left(\left| \frac{B}{B_0} \right| \frac{f_{\varphi 0}}{f_\varphi} \xi_0 \right)^2 - 1 + (1 - \xi_0^2) \left| \frac{B}{B_0} \right| \right] + v_0 \left[\frac{2e(\psi_0 - \psi)}{R m f_\varphi} \left(\left| \frac{B}{B_0} \right| \frac{f_{\varphi 0}}{f_\varphi} \xi_0 \right) \right] + \\ \left[\left(\frac{e(\psi_0 - \psi)}{R m f_\varphi} \right)^2 - \frac{2e(\phi_0 - \phi)}{m} \right] = 0 \end{aligned} \tag{4.5}$$

Solving for v_0 dictates the velocity on a flux surface required for an ion to reach the LCFS[1] or "separatrix". A non-trivial number of particles in the edge plasma find themselves with sufficient energy (i.e., velocity) to reach the LCFS. We determine this portion of ions by sampling distributions of ions on flux surfaces and calculate how many ions are able to reach the LCFS. These ions, along with their energy and momentum, are presumed to be "ion orbit lost" to the plasma (actually, approximately 50% of ions that reach the LCFS will ultimately re-enter the plasma on banana orbits[70]).

Herein, the loss fractions for particles, energy, and momentum (i.e., what fraction of ions on that flux surface have sufficient energy to reach the LCFS) are given by $F(\rho)$, $E(\rho)$, and $M(\rho)$, and the corresponding differential loss fractions are given by $\frac{\partial F}{\partial \rho}$, $\frac{\partial E}{\partial \rho}$, and $\frac{\partial M}{\partial \rho}$,

[1]The Last Closed Flux Surface, or LCFS, is the last flux surface whereby poloidal field lines close upon themselves and do not intersect the vessel wall.

respectively.

4.2 IOL Effects

In the next chapter, we will discuss the plasma balance equations. For now, we note that IOL enters the toroidal momentum balance in Equation 5.2 as corrections to the $\vec{v} \times \mathbf{B}$ term and the external (NBI) momentum input $\mathbf{M}$, and it comes into the energy balance equation in Equation 5.18 as corrections to the NBI heat flux (q_{nbi}) and the convective heat flux (Q^{conv}). In the slab (1D) approximation, we have the following:

$$\frac{\partial \hat{\Gamma}_{r,i}}{dr} = -\frac{\partial n_i}{\partial t} + N_{nbi}(1 - 2f_{nbi}^{\text{iol}}) + n_e \nu_{ion} - 2\frac{\partial F^{\text{IOL}}}{\partial r}\hat{\Gamma}_{r,i} \tag{4.6}$$

$$\frac{\partial \hat{Q}_{r,i}}{dr} = -\frac{\partial}{\partial t}\left(\frac{3}{2} n_i T_i\right) + q_{nbi}^{i}(1 - \alpha e_{nbi}^{\text{IOL}}) - q_{ie} - n_i n_0^c < \sigma v >_{cx} \frac{3}{2}(T_i - T_0^c) - \frac{\partial E_i^{\text{IOL}}}{\partial r}\hat{Q}_{r,i} \tag{4.7}$$

where we are solving for the IOL-corrected total radial particle and energy fluxes (denoted $\hat{\Gamma}$ and $\hat{Q}$). Here, $2f_{nbi}^{iol}$ is the fraction of beam ions lost via IOL and is, in contrast to thermal-particle IOL, calculated assuming monoenergetic, monodirectional particles given that this is representative of neutral beam ions. The factor of 2 represents an inward-directed ion replacing an ion lost via ion orbit loss to maintain charge neutrality[2]. e_{nbi}^{iol}, the fraction of the radial heat flux from beam ions lost to IOL, is calculated similarly, and $\alpha = 1$ in a collisionless plasma.

[2]Recall that the radial particle flux is directional; therefore, an ion lost radially outward is replaced by an ion transporting inward, resulting in the factor of 2

4.3 IOL Sensitivity Scan

Here, we will attempt to show what parameters impact the IOL calculation and indicate what levers may be pulled to affect the IOL calculation. Ions will find themselves on loss orbits if their thermal velocity is greater than the velocity calculated in Equation 4.5[3]. We use a reference shot and separately vary the toroidal magnetic field B_ϕ, the radial electric field E_r, and the ion temperature T_i. Figure 4.1(a) shows the loss fractions for a reference shot with the toroidal magnetic field varied between 1.75 T and 2.5 T, the loss fractions when the radial electric field is varied by shifting the radial electric field in magnitude, and the loss fractions when we vary the ion temperature by uniformly scaling it. We see that varying the toroidal magnetic field does not substantially change the IOL profiles. In contrast, the radial electric field and ion temperature strongly affect the ion orbit loss. This is to be expected given the higher thermal velocity of particles at higher temperatures.

We want to provide the caveat that IOL theory is independent of collisionality and is based purely on conservation of energy and momentum. An ion that finds itself on a loss orbit is assumed to follow that orbit across the separatrix and into the scrape-off layer. However, a collision may put that ion onto a different orbit that is not a loss orbit. At lower collisionality, as what will be seen at ITER, this caveat concerning collisions will become less relevant as ions experience fewer collisions on average as they transport out of the

[3]Actually, since the particle velocities are assumed Maxwellian on a given flux surface, only a fraction of the particles on that flux surface will be on a loss orbit.

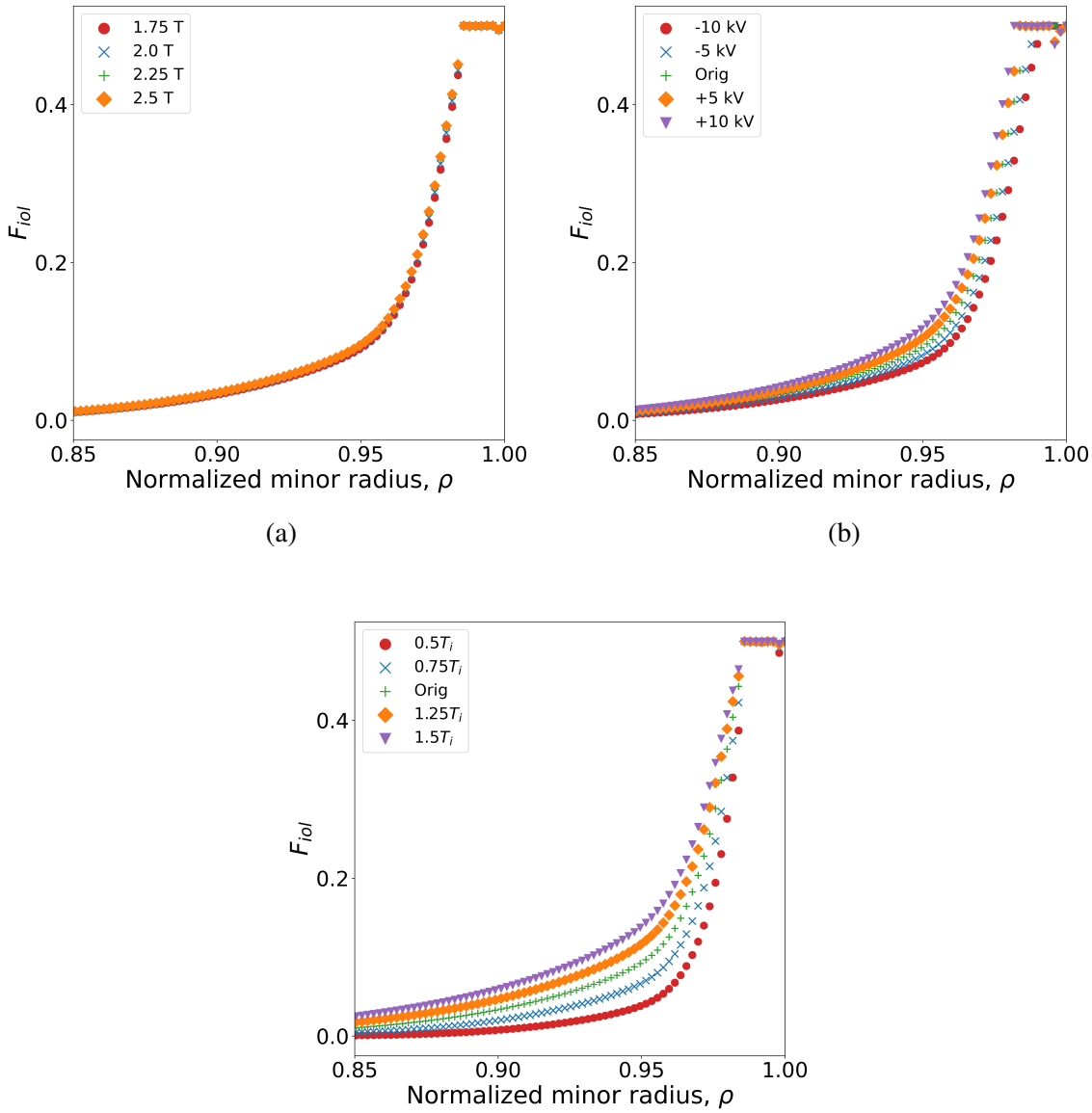

Figure 4.1: Reference IOL data with (a) $B_{\phi,0}$ varied, (b) E_r varied, and (c) T_i varied. Note that the toroidal magnetic field does not substantially affect the loss fractions, whereas the radial electric field and ion temperature do.

plasma.

4.4 IOL In Various Shot Regimes

In this section, we will observe the effects of IOL in the various regimes under study. First, we look at shot 144977 in L-mode and H-mode. The important plasma profiles for this shot are given in Figure 4.2. Note the characteristic pedestal structure in the ion density in H-mode and the dip in the electric field (or "E_r well") in H-mode. Figure 4.3 presents the particle, energy, and momentum loss fractions in L- vs. H-mode. Note that IOL more readily occurs toward the core in L-mode, e.g., at $\rho = 0.95$, approximately 2% of ions are on loss orbits in H-mode, whereas 6% are in L-mode. Given that the escape velocity, which determines the fraction of ions on a flux surface that are lost, is given by the solution to a complex quadratic equation involving, among other things, the radial electric field and ion temperature, it is not immediately clear what causes losses occurring closer to the core despite the higher ion pedestal temperature in the H-mode shot; however, given the sensitivity study in section 4.3, it is likely that this is driven by E_r. Figure 4.4 shows the heat and particle fluxes for shot 144977 in H-mode with and without the IOL corrections.

We want to note the important implications IOL has for our analysis. These loss fractions essentially act as particle and energy sinks in the balance equations discussed previously. This results in substantially reduced total radial ion heat and particle fluxes in the edge ($\approx 50\%$ from $\rho > 0.98$), as seen in Figure 4.4 using shot 144977 in H-mode

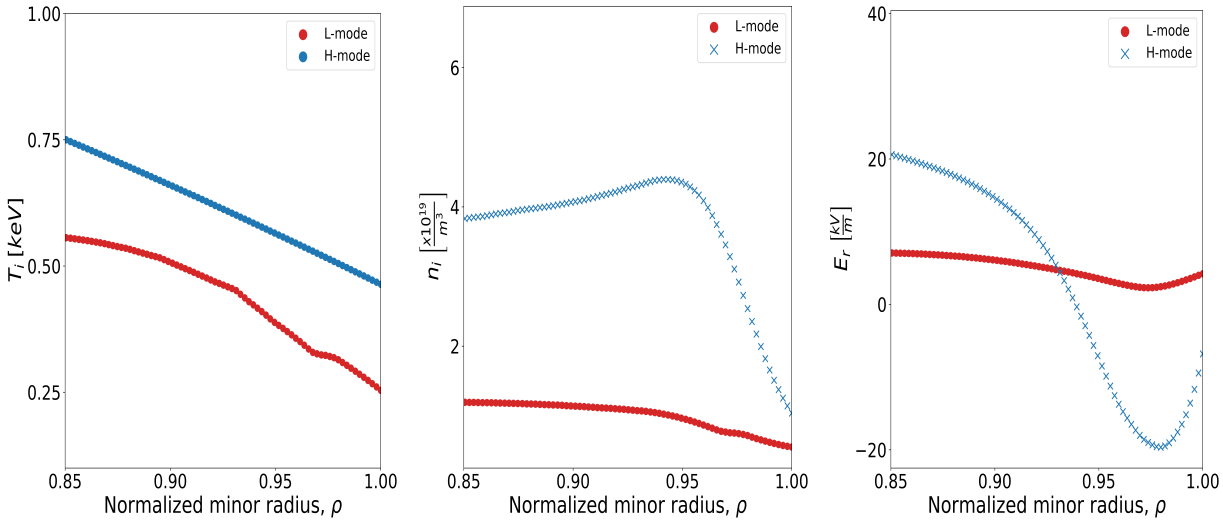

Figure 4.2: Plasma profiles for shot 144977 in L- and H-modes. (a) Plasma ion temperature. (b) Plasma ion density in the edge. Note that characteristic pedestal shape. (c) Radial electric field. Note the characteristic dip in the radial electric field in H-mode.

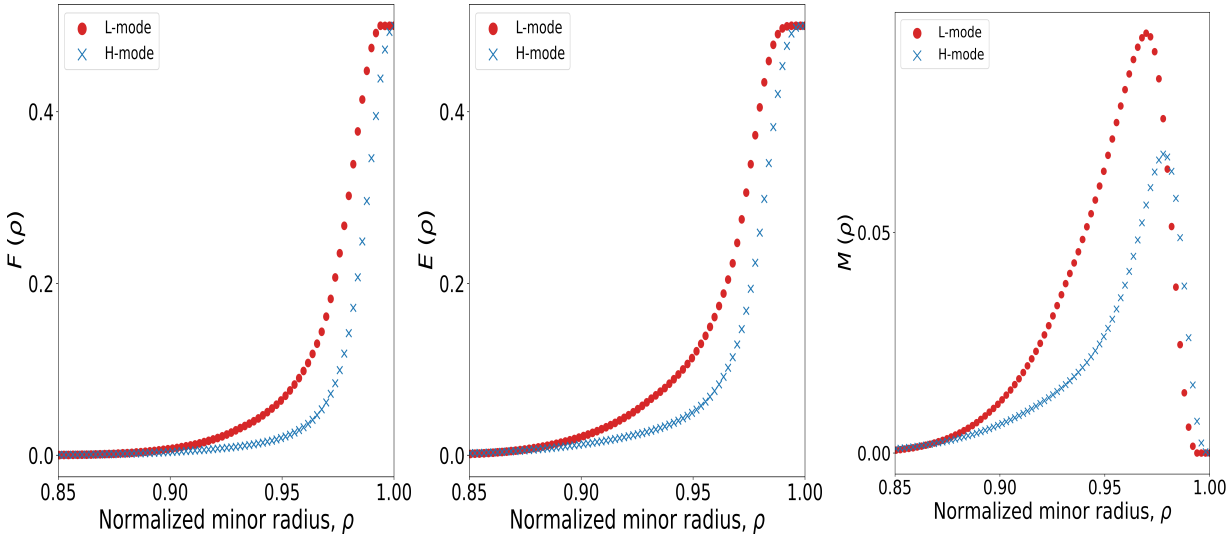

Figure 4.3: Ion Orbit Loss (IOL) profiles for shot 144977 in L- and H-modes. (a) Ion loss fraction. (b) Energy loss fraction. (c) Momentum loss fraction.

as an example. We ultimately are looking to explore the diffusive particle and conductive heat fluxes; thus, we must use these corrected total fluxes given that IOL is a non-diffusive phenomenon, i.e., it is a kinetic effect.

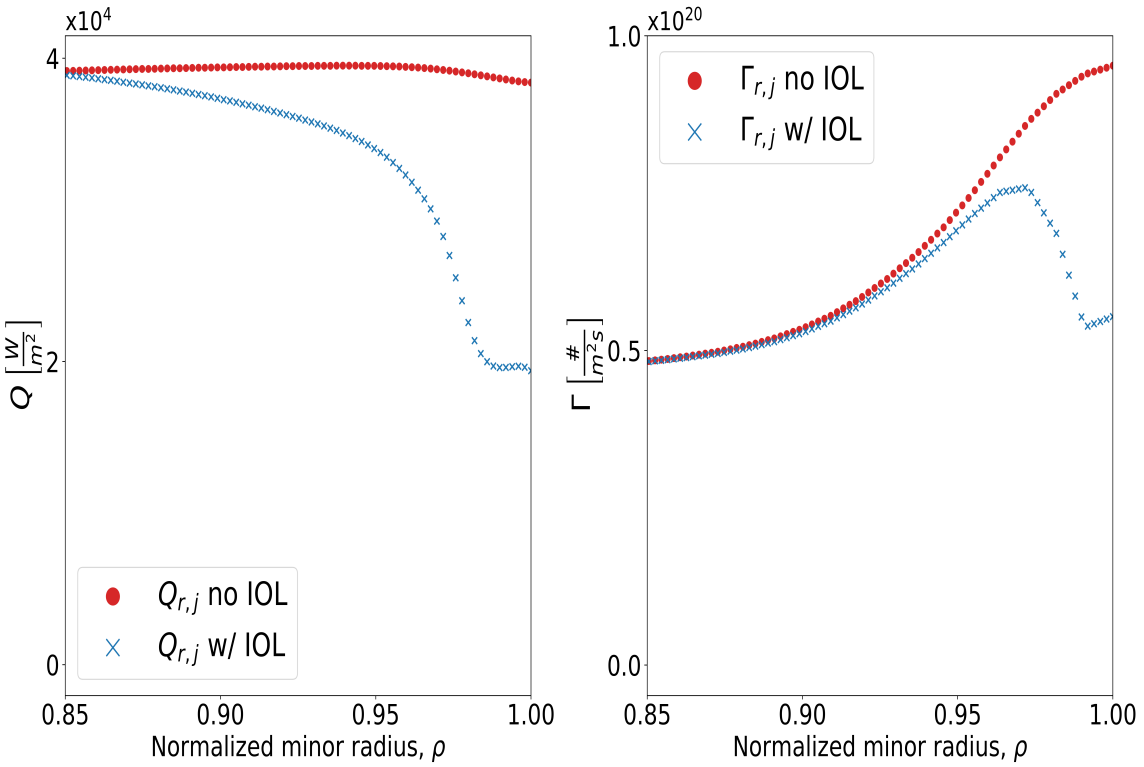

Figure 4.4: Inferred radial heat flux (Left) and total radial ion particle flux (Right) with and without the IOL corrections for shot 144977 in H-mode.

Next, we look at the effects of IOL on two so-called resonant magnetic perturbation (RMP) shots. DIII-D shots 123301 and 123302 are low-collisionality, matched RMP shots (see Refs. [71],[72],[73]). These perturbations in the magnetic field lines are achieved via so-called "I-coils" in order to increase the chaotic nature of magnetic field lines in the edge plasma, enhancing radial electron heat transport. These two shots were produced to be as identical as possible, except shot 123302 has these I-coils turned off. Previous work in [74] applied ion orbit loss to these matched RMP shots to demonstrate differential ion orbit losses between the two machine configurations. A comparison of toroidal rotation velocities as well as a methodology for estimating main ion toroidal rotation using perturbation theory were also provided.

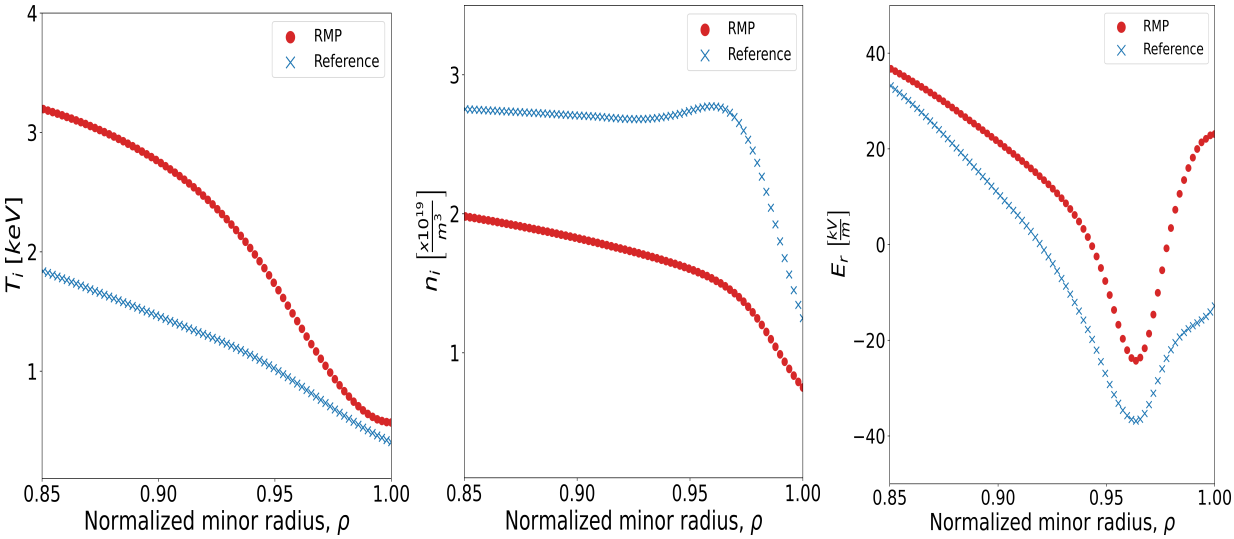

(a) (b) (c)

Figure 4.5: Plasma profiles for shot 123301 (RMP) and 123302 (Reference H-mode) at approximately 2800 ms. (a) Plasma ion temperature. (b) Plasma ion density in the edge. (c) Radial electric field.

We note that the RMP shot sees IOL occurring closer to the core than in the reference

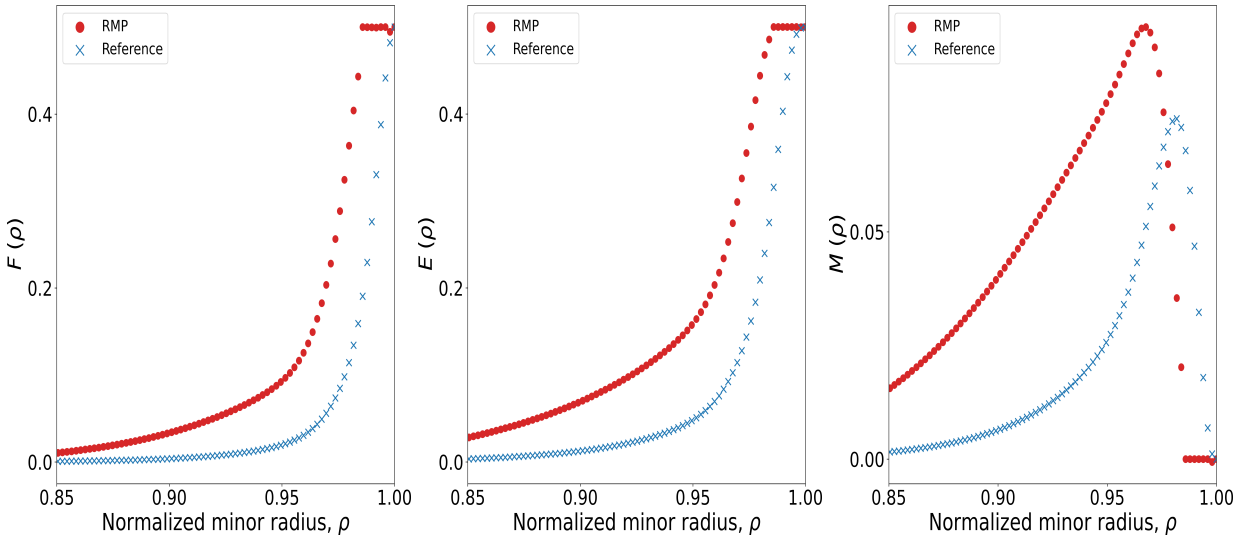

(a) (b) (c)

Figure 4.6: Ion Orbit Loss (IOL) profiles for shot 144977 in L- and H-modes. (a) Ion loss fraction. (b) Energy loss fraction. (c) Momentum loss fraction.

H-mode shot. This is likely due to the increased edge ion temperature seen in the RMP shot.

We will next observe the effects of IOL on a handful of QH-mode shots. Quiescent H-mode plasmas are of interest because this operating regime achieves H-mode levels of plasma performance, including high confinement. Importantly, QH-mode operation does not produce ELMs, thereby reducing transient spikes in heat and particle fluxes at the divertors. Figure 4.7 provides the plasma profiles for shots 163477 at 1800ms and 163518 at 2350ms. Shot 163477 is a standard QH-mode shot, while 163518 at 2350 ms is a wide-pedestal QH-mode shot. QH-mode shots at DIII-D are generally run in a reverse I_p (plasma current) mode and have a generally negative radial electric field. Figure 4.8 presents the IOL profiles for these two timeslices. Note the interesting results of shot 163518 in Figure 4.8. This shot has a relatively weak toroidal magnetic field and high

pedestal temperature $\approx 3.5keV$ at $\rho = 0.9$. Ions rather close to the core are finding themselves on loss orbits according to this analysis, likely due to the very high pedestal ion temperature.

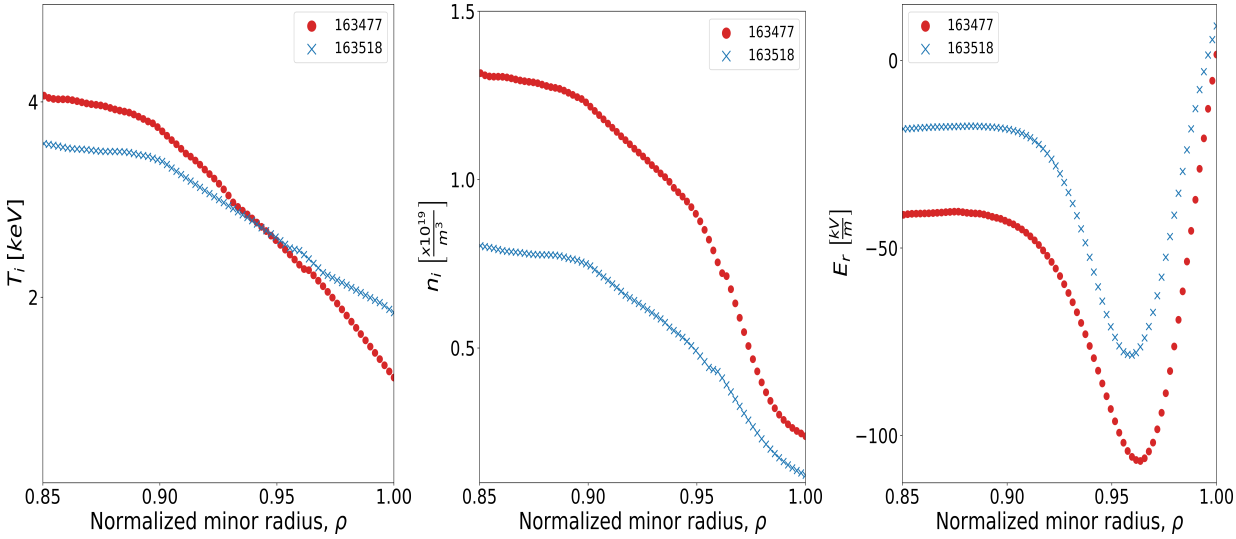

(a) (b) (c)

Figure 4.7: Plasma profiles for shots 163477 at 1800 ms and 163518 at 2350 ms. (a) Plasma ion temperature. (b) Plasma ion density in the edge. (c) Radial electric field.

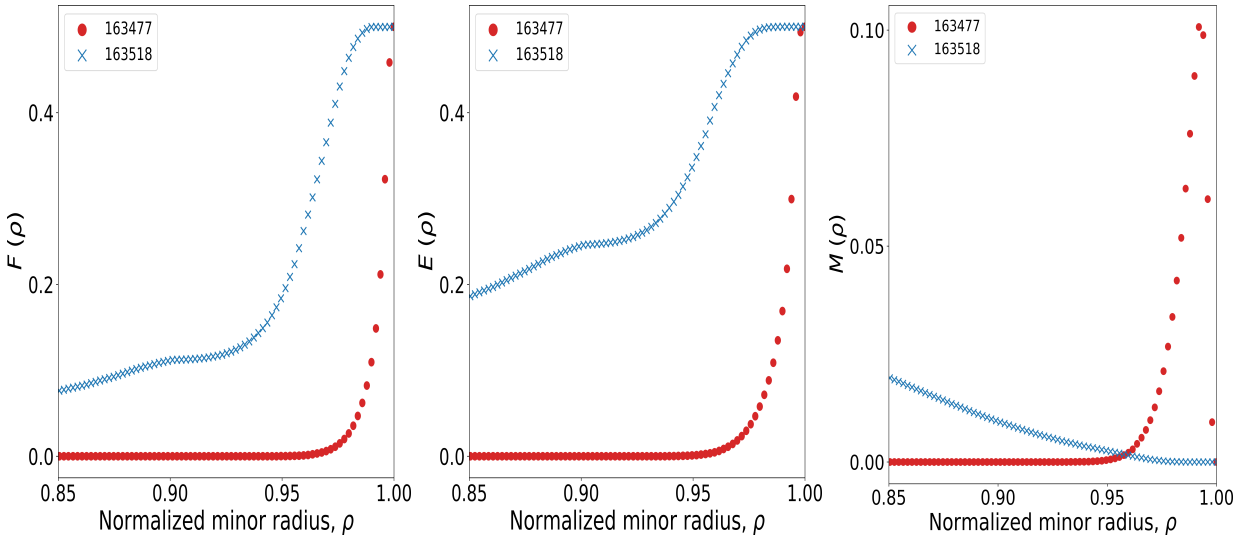

(a) (b) (c)

Figure 4.8: Ion Orbit Loss (IOL) profiles for shots 163477 at 1800 ms and 163518 at 2350 ms. (a) Ion loss fraction. (b) Energy loss fraction. (c) Momentum loss fraction.

Finally, we will observe IOL on a Super H-mode shot. Figure 4.9 shows the plasma profiles for shot 174783, a double-null plasma, during SH-mode operation at 2100 ms. Figure 4.10 shows that, despite the rather high ion temperature seen in Figure 4.9, IOL does not occur significantly deep into the core.

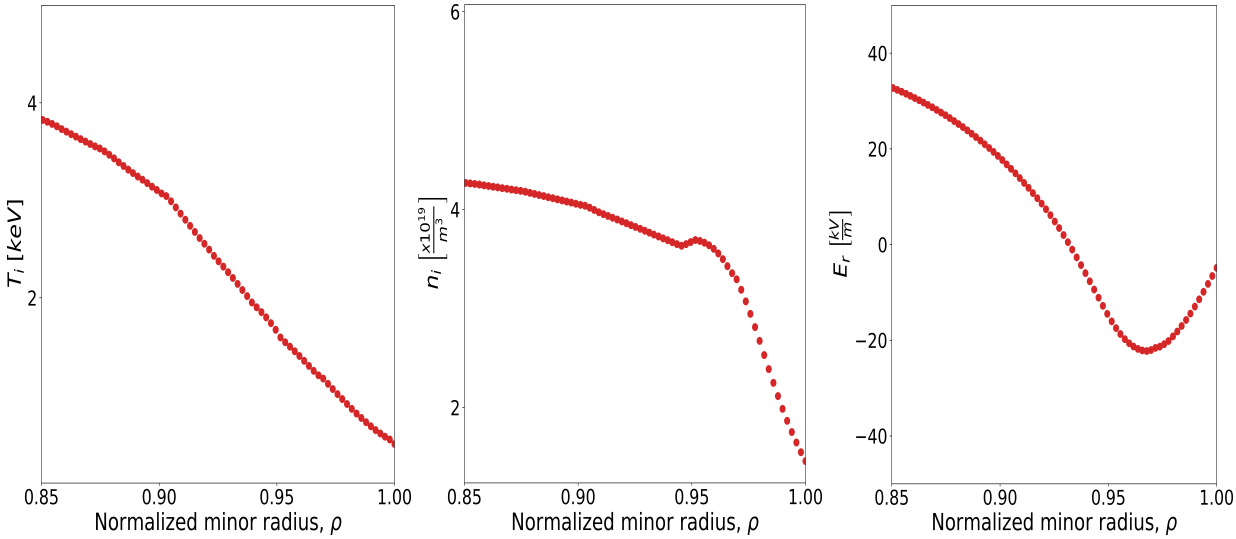

(a) (b) (c)

Figure 4.9: Plasma profiles for shot 174783 at 2100 ms. (a) Plasma ion temperature. (b) Plasma ion density in the edge. (c) Radial electric field.

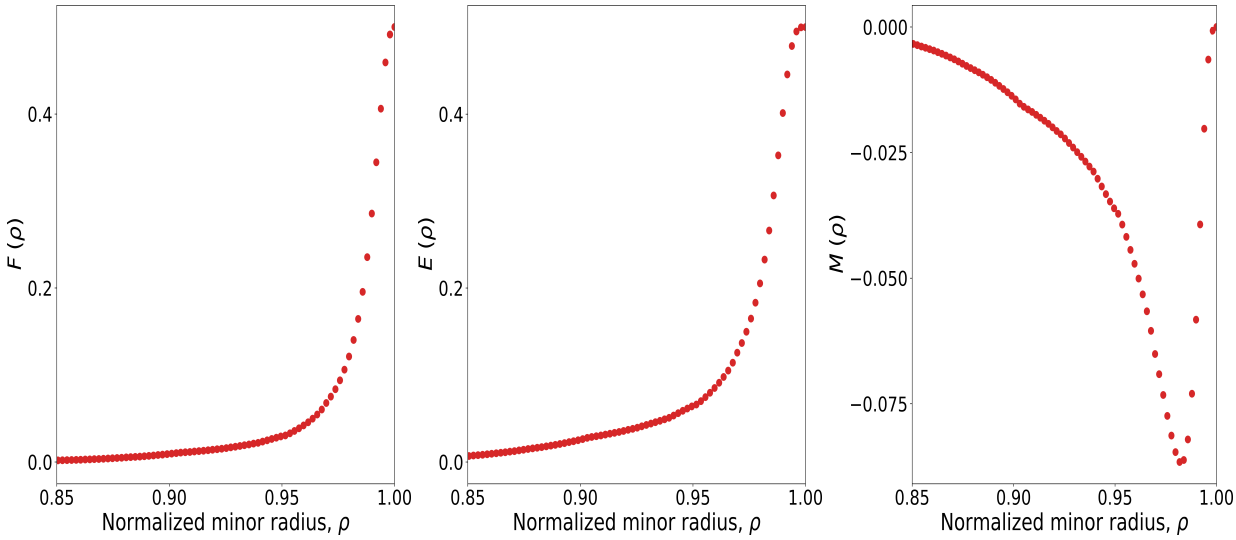

Figure 4.10: Ion Orbit Loss (IOL) profiles for shot 174783 at 2100 ms. (a) Ion loss fraction. (b) Energy loss fraction. (c) Momentum loss fraction.

4.5 Summary

This section discussed Ion Orbit Loss (IOL). IOL is a non-diffusive particle loss mechanism whereby ions can find themselves on loss orbits, i.e., orbits with sufficient energy to escape the plasma. IOL is calculated using conservation of energy and poloidal angular momentum. This phenomenon is found to be important in the edge of the plasma and represents a non-trivial particle and heat loss mechanism. At the very edge, approximately 50% of particles are lost to the plasma, thus representing an important correction in the calculations of the diffusive particle and conductive heat fluxes performed in this research. Specifically, it is clear that a large fraction of particles and energy in the edge plasma are transporting out non-diffusively, thereby affecting the accounting between diffusive vs. non-diffusive transport. In the next chapter, we will go over the basic plasma balance equations that

define the bulk of this thesis work.

CHAPTER 5

BALANCE EQUATIONS

5.1 Particle and Momentum Balance

This research is based on the use of particle and energy balance equations that conserve particle number and canonical angular momentum. The time-independent particle continuity equation for ion species j is

$$\nabla \cdot \Gamma_j \equiv \nabla \cdot n_j v_j = S_j + n_e \nu_{cx} + S_{nbi} - n_j \frac{\partial F_{iol}}{\partial r} \tag{5.1}$$

and the momentum balance equation is

$$\nabla \cdot (n_j m_j v_j v_j) + \nabla p_j + \nabla \cdot \pi_j = n_j e_j (\vec{v}_j \times B) + n_j e_j E + F_j + \hat{M}_j - n_j m_j \nu^i_{elcx,j} v_j \tag{5.2}$$

where Γ_j is the total particle flux of species j; n_j is the particle density of species j; v_j is the velocity of species j; S_j is the particle source term, defined as $S_j(r,\theta) = n_e(r,\theta) n_{j,0}(r,\theta) < \sigma v >_{ion} \equiv n_e(r,\theta)\nu_{ion}(r,\theta)$, in which $n_{j,0}$ is the local concentration of neutrals of species j, and n_e is the electron density; $\mathbf{E}$ is the electric field; $\mathbf{F_j}$ represents interspecies collisions; $\hat{\mathbf{M}}_\mathbf{j}$ is external momentum input corrected for IOL, and the last term represent momentum loss due to elastic scattering and charge exchange with neutrals.

To leading order, the radial component of Equation 5.2 can be written as

$$E_r^0 = \frac{1}{n_j^0 e_j}\frac{\partial p_j^0}{\partial r} + v_{\psi,j}^0 B_\theta^0 - v_{\theta,j}^0 B_\phi^0 \tag{5.3}$$

To obtain the radial flux surface averaged (FSA) toroidal component of Equation 5.2, we must evaluate the FSA toroidal viscous torque and inertial terms in the equation (see [27]). The neoclassical viscous torqu e can be written as the sum of "parallel", "gyroviscous" and "perpendicular" components. The FSA parallel component vanishes identically. Therefore, using the Stacey-Sigmar extension of the Braginskii gyroviscosity (see [75][76][77][78]) in a right-handed (ψ, θ,ϕ) toroidal flux surface coordinate system, the FSA toroidal viscous torque can be written as follows:

$$< R^2\nabla\phi\cdot\nabla\cdot\Pi >=< R^2\nabla\phi\cdot\nabla\cdot\Pi >_{gv} + < R^2\nabla\phi\cdot\nabla\cdot\Pi >_{\perp} \tag{5.4}$$

where

$$< R^2\nabla\phi\cdot\nabla\cdot\Pi >_{gv} = - < \frac{1}{Rh_p}\frac{\partial}{\partial l_\psi}\left(R^3 h_p \eta_4 \frac{\partial}{\partial l_p}(v_\phi/R)\right) > \tag{5.5}$$

$$< R^2\nabla\phi\cdot\nabla\cdot\Pi >_{\perp} = - < \frac{1}{Rh_p}\frac{\partial}{\partial l_\psi}\left(R^3 h_p \eta_2 \frac{\partial}{\partial l_p}(v_\psi/R)\right) > \tag{5.6}$$

Here, $\eta_2 = nT\tau/(\Omega\tau)^2$, $\eta_4 \approx (\Omega\tau)\eta_2 \approx (10^3 - 10^4)\eta_2$, $\Omega \equiv ZeB/m$, and τ is the collision time. Thus, the gyroviscous toroidal torque is in general a couple of orders of magnitude larger than the perpendicular toroidal viscous torque. Making a low-order Fourier expansion $X(r,\theta) = X^0(r)[1 + X^c cos\theta + X^s sin\theta]$ after approximating the flux surface geometry by a toroidal geometry allows Equation 5.5 and Equation 5.6 to be written

for species j as

$$< R^2\nabla\phi\cdot\nabla\cdot\Pi >_{gv,j} \approx \frac{1}{2}\eta_{4j}\frac{r}{R_0}(L_n^{-1}+L_T^{-1}+L_{v_\phi}^{-1})[(4+\tilde{n}_j^c)\tilde{v}_{\phi,j}^s+\tilde{n}_j^s(1-\tilde{v}_{\phi,j}^c)]v_{\phi,j}$$
$$\equiv R_0 n_j^0 m_j \nu_{gv,j} v_{\phi,j} \tag{5.7}$$

and

$$< R^2\nabla\phi\cdot\nabla\Pi >_{\perp,j} \approx R_0\eta_{2,j}[L_{v_\phi}^{-1}\left(\frac{1}{r}-L_{\eta_2}^{-1}\right)-\frac{1}{v_{\phi,j}}\frac{\partial^2 v_{\phi,j}}{\partial r^2}]v_{\phi,j} \equiv R_0 n_j^0 m_j \nu_{\perp,j} v_{\phi,j} \tag{5.8}$$

The poloidal asymmetry coefficients ($\tilde{n}_j^c \equiv n_j^c/\epsilon, etc.$) can be determined by solving the low-order Fourier moments of the poloidal component of Equation 5.2.

The turbulent, or "anomalous", toroidal viscous torque is usually assumed to be of the form of Equation 5.6 with an enhanced viscosity coefficient η_{anom}, giving

$$< R^2\nabla\phi\cdot\nabla\cdot\Pi >_{anom,j} \approx R_n\eta_{anom,j}\left[L_{v_\phi}^{-1}\left(\frac{1}{r}-L_{\eta_2}^{-1}\right)-\frac{1}{v_{\phi,j}}\frac{\partial^2 v_{\phi,j}}{\partial r^2}\right]v_{\phi,j}$$
$$\equiv R_0 n_j^0 m_j \nu_{anom,j} v_{\phi,j} \tag{5.9}$$

To obtain the inertial term in the FSA toroidal component of Equation 5.2, we use Equation 5.1 and obtain

$$< R^2\nabla\phi\cdot\nabla\cdot(n_j m_j \mathbf{v_j}\mathbf{v_j}) >=< R^2\nabla\phi\cdot n_j m_j(\mathbf{v_j}\cdot\nabla)\mathbf{v_j} > + R_0 n_j m_j \nu_{ion,j} v_{\phi,j} \tag{5.10}$$

The same set of approximations can be used to write the first term on the right as follows:

$$< R^2\nabla\phi \cdot n_j m_j(\mathbf{v_j}\cdot\nabla)\mathbf{v_j} >\equiv R_0 n_j m_j \nu_{n,j} v^0_{\phi,j} \tag{5.11}$$

The above can be used to write the FSA toroidal component of Equation 5.2 as

$$n^0_j m_j \nu^0_{jk}(1+\frac{\nu_{d,j}}{\nu^0_{jk}}v^0_{\phi,j} - v^0_{\phi,k}) = n^0_j e_j E^A_\phi + e_j B^0_\theta \Gamma_{r,j} + M^0_{\phi,j} \tag{5.12}$$

where $\nu_{d,j} \equiv \nu^{visc}_j + \nu^{iner}_j + \nu^{cx}_j + \nu^{ion}_j$ is a composite momentum loss frequency due to viscosity, inertia, charge exchange, and ionization.

Combining Equation 5.3 with Equation 5.12 yields a generalized pinch-diffusion relation for the radial particle flux of ion species j with impurity species k.

$$\Gamma_{r,j} \equiv < n_j v_{r,j} >= n_j D_{jj}\left(L^{-1}_{n,j} + L^{-1}_{T,j}\right) - n_j D_{jk}\left(L^{-1}_{n,k} + L^{-1}_{T,k}\right) + n_j v_{p,j} \tag{5.13}$$

with diffusion coefficients given by

$$D_{jj} \equiv \frac{m_j T_j\left(\nu^*_{d,j} + \nu_{jk}\right)}{(e_j B_\theta)^2}, D_{jk} \equiv \frac{m_j T_k \nu_{jk}}{e_j e_k (B_\theta)^2} \tag{5.14}$$

where the pinch velocity is given by

$$n_j v_{p,j} \equiv -\frac{M_{\phi,j}}{e_j B_\theta} - \frac{n_j E^A_\phi}{B_\theta} + \frac{n_j m_j \nu^*_{d,j}}{e_j B_\theta}\left(\frac{E_r}{B_\theta}\right) + \frac{n_j m_j f^{-1}_p}{e_j B_\theta}((\nu_{jk}+\nu^*_{d,j})v_{\theta,j} - \nu_{jk} v_{\theta,k}) \tag{5.15}$$

If we assume that there is only one impurity species in local thermal equilibrium with the ion species, the effective main ion diffusion coefficient can be written

$$D_j = \frac{m_j T_j \nu_{j,k}}{(e_j B_\theta)^2} \left[1 + \frac{\nu^*_{d,j}}{\nu_{j,k}} - \frac{Z_j}{Z_i}\right] \tag{5.16}$$

5.2 Energy Balance

In the remainder of this chapter, we will focus on a single-species plasma and use the subscript i to refer to the ions.

The Fourier heat conduction relation can be written

$$q^{\text{cond}} = -\chi n \left(\frac{\partial T}{\partial r}\right) \tag{5.17}$$

The total radial heat flux, Q^{tot}, can be written as a conductive component and a non-conductive component: $Q_i^{\text{tot}} = q^{\text{cond}} + Q^{\text{non-cond}}$.

To obtain the total radial heat flux, taking the third velocity moments of Equation 5.2, the energy balance on the plasma for the ions and electrons can be written as

$$\frac{\partial Q_i^{tot}}{\partial r} = -\frac{\partial}{\partial t}\left(\frac{3}{2} n_i T_i\right) + q_{nbi} - \frac{3}{2}(T_i - T_0^c) n_i n_0^c < \sigma v >_{cx+el} - q_{ie} \tag{5.18}$$

$$\frac{\partial Q_e^{tot}}{\partial r} = -\frac{\partial}{\partial t}\left(\frac{3}{2} n_e T_e\right) + q_{nbe} + q_{ie} - n_e n_0 < \sigma v >_{ion} E_{ion} - n_e n_z L_z \tag{5.19}$$

where $Q_i^{tot}(Q_e^{tot})$ is the total radial ion (electron, respectively) heat flux, q_{nbi} represents neutral beam injector (NBI) ion heating, q_{nbe} represents the NBI electron heating term, $q_{ie}(q_{ei})$ is the collisional heat exchange from ions to electrons (electrons to ions, respectively),

the $cx + el$ subscript represents charge-exchange plus elastic scattering, and the superscript c represents cold (uncollided) neutrals. Equation 5.17 can be re-written

$$\chi_i = \frac{q_i^{\text{cond}} \left(-\frac{1}{T_i} \frac{\partial T_i}{\partial r} \right)^{-1}}{n_i T_i} = \frac{q_i^{cond} L^{-1}}{n_i T_i} \tag{5.20}$$

where χ_i is the heat conductivity coefficient. A similar equation holds for the electrons.

Generally, the non-conductive component is simply written as $Q^{\text{non-cond}} = Q^{\text{conv}} = \frac{3}{2}\Gamma_r T$, where Q^{conv} is the convective radial heat flux. This formulation ignores other non-diffusive mechanisms that become important in the edge plasma.

The fully corrected q^{cond}, where $\hat{Q}^{\text{tot}}$ is corrected for IOL, can be written as follows:

$$q^{\text{cond}} = \hat{Q}^{\text{tot}} - Q^{\text{conv}} - Q^{\Pi} - Q^{\text{heatin}} - Q^{\text{visc}} \tag{5.21}$$

where

$$Q_i^{\text{conv}} = \frac{3}{2} \hat{\Gamma}_{r,i} T_i^{\text{exp}} \tag{5.22}$$

$$Q_i^{\Pi} = \hat{\Gamma}_{r,i} T_i^{\text{exp}} \tag{5.23}$$

$$Q_i^{\text{heatin}} = \frac{1}{2} n_i m_i \left(\vec{V}_i \cdot \vec{V}_i \right) V_{r,i} = \frac{1}{2} \hat{\Gamma}_{r,i} m_j \vec{v}^2 \tag{5.24}$$

To obtain the viscous heating term, we do a Fourier expansion $V(r,\theta) \approx V^0(r)(1 + V^s sin\theta + V^c cos\theta)$ and obtain

$$Q_i^{\text{visc}} \approx \frac{1}{R_0} V_{\phi,i}^0 V_{\phi,i}^s [\eta_0 f_p V_{r,i}^0 - \eta_{4,i}(2V_{\phi,i}^0 + \frac{1}{2}V_{\theta,i}^0] - \frac{1}{2}V_{\theta,i}^0 V_{\theta,i}^s [\eta_{0,i} V_{r,i}^0 + \eta_{4,i}(V_{\phi,i}^0 + \frac{1}{2}V_{\theta,i}^0)] \tag{5.25}$$

where $f_p = B_\theta / B_\phi$, and η_0, η_4 are Braginskii's parallel and gyroviscosity coefficients, respectively, the former being extended to the banana-plateau regime,

$$\eta_{0,i} = \frac{n_i m_i V_{\theta,i} q R \epsilon^{-3/2} \nu_i^*}{(1 + \epsilon^{-3/2}\nu_i^*)(1 + \nu_i^*)} \tag{5.26}$$

$$\eta_{4,i} = \frac{n_i T_i}{\Omega_i} \tag{5.27}$$

in which $\Omega_i = Z_i e B / m_i$, $\nu^* = \nu_{90} q R_{0,a} / V_{th,i}$, and $\epsilon = a / R_0$.

5.3 Summary

This chapter demonstrated how the particle and momentum balance equations could be used to solve for the total radial particle flux in a form that explicitly shows a diffusive and non-diffusive component. The non-diffusive component is proportional to the pinch velocity, a term that can be solved for using experimental data. The diffusion coefficients are given by Equation 5.14. This chapter also demonstrated that the energy balance equation could be used to solve for the total radial heat flux. Then, the non-conductive terms (convective heating, inertial heating, etc.) were presented. The non-conductive radial heat fluxes can be subtracted from the total radial heat flux to obtain the radial conductive heat flux, which allows one to interpret a radial heat conductivity coefficient: χ_r. In the

next chapter, we will discuss the framework used in GTEDGE2 to calculate the transport coefficients discussed in this chapter.

CHAPTER 6

INTERPRETATION METHODOLOGY

6.1 Interpretation of DIII-D Data

This work utilizes data from the DIII-D tokamak. Briefly, the data from DIII-D are processed using various automated and manual processes. Subsequently, data users can utilize these reduced data for interpretive work. This PhD research utilizes the GTEDGE2 code from the Fusion Research Center at Georgia Tech to perform interpretive work on DIII-D data. This code utilizes radial profiles of the ion/electron density and temperature distributions, the toroidal and poloidal carbon velocity distributions, and various 0-D parameters such as the toroidal magnetic field at the magnetic axis, the NBI power, the plasma radius, etc. The GTEDGE2 code is available for use with Python 2.7 and Python 3.8. NBI deposition profiles are generated using a Python port of the NBEAMS code [79], also developed previously at the Fusion Research Center.

6.2 Background Plasma

To generate the background plasma, the GTEDGE2 code takes in 2- and 3-column (ρ, val and R,Z,val) data of the ion and electron densities and temperatures, the radial electric field, 2D ψ data, and toroidal and poloidal ion velocities of the impurity and/or main ions.

The R,Z coordinates of the vessel wall are also required. GTEDGE2 can also utilize profiles of q and of densities and temperatures for impurities such as C, Ne, W, and Be. Note that GTEDGE2 is meant to be reactor agnostic and could theoretically be used for any tokamak. The `Shapely`[1] and `matplotlib` packages are used to generate the flux surfaces from the ψ data and find the x-point(s), strike points, magnetic and geometric axes, elongation, triangularities, q, and the separatrix, as shown in Figure 6.1. GTEDGE2 is also able to utilize 2D data for the plasma profiles, although the work in this dissertation utilized 1D data.

We note that this work utilizes flux-surface averaging (FSA) of various quantities. In general, on a flux surface ψ, the FSA of a quantity A, denoted $< A >_\psi$, is given by

$$< A >_\psi \equiv \oint_\psi \frac{A dl_p}{B_p} / \oint_\psi \frac{dl_p}{B_p} \tag{6.1}$$

where dl_p is the infinitesimal distance poloidally along the flux surface and B_p is the poloidal magnetic field.

6.3 Ion Orbit Loss

After the background plasma is generated, the `IOL` module generates the Ion Orbit Loss (IOL) profiles for the plasma. The module uses a user-defined number of launch angles off a flux surface and performs the calculations found in chapter 4. Loss profiles are generated for the particle number, energy, and momentum loss fractions for deuterium,

[1]The `Shapely` Python package is a package for the manipulation and analysis of planar geometric objects.

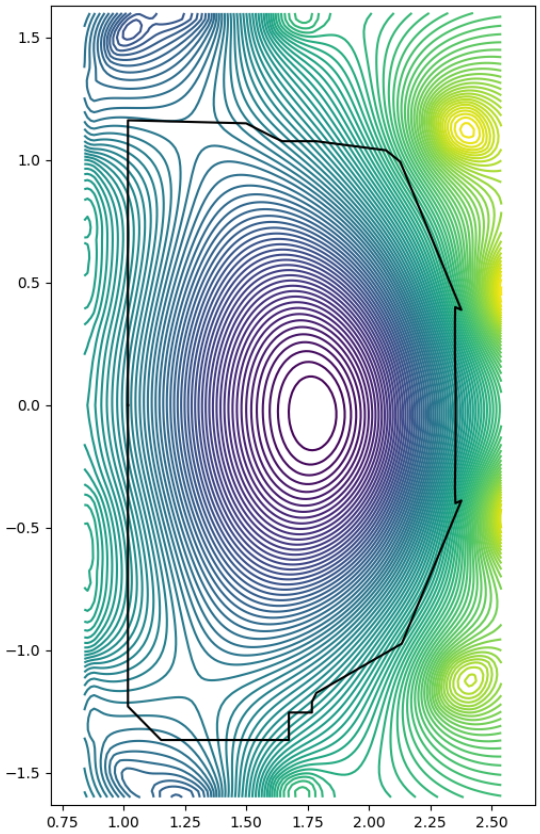

Figure 6.1: Example mapping of 2D flux surfaces in GTEDGE2. GTEDGE2 takes in R,Z flux values and calculates important plasma parameters such as the magnetic and geometric axes, elongation, etc.

tritium, carbon, and alphas. These calculations can be expanded to other ions. The `IOL` module performs separate calculations for thermalized (e.g., plasma) ions and monoenergetic (e.g., neutral-beam-injected) ions, with the latter performed for each molecular species and beam energy for the beam ions. The `IOL` module can easily be extended to additional impurity species, as the IOL calculations are simply a function of the charge-to-mass ratio ($\frac{q}{m}$).

6.4 Neutral Beam Injection

The `BeamDeposition` module is a Python port of the neutral beam heating aspect of the NBEAMS [79] FORTRAN90 neutral beam heating and current drive code. NBEAMS uses a diffuse-beam model for beam modeling. The `BeamDeposition` code takes as input the background plasma as well as an input file containing the beam width, radius of tangency, ion mass, ion energy, direction (co-current or counter-current w.r.t. the plasma current) and beam power of each beam. By default, the power fractions (i.e., the fraction of the beam power constituted by the molecular ions, e.g., D, D_2, and D_3) are calculated assuming deuterium launched at approximately 80 keV using an empirical fit from DIII-D. Note that these power fractions can be overwritten in the beam data file for use with different NBI configurations.

The `BeamDeposition` module attempts to calculate the number of atoms ionized within a toroidal volume element $V'(r)dr$:

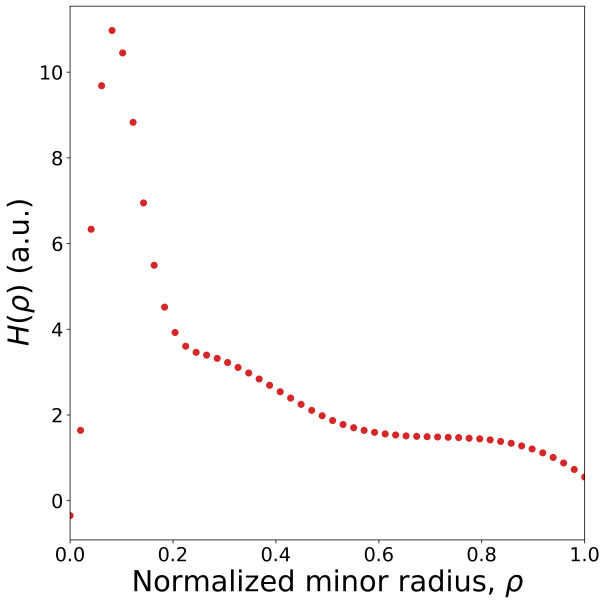

Figure 6.2: Typical deposition profile of deuterium ions calculated by GTEDGE2

$$\frac{I_0/e}{V_p} H(r) V'(r) dr \tag{6.2}$$

where I_0 is the injection current, V_p is the plasma volume, and $H(r)$ is the neutral beam deposition profile. The fast ion source for the plasma is

$$S_{nbi} = \frac{I_0/e}{V_p} H(r) \tag{6.3}$$

$H(r)$ is calculated and used to provide the beam particle and energy sources in the plasma, as will be discussed later. An example deposition profile, $H(r)$, is shown in Figure 6.2. Note that the `BeamDeposition` module is coupled to the `IOL` module and applies an IOL correction to each species of injected ion.

6.5 Neutral Recycling

An important fueling mechanism for the plasma is neutral particles coming off the vessel wall and divertor. This neutral recycling creates a particle source as neutral ions interact with the hot plasma, and it creates an energy sink as these new colder ions enter the plasma. The `Neutrals` module utilizes the `GTNEUTPY`[3] neutrals package[2] to calculate the neutral density and ionization rates for the plasma. `GTNEUTPY` is a Python port of the GTNEUT code, which is based on the transmission-and-escape probability (TEP) method. The Python port can utilize multiple CPUs, greatly reducing the calculation time of the density on a grid of thousands of cells to a few minutes.

6.6 Radial Transport

The `RadialTransport` module contains the main calculations for the interpretations performed in this work. First, the particle flux in the particle balance is calculated by using the `SciPy` ODE integrator to solve, in a 1-D (slab) geometry,

$$\frac{d\hat{\Gamma}_i}{dr} = n_e(r)\nu_{ion}(r) + n_e(r)\nu_{cx}(r) + S_{nbi} - \hat{\Gamma}_i \frac{dF_{iol}}{dr} \tag{6.4}$$

where $\hat{\Gamma}$ is the IOL-corrected particle flux of thermalized main ions, n_e is the electron density, ν_{ion} is the ionization rate, ν_{cx} is the rate of charge exchange, S_{nbi} is the neutral beam particle source (corrected for IOL), and $\frac{dF_{iol}}{dr}$ is the differential particle loss fraction.

[2] `GTNEUTPY` is a Python port of the GTNEUT neutrals code.

Similarly, the total heat flux for the ions and electrons is calculated from energy balance in a 1-D (slab) geometry as

$$\frac{d\hat{Q}_i^{tot}}{dr} = q_{nbi} - \frac{3}{2}(T_i - T_0^c) n_i n_0^c < \sigma v >_{cx+el} - q_{ie} - \hat{Q}_i^{tot} \frac{dE^{iol}}{dr} \tag{6.5}$$

$$\frac{dQ_e^{tot}}{dr} = q_{nbe} + q_{ie} - n_e n_0 < \sigma v >_{ion} E_{ion} - n_e n_z L_z \tag{6.6}$$

where $\hat{Q}_i^{tot}(Q_e^{tot})$ is the IOL-corrected total radial ion (electron[3], respectively) heat flux, $q_{nbi}(q_{nbe}$) represents NBI ion (electron, respectively) heating, $q_{ie}(q_{ei})$ is the collisional heat exchange from ions to electrons (electrons to ions, respectively), $\frac{dF^{iol}}{dr}$ and $\frac{dE^{iol}}{dr}$ are the differential loss fractions for the particle number and energy, $n_e n_z L_z$ is the radiative energy losses due to impurities, the $cx{+}el$ subscript represents charge-exchange plus elastic scattering, and the superscript c represents cold (uncollided) neutrals.

To correct for non-diffusive and non-conductive phenomena, we calculate various terms. The convective heating is simply calculated as

$$Q_j^{\text{conv}} = \frac{3}{2} e \hat{\Gamma} T_j \tag{6.7}$$

where e is the electron charge, $\hat{\Gamma}$ is the IOL-corrected radial ion particle flux, and T_j is in units of eV.

The work done by the flowing plasma on the pressure tensor is given by

$$Q_j^{\Pi} = e \hat{\Gamma} T_j \tag{6.8}$$

[3]electrons do not have an IOL correction, as they are bound too tightly to the plasma to be lost in this manner.

The viscous heating term is

$$Q_j^{\text{visc}} \approx \frac{1}{R_0} V_{\phi,j}^0 V_{\phi,j}^s [\eta_0 f_p V_{r,j}^0 - \eta_{4,j}(2V_{\phi,j}^0 + \frac{1}{2}V_{\theta,j}^0)] - \frac{1}{2} V_{\theta,j}^0 V_{\theta,j}^s [\eta_{0,j} V_{r,j}^0 + \eta_{4,j}(V_{\phi,j}^0 + \frac{1}{2}V_{\theta,j}^0)] \quad (6.9)$$

where R_0 is the major radius at the magnetic axis, $V_{\phi,j}^0$ and $V_{\theta,j}^0$ are the toroidal and poloidal ion velocity, $V_{\theta,j}^s$ and $V_{\phi,j}^s$are the levels of asymmetry assumed in $V(r,\theta) \approx V^0(r)(1 + V^s sin\theta + V^c cos\theta)$, $f_p = B_\theta/B_\phi$, and η_0, η_4 are Braginskii's parallel and gyroviscosity coefficients, respectively,

$$\eta_{0,i} = \frac{n_j m_j V_{\theta,j} q R \epsilon^{-3/2} \nu_j^*}{(1 + \epsilon^{-3/2}\nu_j^*)(1 + \nu_j^*)} \quad (6.10)$$

$$\eta_{4,i} = \frac{n_j T_j}{\Omega_j} \quad (6.11)$$

in which $\Omega_j = Z_j eB/m_j$, $\nu^* = \nu_{90} q R_{0,a}/V_{th,j}$, and $\epsilon = a/R_0$.

The inertial heating term is simply given by

$$Q_j^{\text{heatin}} = \frac{1}{2}\hat{\Gamma}_j m_j v_{th}^2 \quad (6.12)$$

With the above, we can then calculate $\chi_{r,j}$ as

$$\chi_{r,j} = \frac{(\hat{Q}_j^{\text{tot}} - Q^{\text{conv}} - Q^{\Pi} - Q^{\text{heatin}} - Q^{\text{visc}}) L_{T,j}}{n_j^{\text{exp}} T_j^{exp}} \quad (6.13)$$

where $L_{T,j} = -\frac{T^{\text{exp}}}{\nabla T^{\text{exp}}}$ is the gradient scale length, n_j^{exp} is the experimental ion density, and T_j^{exp} is the experimental ion temperature.

To calculate an ion particle diffusion coefficient, we first calculate a composite momentum

loss frequency, $\nu_{d,i}$, that satisfies momentum balance (see Equation 5.12):

$$\nu_{d,j} = \frac{n_j e_j E_\phi^A + e_j B_\theta \Gamma_{r,j} + M_{\phi,j} + n_j m_j \nu_{jk} v_{\phi,k}}{n_j m_j v_{\phi,j}} - \nu_{jk} \tag{6.14}$$

Assuming one impurity species with the same radial profile and local temperature as the main ions allows us to write the diffusion coefficient

$$D_j \equiv \frac{m_j T_j \nu_{jk}}{(e_j B_\theta)^2} \left[1 + \frac{\nu_{d,j}}{\nu_{jk}} - \frac{Z_j}{Z_k}\right] \tag{6.15}$$

and the pinch velocity, $v_{p,j}$,

$$n_j v_{p,j} = -\frac{M_{\phi j}}{e_j B_\theta} - \frac{n_j E_\phi^A}{B_\theta} + \frac{n_j m_j \nu_{d,j}}{e_j B_\theta}\left(\frac{E_r}{B_\theta}\right) + \frac{n_j m_j f_p^{-1}}{e_j B_\theta}((\nu_{jk} + \nu_{d,j}) v_{\theta,j} - \nu_{jk} v_{\theta,k} \tag{6.16}$$

In the next chapter, we will present the results obtained for various shots using the GTEDGE2 code for our interpretation of the radial transport coefficients. The figures in the next chapter will present our inferred values of D_j, $v_{p,j}$, as well as the values of χ_j using 6 formulations, each progressively correcting for an additional non-conductive heat transport mechanism:

1. χ_j calculated assuming $q^{\text{cond}} = Q^{\text{tot}}$ w/out IOL Correction, i.e., all energy transporting out of the plasma is conductive, and our IOL corrections are not applied.

2. χ_j calculated assuming $q^{\text{cond}} = Q^{\text{tot}}$ w/ IOL Correction, i.e., all energy transporting out of the plasma is conductive, and our IOL corrections are applied.

3. χ_j calculated assuming $q^{\text{cond}} = Q^{\text{tot}} - Q^{\text{conv}}$, i.e., same as above but also correcting

for the convective flow of thermal energy.

4. χ_j calculated assuming $q^{\text{cond}} = Q^{\text{tot}} - Q^{\text{conv}} - Q^{\Pi}$, i.e., same as above but also correcting for the work done by the flowing plasma on the pressure tensor.

5. χ_j calculated assuming $q^{\text{cond}} = Q^{\text{tot}} - Q^{\text{conv}} - Q^{\Pi} - Q^{\text{heatin}}$, i.e., same as above but also correcting for the outflow of rotational (i.e., inertial) energy.

6. χ_j calculated assuming $q^{\text{cond}} = Q^{\text{tot}} - Q^{\text{conv}} - Q^{\Pi} - Q^{\text{heatin}} - Q^{\text{visc}}$, i.e., same as above but also correcting for viscous heating.

Note that the transport of rotational energy, Q^{heatin}, in the analyzed shots is generally quite small relative to the other non-diffusive radial heat fluxes, making formulations 4 and 5 fairly indistinguishable in the results.

6.7 Impurities and Limitations

We briefly note the limitations of this model and also discuss how impurities are handled. In the calculation of the background plasma, GTEDGE2 assumes that impurities enter the plasma at the separatrix fully stripped of electrons. In general, the electron density data are used to calculate the main ion densities and carbon densities. If Z_{eff} data are available, the carbon density can be calculated assuming fully stripped electrons; otherwise, a constant density fraction is assumed throughout the plasma. If carbon density data can be provided, carbon densities can be used directly.

The calculations of $D_{r,j}$ and $\chi_{r,j}$ assume one impurity species and that the impurity species has come into thermal equilibrium with the ions. This means that the calculation of $\chi_{r,j}$ is independent of the impurities, as there is no temperature difference to cause energy transfer between the main ion species and impurity species. The calculation of $D_{r,j}$ that will be presented in this thesis is the effective ion diffusion coefficient given by Equation 5.16. However, the model supports multiple impurity species, as discussed in section 5.1. It is also worth noting that the IOL calculations are estimates that assume a collisionless plasma. In certain plasmas, such as L-mode plasmas, a potentially significant number of ions may experience collisions before transporting out of the plasma and thus would be considered part of a diffusive flux.

6.8 Summary

In this chapter, our interpretation methodology was discussed. This chapter mainly focused on the interpretation method used by the GTEDGE2 software package. The background plasma is generated using experimental main ion densities, temperatures, and rotational velocities, along with various 0-D parameters such as the toroidal magnetic field, as well as the experimental psi values. The particle and heat sources and sinks are generated by various modules in GTEDGE2. These sources and sinks allow us to calculate inferred particle and heat fluxes, which allow us to infer particle diffusion and heat conductivity coefficients. In the next chapter, the results from GTEDGE2 using data from various shots

obtained will be presented. Note that a more detailed manual for GTEDGE2 can be found in Appendix B.

CHAPTER 7

IMPROVED INTERPRETATION

7.1 Non-conductive Heat Fluxes

In this chapter, we will present how the above corrections produce significant differences in the inferred χ_r compared to the situation where χ_r is calculated assuming all heat is transporting out in a conductive manner. First, we present the heat and particle fluxes when corrected for IOL. The IOL correction comes into Equation 6.4 and Equation 6.5 as essentially particle and heat sinks, respectively. We will then present the various heat fluxes that correspond to the non-conductive heat transport mechanisms. It will be clear that, in most cases presented, non-conductive heat fluxes are significant; thus, it is clear that the usual way of thinking of transport, i.e., all particles diffuse and all heat conducts, is not telling the whole story. We subtract these non-conductive heat fluxes from the total heat flux so that we can obtain $q_{r,j}^{cond}$, which leads us to $\chi_{r,j}$, the ion heat conductivity coefficient. These results will be used in chapter 9 to compare with theoretical calculations of $\chi_{r,j}$ to demonstrate that correcting for these non-conductive mechanisms is essential to obtaining a theoretical understanding of edge conductive heat transport.

Figure 7.1 shows the IOL-corrected radial particle and heat fluxes for DIII-D RMP reference shot 123302 at 2810 ms in H-mode. These profiles are calculated by solving

Equation 6.4 and Equation 6.5 for the radial ion particle flux ($\Gamma_{r,j}$) and ion heat flux ($Q^{tot}_{r,j}$). The profiles indicated as "w/ IOL" are obtained with the IOL correction, and the profiles indicated as"w/out IOL" are obtained without the IOL correction to demonstrate the importance of this correction. As seen, the IOL correction significantly reduces the radial conductive heat flux, as well as the diffusive particle flux, in the edge plasma. This is because IOL is essentially a particle sink, i.e., ions are finding themselves on orbits that will take them beyond the LCFS and make them be lost to the plasma. The particle flux calculation is important here for the interpretation of $\chi_{r,j}$ because it also drives the convective heat flux, i.e., $Q^{conv}_{r,j} = \frac{3}{2} n_j T_j$, and the work done on the pressure tensor, Q, which will be seen to be an important transport mechanism that must be corrected for when interpreting $\chi_{r,j}$. Again, we note that this does not mean that less energy is being transported out but rather that significant amounts of energy are being transported out in ways that do not simply satisfy a Fourier-type relation.

We now give the radial ion heat conductivity coefficient, $\chi_{r,j}$, and the various radial ion heat fluxes, $Q_{r,j}$, in Figure 7.2. In the left panel, we see the total radial heat flux, indicated by ●; the total radial heat flux when we correct for IOL, indicated by × ; the convective heat flux (Equation 5.22), indicated by +; work done by the flowing plasma on the pressure tensor (Equation 5.23), indicated by ◆; the heat flux of rotational energy being transported out of the plasma (Equation 5.24), indicated by ▼; and the viscous heating (Equation 5.25), indicated by ▲. These heat fluxes show that there are multiple significant, non-conductive

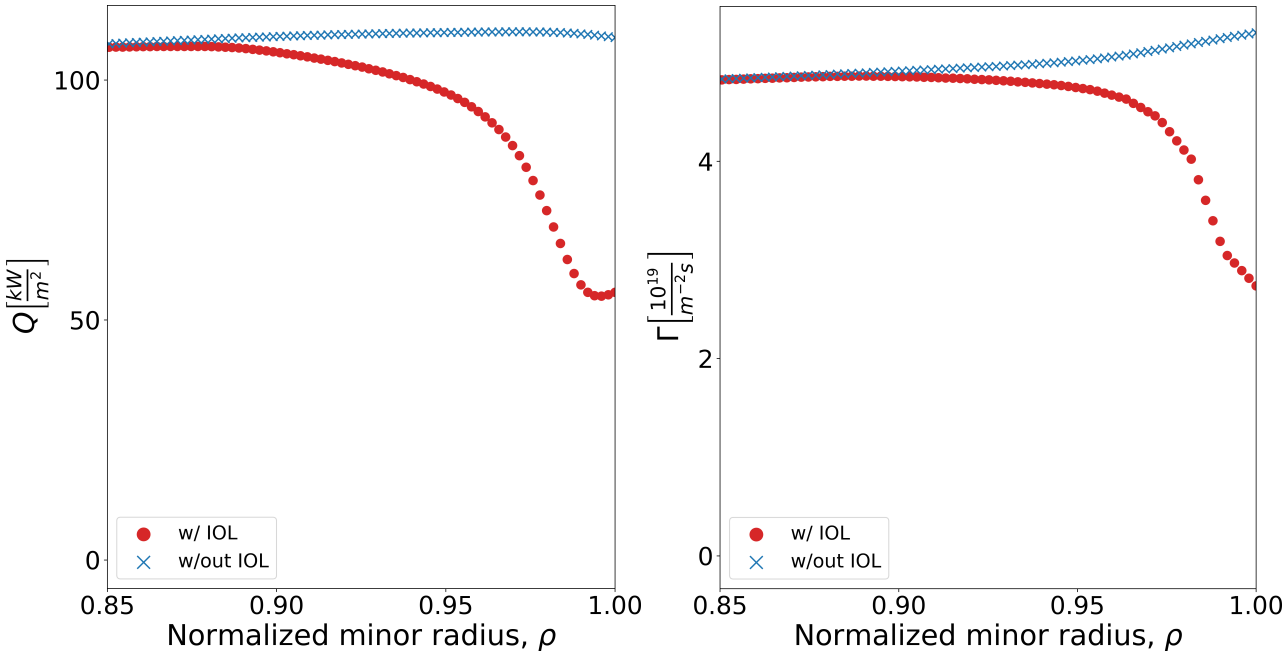

Figure 7.1: Inferred total heat (left) and particle (right) fluxes for shot 123302, the reference RMP H-mode plasma, corrected and not corrected for IOL.

heat transport mechanisms at work in the plasma. Q^{tot}, the total radial heat flux, is the sum of conductive and non-conductive heat fluxes. If one were to simply calculate Equation 5.20 using $q_i^{cond} = Q^{tot}$, or the total heat flux, the $\chi_{r,j}$ would be incorrect since it is a conductive transport coefficient being inferred from a heat flux that includes non-conductive transport mechanisms. Therefore, we have to take the total heat flux, Q^{tot}, and correct for IOL and then subtract the non-conductive transport mechanisms (Q^{visc}, Q^{conv}, Q^{Π} and Q^{heatin}). Only after we have made all these corrections can Equation 5.20 be computed correctly using a q^{cond} that is representative of only conductive heat flows.

We will present the inferred $\chi_{r,j}$ by subtracting each non-conductive heat flux from the total heat flux in successive calculations as follows to show which non-conductive heat flux mechanisms are the most important contributions. Note that in our calculations, a

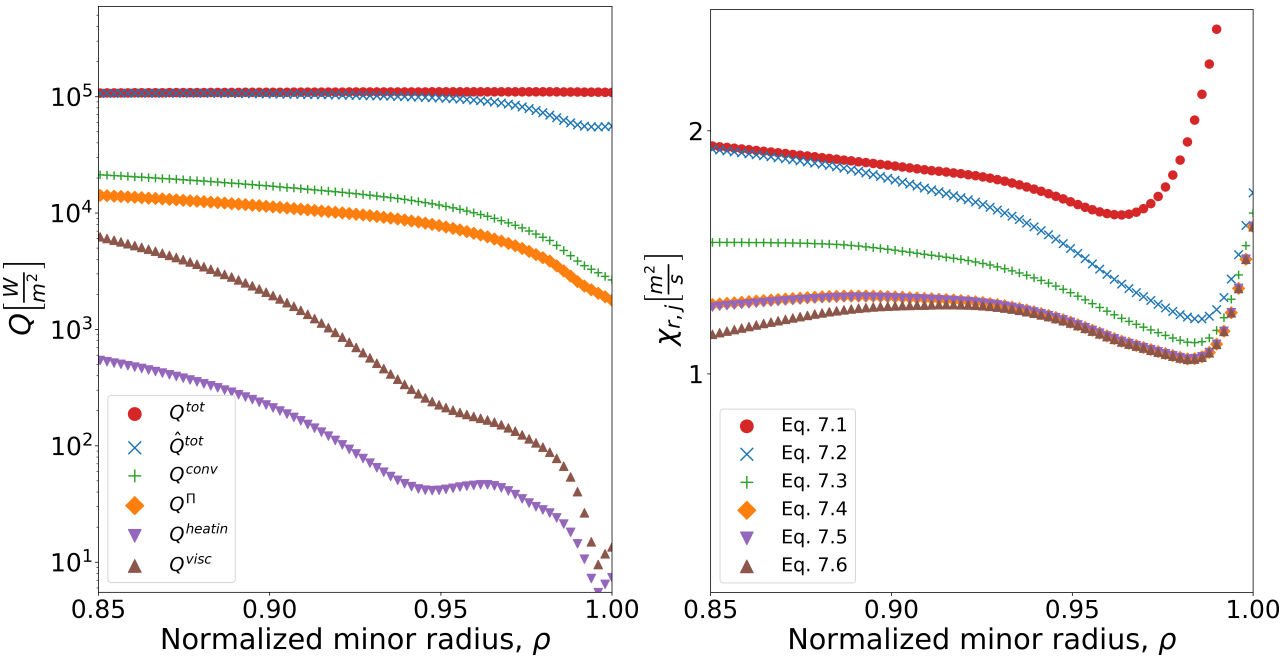

Figure 7.2: Inferred heat fluxes (left) and $\chi_{r,j}$ (right) for shot 123302, the reference RMP H-mode plasma discussed previously, with various non-conductive transport mechanisms corrected for.

2% asymmetry is considered in the rotational velocities to give one an idea about the potential magnitude of the viscous heat flux. In reality, one would require additional modeling or data to determine or infer the true asymmetries driving this heat flux. Note in Equation 7.1 and Equation 7.2 that the total heat flux is being inferred without (Q_j^{tot}) and with ($\hat{Q}_j^{\text{tot}}$) the IOL correction. Equation 7.3 through Equation 7.6 are the formulations whereby we subtract off an additional non-conductive radial heat flux from the total (with IOL correction) heat flux to demonstrate which heat fluxes create the greatest difference in the inferred $\chi_{r,j}$.

$$\chi_{r,j} = \frac{Q_j^{\text{tot}} L_{T,j}}{n_j^{\text{exp}} T_j^{exp}} \tag{7.1}$$

$$\chi_{r,j} = \frac{\hat{Q}_j^{\text{tot}} L_{T,j}}{n_j^{\text{exp}} T_j^{exp}} \tag{7.2}$$

$$\chi_{r,j} = \frac{(\hat{Q}_j^{\text{tot}} - Q^{\text{conv}}) L_{T,j}}{n_j^{\text{exp}} T_j^{exp}} \tag{7.3}$$

$$\chi_{r,j} = \frac{(\hat{Q}_j^{\text{tot}} - Q^{\text{conv}} - Q^{\Pi}) L_{T,j}}{n_j^{\text{exp}} T_j^{exp}} \tag{7.4}$$

$$\chi_{r,j} = \frac{(\hat{Q}_j^{\text{tot}} - Q^{\text{conv}} - Q^{\Pi} - Q^{\text{heatin}}) L_{T,j}}{n_j^{\text{exp}} T_j^{exp}} \tag{7.5}$$

$$\chi_{r,j} = \frac{(\hat{Q}_j^{\text{tot}} - Q^{\text{conv}} - Q^{\Pi} - Q^{\text{heatin}} - Q^{\text{visc}}) L_{T,j}}{n_j^{\text{exp}} T_j^{exp}} \tag{7.6}$$

By looking at Figure 7.2, we can see why the corrections made in our framework are important. The top scatter plot in the left panel is the total radial ion heat flux without any corrections. The second plot shows the same heat flux but corrected for IOL. In the far edge, approximately half of all ions are on loss orbits exiting the plasma. Next, we see the convective heat flux and work done on the pressure tensor being approximately 20% and 14%, respectively, of the total heat flux at $\rho \approx 0.85$. The viscous heating at 2% asymmetry is $\approx 5\%$ of the total radial ion heat flux at this flux surface. In other words, these three non-conductive heat fluxes are significant and must be subtracted from the total radial heat flux before calculating $\chi_{r,j}$. Note that the GTEDGE2 code, as used in this research, utilizes 1D radial profiles for the toroidal and poloidal velocities; thus, the asymmetry that drives the viscous heating is only assumed and is meant to provide an indication of whether viscous heating may play an important role in ion heat transport. We will show later situations

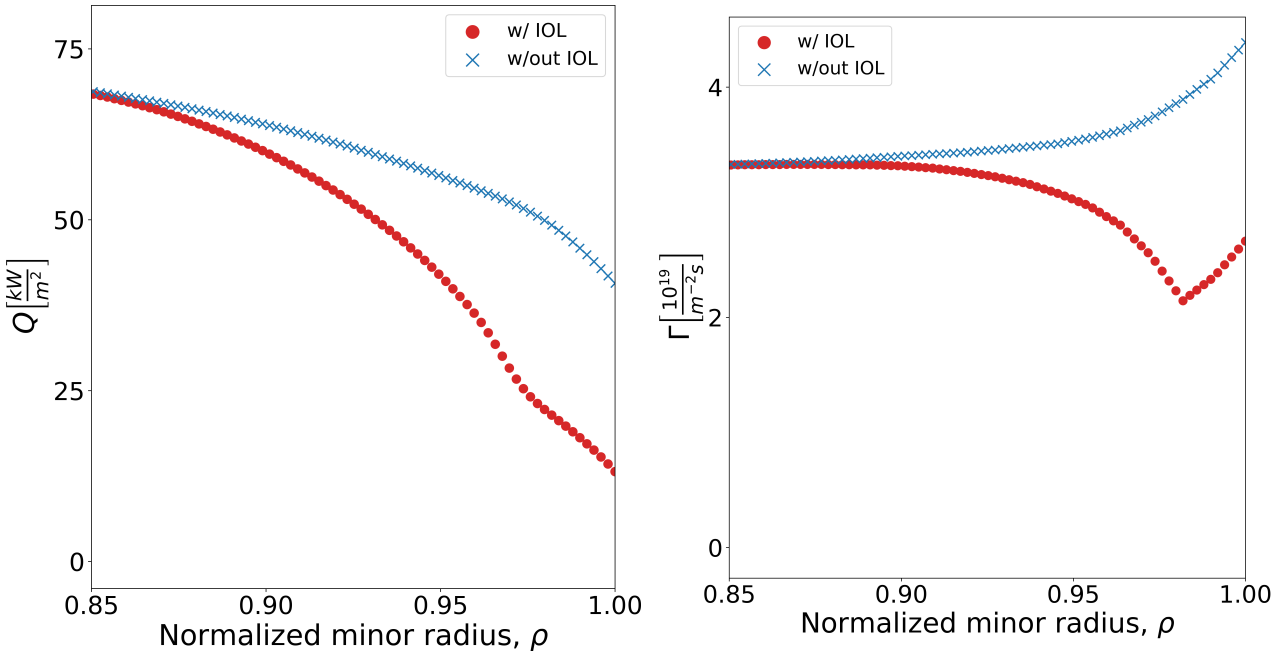

Figure 7.3: Inferred total heat (left) and particle (right) fluxes for shot 170672, a double-null negative-triangularity plasma, corrected and not corrected for IOL.

whereby viscous heating can be insignificant as well as situations whereby it plays an even more important role than in shot 123302.

As a second example, we do the same calculations for DIII-D shot 170672 at 1900ms. This shot is a negative triangularity plasma. Figure 7.4 shows our corrections of $\chi_{r,j}$ for this timeslice. Of note is the fact that negative triangularity shots are generally characterized by improved confinement despite the lack of edge pedestal [80]. Our modeling indicates that IOL greatly reduces the inferred conductive transport in the very edge (approximately 50% of the heat flux has been lost via IOL at $\rho > 0.975$). This may have important implications for understanding the mechanism behind the enhanced confinement that characterizes this shot regime. One may also wonder about sudden changes in particle and/or heat fluxes near the far edge in our analysis. This is often due to an interplay between IOL and NBI.

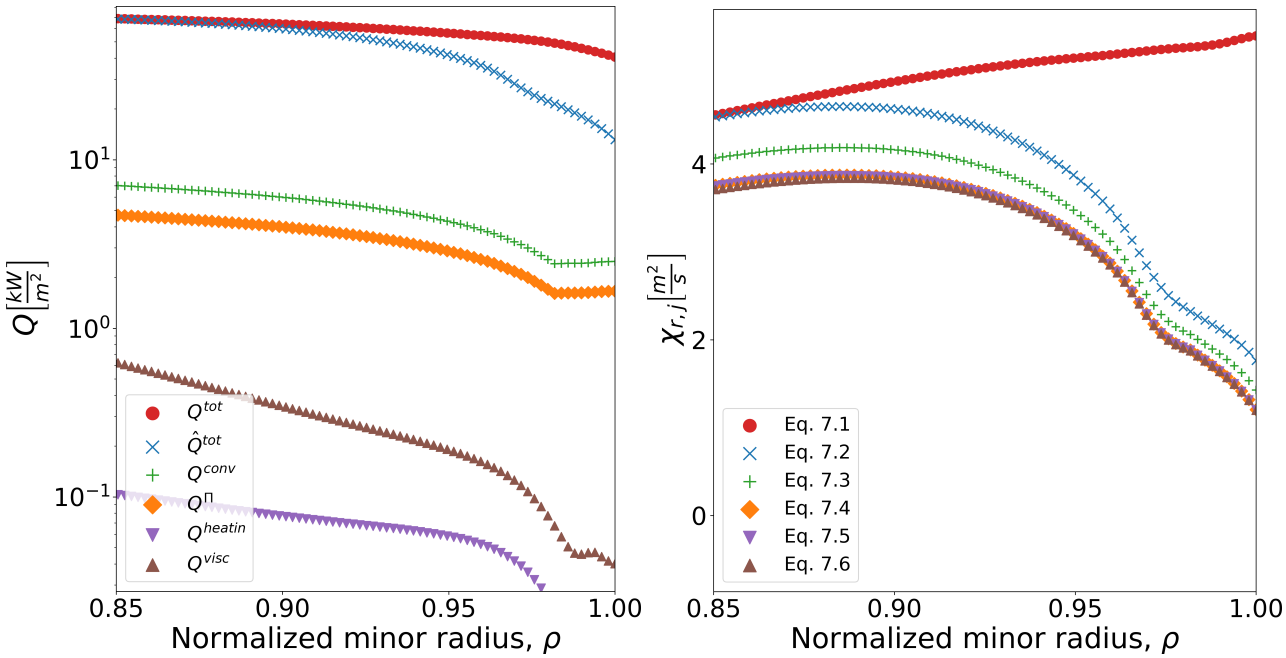

Figure 7.4: Inferred heat fluxes (left) and $\chi_{r,j}$ (right) for shot 170672, a double-null negative-triangularity plasma, with various non-conductive transport mechanisms corrected for.

Particles entering the plasma via NBI have separate deposition profiles and separate loss profiles. Specifically, each species of beam ion (or rather, atomic and molecular D/H) enters the plasma with very different velocities, and the ion velocity is an important factor in when ions can find themselves on loss orbits. In addition, beam ions are monoenergetic in the IOL framework; therefore, beam ions born on a given flux surface are either all lost or none are lost.

In the next chapter, we will apply this methodology to additional shot regimes.

7.2 Viscous Heating

In this section, we want to focus on the viscous heat flux discussed in the previous section. When approximating the rotational velocities as $V(r,\theta) = V^0(r)[1 + V^c cos\theta + V^s sin\theta]$ in a low-order Fourier expansion, the ion viscous heat flux is given by

$$Q_j^{\text{visc}} \approx \frac{1}{R_0} V^0_{\phi,j} V^s_{\phi,j} [\eta_0 f_p V^0_{r,j} - \eta_{4,j}(2V^0_{\phi,j} + \frac{1}{2}V^0_{\theta,j})] - \frac{1}{2} V^0_{\theta,j} V^s_{\theta,j} [\eta_{0,j} V^0_{r,j} + \eta_{4,j}(V^0_{\phi,j} + \frac{1}{2}V^0_{\theta,j})] \quad (7.7)$$

To demonstrate the potential effect rotational asymmetries may have, we plot the total radial ion heat fluxes for shot 144977 in H-mode (left) and L-mode (right) in Figure 7.5. In both panels, we give the total uncorrected radial ion heat flux, $Q^{\text{tot}}_{r,j}$ as well as the viscous heat flux for 3 different asymmetries. For example, the plot labeled $Q^{\text{visc}}_{r,j} - 2\%$ indicates that $V^c, V^s = 0.02$. These plots provide an idea of the magnitude of the viscous heating term if the Fourier expansion above represents a good approximation. At $\rho = 0.9$, 2%, 4%, and 6% asymmetries produce heat fluxes that represent 15%, 30%, and 45% of the total radial heat flux. We thus see that even a small asymmetry can create a substantial heat flux (which is non-conductive in nature) that must be corrected for when inferring $\chi_{r,j}$.

On the other hand, the right panel in Figure 7.5 shows the same comparison for the same shot in L-mode. We note that the viscous heat flux is at least an order of magnitude lower in L-mode and thus produces an almost imperceptible difference in the conductive heat transport. It is noteworthy that, as shown in Figure 7.6, that the H-mode timeslice

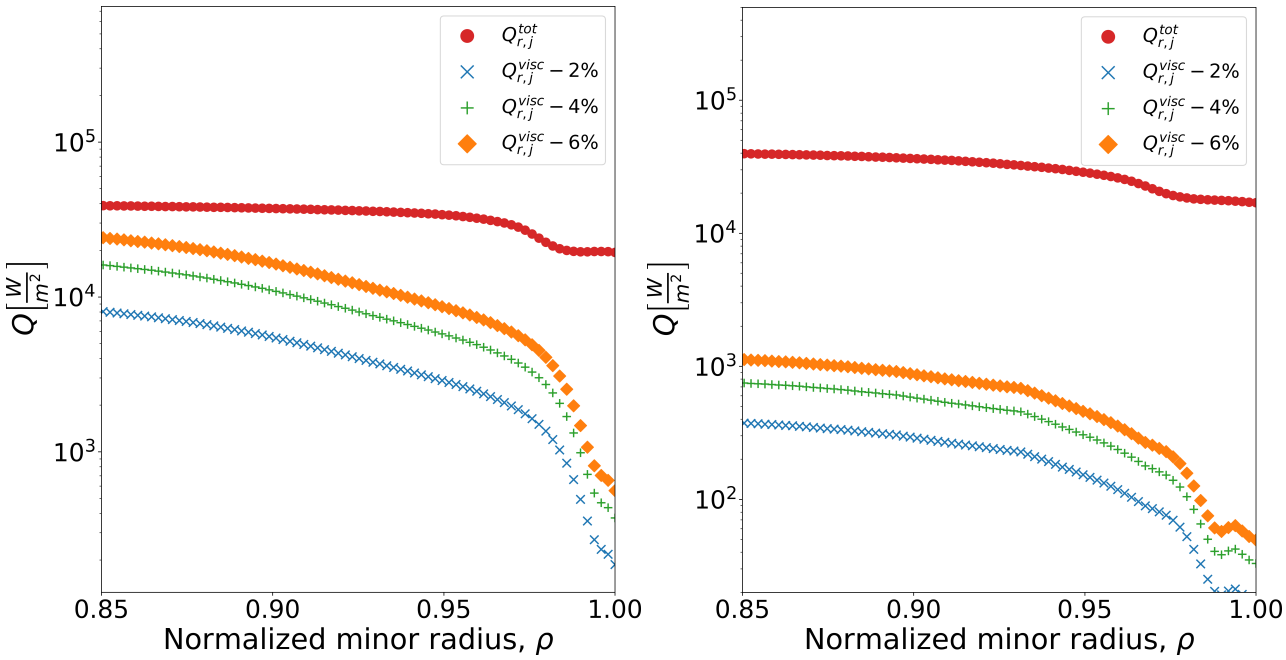

Figure 7.5: Left: Total and viscous heat fluxes for shot 144977 at 3000 ms (H-mode). The viscous heat fluxes are given for 3 asymmetry values of 2%, 4% and 6%. Right: Total and viscous heat fluxes for shot 144977 at 925 ms (L-mode). The viscous heat fluxes are given for 3 asymmetry values of 2%, 4%, and 6%.

has substantially higher rotation velocities than the L-mode timeslice, driving the viscous heating.

7.3 Pinch-diffusion Interpretation

In this section, we will present a sampling of results of this interpretation methodology for calculating the ion pinch velocity, v_{pinch}, and the radial ion diffusion coefficient, D_j. From chapter 5, the pinch velocity is given from momentum balance by

$$n_j v_{p,j} = -\frac{M_{\phi j}}{e_j B_\theta} - \frac{n_j E_\phi^A}{B_\theta} + \frac{n_j m_j \nu_{d,j}}{e_j B_\theta}\left(\frac{E_r}{B_\theta}\right) + \frac{n_j m_j f_p^{-1}}{e_j B_\theta}((\nu_{jk} + \nu_{d,j})v_{\theta,j} - \nu_{jk} v_{\theta,k} \qquad (7.8)$$

In this formulation, we have to calculate a composite momentum exchange frequency,

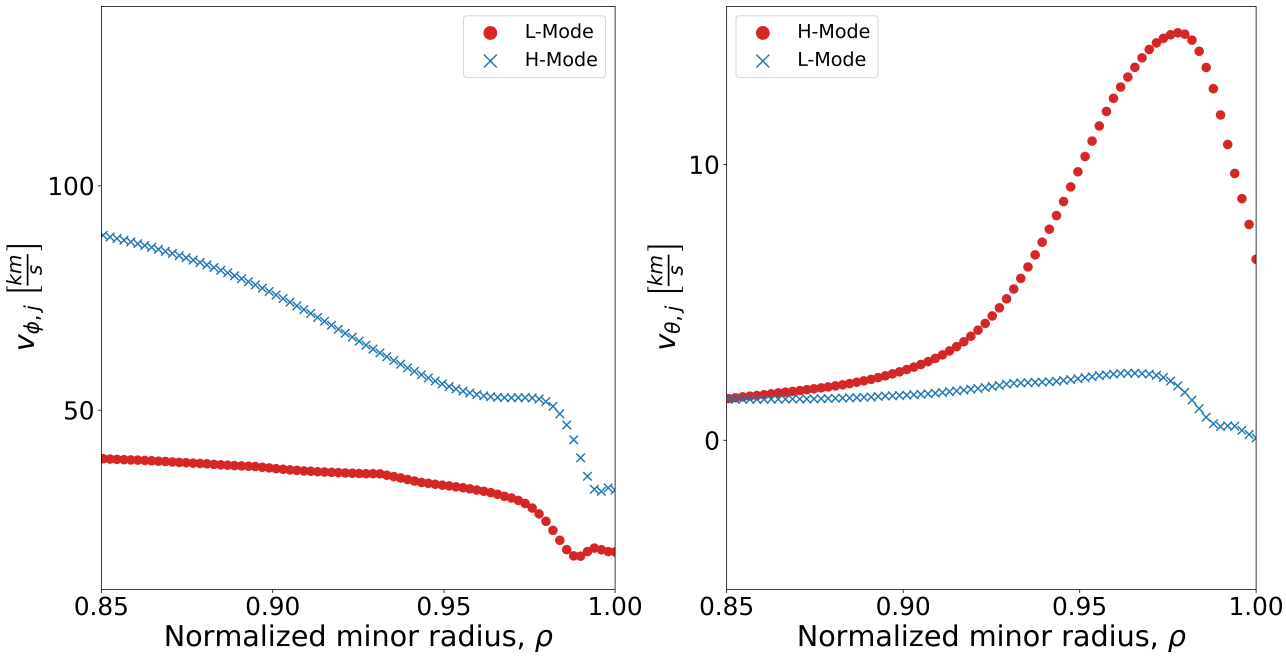

Figure 7.6: Ion toroidal velocity (left) and poloidal velocity (right) for shot 144977 for L-mode and H-mode timeslices.

$\nu_{d,j}$, using Equation 6.14. $\nu_{d,j}$ is calculated for shot 144977 at 3000 ms and presented in Figure 7.7(a). Using this, we calculate the pinch velocity for shot 144977 at 3000 ms and present the results in Figure 7.7(b). In Figure 7.7(c), the radial ion particle diffusion coefficient for this timeslice is plotted. Recalling that we posited that the total particle flux for the thermalized ions is given by a combination of diffusive transport plus a pinch velocity, i.e., Equation 5.13, these results are important because we see that the pinch velocity is a non-trivial form of non-diffusive transport.

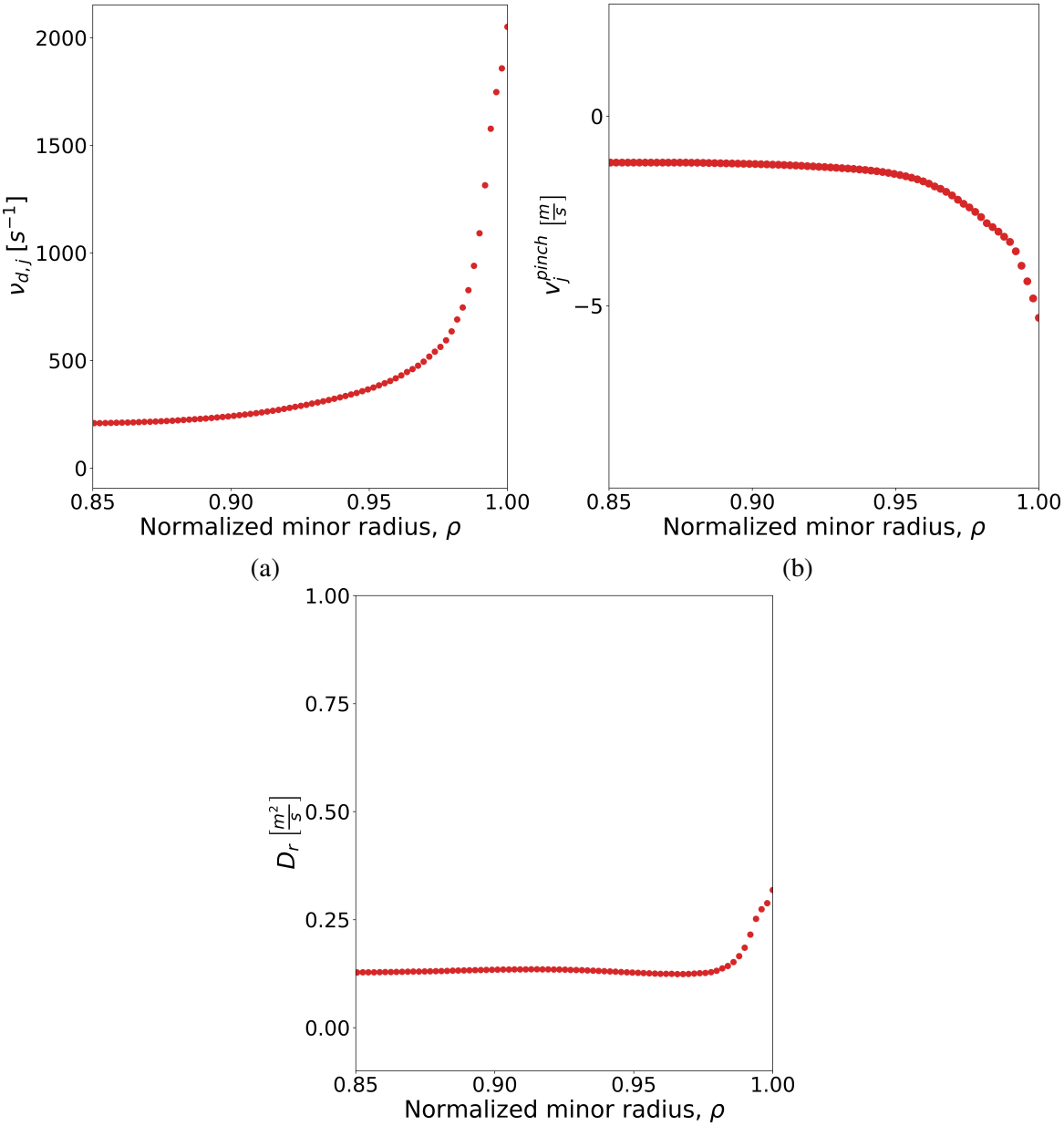

Figure 7.7: $\nu_{d,j}$, v^{pinch}, and $D_{r,j}$ for shot 144977 in H-mode.

CHAPTER 8

APPLICATION TO DIII-D DATA

8.1 DIII-D

This research utilizes data from the DIII-D tokamak located at the General Atomics facility in San Diego, California [81]. Some of the DIII-D tokamak specifications are provided in the following table.

Table 8.1: DIII-D Tokamak Specifications

Specification	Symbol	Value
Major radius	R	1.7 m
Central ion density	n_0	$0.3 - 1.5 \times 10^{20} m^{-3}$
Plasma current	I_p	0.4 - 2 MA
Safety factor (95% surface)	q_{95}	$\sim$2-12
NBI Heating Power	P_{nbi}	Up to 20 MW
Electron cyclotron heating	P_{ech}	Up to 3 MW
Toroidal magnetic field	B_ϕ	Up to 2.17 T (geom. axis)
Ion/Electron temperatures	T_i/T_e	Up to 15 keV

In this chapter, we will explore various shot regimes and see what effect the corrections discussed in previous chapters have on inferences of experimental quantities such as the radial particle flux, radial heat flux, and $\chi_{r,j}$, as well as results for the pinch velocity v_{pinch}, $\nu_{d,j}$, and D_r. The specifications (e.g., plasma radius a, plasma current I_p, central ion density $n_{j,0}$, etc.) for the shots analyzed in this chapter are given in Table A.1. Note that the main goal here is to demonstrate that the non-diffusive and non-conductive transport phenomena

discussed in previous chapters are important and should be considered when interpreting radial transport coefficients. We will present the results for samples of shots in the various regimes. For each comparison, as in the previous chapter, we will show the various heat fluxes calculated in GTEDGE2. The legend for the heat flux comparisons indicates the following.

- Q^{tot} : Q^{tot} when IOL effects are ignored.
- $\hat{Q}^{\text{tot}}$: Q^{tot} corrected for IOL.
- Q^{visc} : The viscous heat flux calculated assuming a 2% asymmetry unless otherwise noted.
- Q^{heatin} : The heat flux from the transport of rotational energy.
- Q^{conv} : The convective heat flux corrected for IOL.
- Q^{Π}: The work done by the flowing plasma on the pressure tensor.

The legend for the comparisons of $\chi_{r,j}$ has the same meaning as in the previous chapter.

We will also present the inferred drag coefficient ($\nu_{d,j}$), $D_{r,j}$, and v_{pinch} for these shots using the formalism described in previous chapters with IOL corrections applied.

8.2 Matched RMP

For the first set of shots, we look at DIII-D shot 123301 and shot 123302, which are low-collisionality, matched RMP shots (that is, shot 123301 utilizes RMP, while shot 123302 is run identically but without RMP). These perturbations in the magnetic field lines are applied via so-called "I-coils" in order to increase the chaotic nature of magnetic field lines in the edge plasma, enhancing radial electron heat transport. This is done to reduce the plasma pressure gradient below the threshold whereby edge localized modes (ELMs) can occur (see references within Ref. [71] for additional details on ELMs). The specifications for the data for shots 123301 and 123302 are given in Table A.1 for the timeslices analyzed. Shot 123301 is the RMP shot, and shot 123302 is the reference H-mode shot without I-coils.

Figure 8.1 and Figure 8.2 show the ion heat fluxes and $\chi_{r,j}$ for the RMP and non-RMP H-mode shots, respectively. Of interest is the magnitude of the corrections that we make to the total ion heat flux. At the far edge, we see the difference between the total heat flux calculated without (red dots) and with (blue crosses) the IOL correction. As expected, approximately half of the energy is being lost in a non-conductive manner at the separatrix. We also notice that the convective heat flux and work done on the pressure tensor represent substantial heat fluxes, as does the viscous heating, even when only assuming a small asymmetry. We also see that both shots have fairly similar non-conductive heat

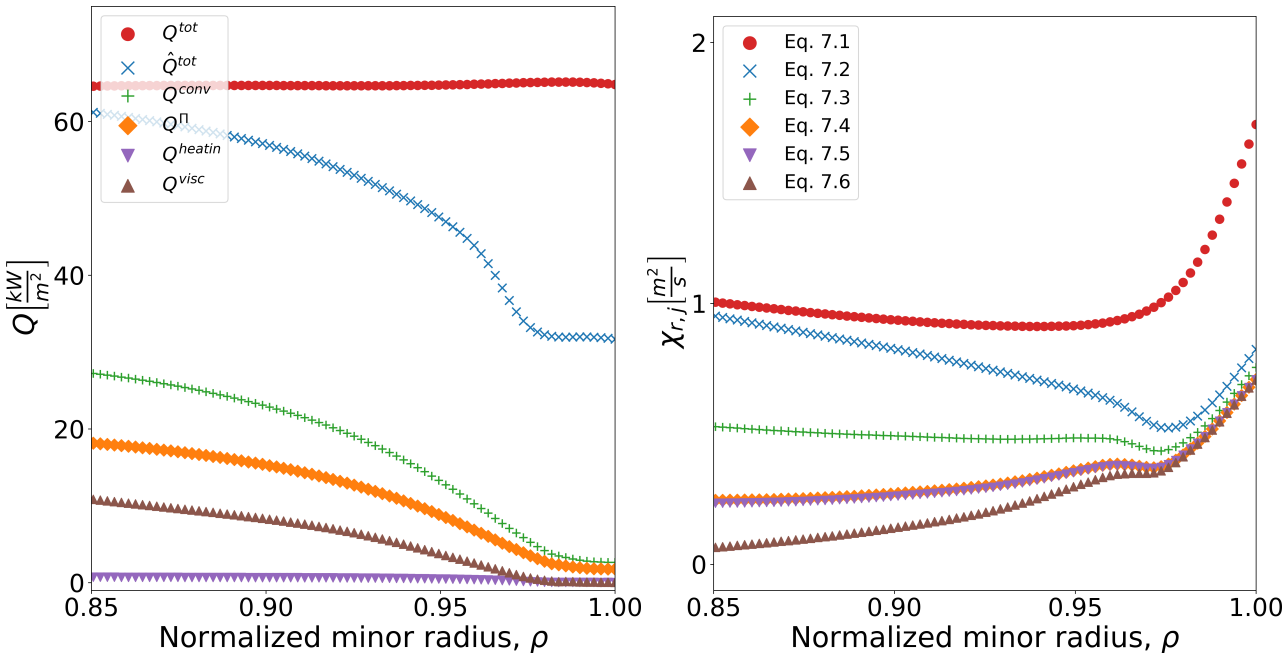

Figure 8.1: Left: Radial heat fluxes for RMP H-mode shot 123301 at 2810 ms. A 2% toroidal and poloidal velocity asymmetry is assumed. Right: Inferred $\chi_{r,j}$ when we successively correct for each non-conductive heat transport mechanism.

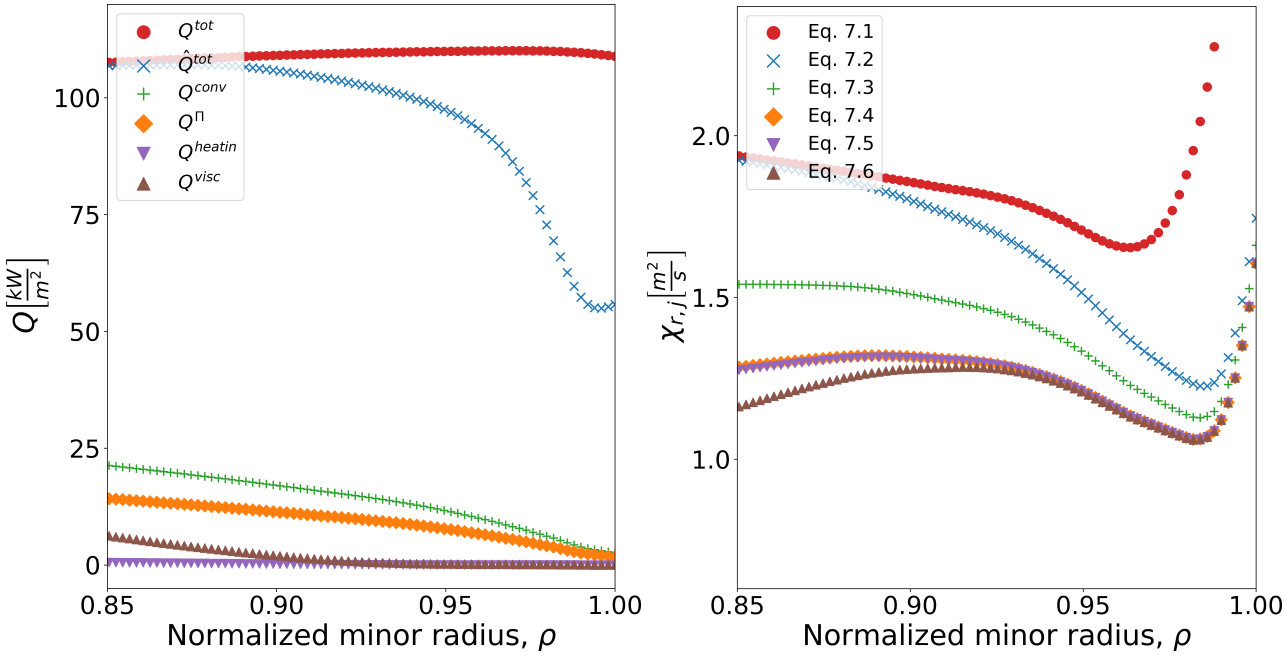

Figure 8.2: Left: Radial heat fluxes for the reference H-mode shot 123302 at 2800 ms. A 2% toroidal and poloidal velocity asymmetry is assumed. Right: Inferred $\chi_{r,j}$ when we successively correct for each non-conductive heat transport mechanism.

fluxes; however, the total heat flux of the RMP shot is greatly reduced. It is of interest that it appears that the I-coil activation does not have a significant effect on the non-conductive heat fluxes even when a much higher total heat flux is inferred. Also of note in both shots is that the viscous heating term can greatly alter the inferred $\chi_{r,j}$ and therefore should be considered when performing these types of interpretations.

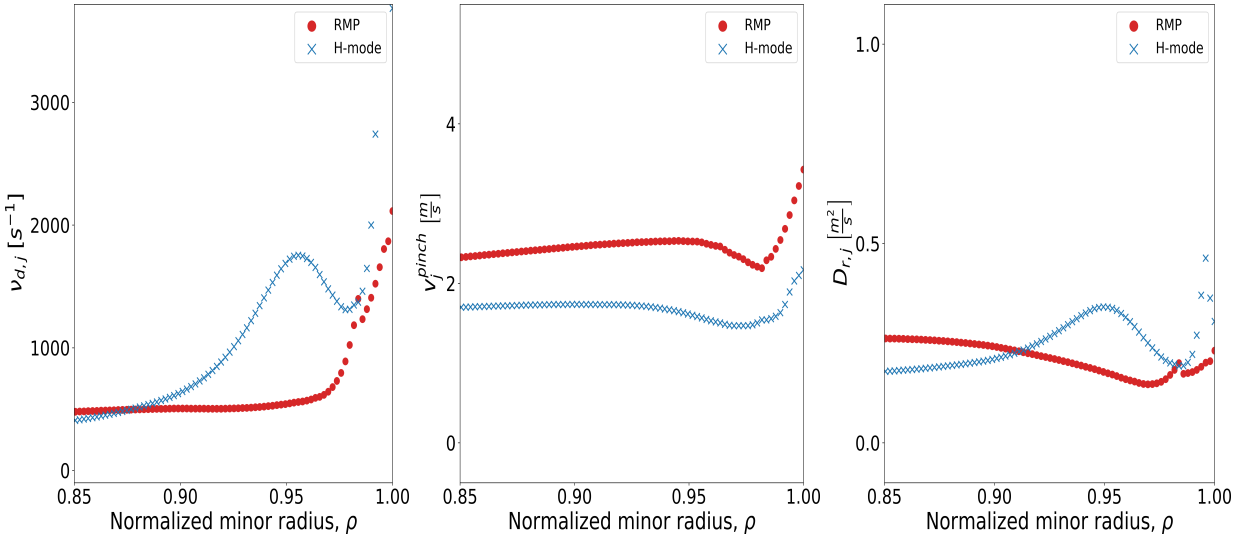

(a) (b) (c)

Figure 8.3: From left to right, comparisons of the ion pinch velocity, composite momentum transfer frequency, and effective diffusion coefficient for the RMP and reference H-mode shots 123301 and 123302 in the edge plasma at approximately 2800 ms.

Next, we present the results for the inferred particle diffusion coefficient and the pinch velocity. Figure 8.3 presents a comparison of the composite drag frequency, $\nu_{d,j}$; pinch velocity, v_j^{pinch}; and effective radial ion diffusion coefficient, $D_{r,j}$, between the two shots at approximately 2800 ms. Interestingly, we see a higher outward pinch velocity but similar diffusion coefficient in the edge plasma for the RMP shot, i.e., shot 123302, compared to its reference comparison shot 123302. This may have implications for the role RMP has

in these types of shots in so far as helping to explain the reduction in ELMs seen in RMP shots, but that is beyond the scope of this work. We also note the significant increase in the reference shot's drag frequency, $\nu_{d,j}$, in Figure 8.3(a) corresponding to a decrease in the toroidal ion rotation velocity (see Appendix A), whereas RMP shot 123301 maintains a fairly flat toroidal ion rotation velocity up until $\rho \approx 0.98$. This drives an increase in the diffusive particle transport in the reference shot seen in Figure 8.3(c).

8.3 L-mode vs. H-mode

Shot 144977 is a DIII-D H-mode discharge characterized by Type-I ELMs. This shot has been studied previously in [82]. Table A.1 provides the specifications for this shot during L-mode at 925 ms and during H-mode at 3000 ms. This H-mode timeslice consists of data collected between ELMs centered about 3000 ms. The L-mode timeslice was obtained during the initial power step while in steady state significantly before the L-to-H transition.

Figure 8.4 presents the radial ion heat fluxes and interpreted $\chi_{r,j}$ in L-mode for shot 144977. It is interesting to note that almost all of the heat is conducting out except for at the very edge, where IOL plays a more significant role. The right panel of Figure 8.4 shows that the corrections other than the IOL corrections make only minor differences in the inferred $\chi_{r,j}$. As expected, we also note the clear lack of transport barrier in this L-mode shot. Figure 8.5 presents the radial ion heat fluxes and interpreted $\chi_{r,j}$ in H-mode for the same shot. A more significant amount of heat is being transported out in a non-conductive manner, yet the total heat flux appears to be fairly similar. Of additional interest is the substantially increased H-mode viscous heating relative to L-mode. The H-mode timeslice has a higher rotational velocity in the edge compared to the L-mode timeslice; thus, this is to be expected.

We note that the convective and viscous heating, as well as the work done on the

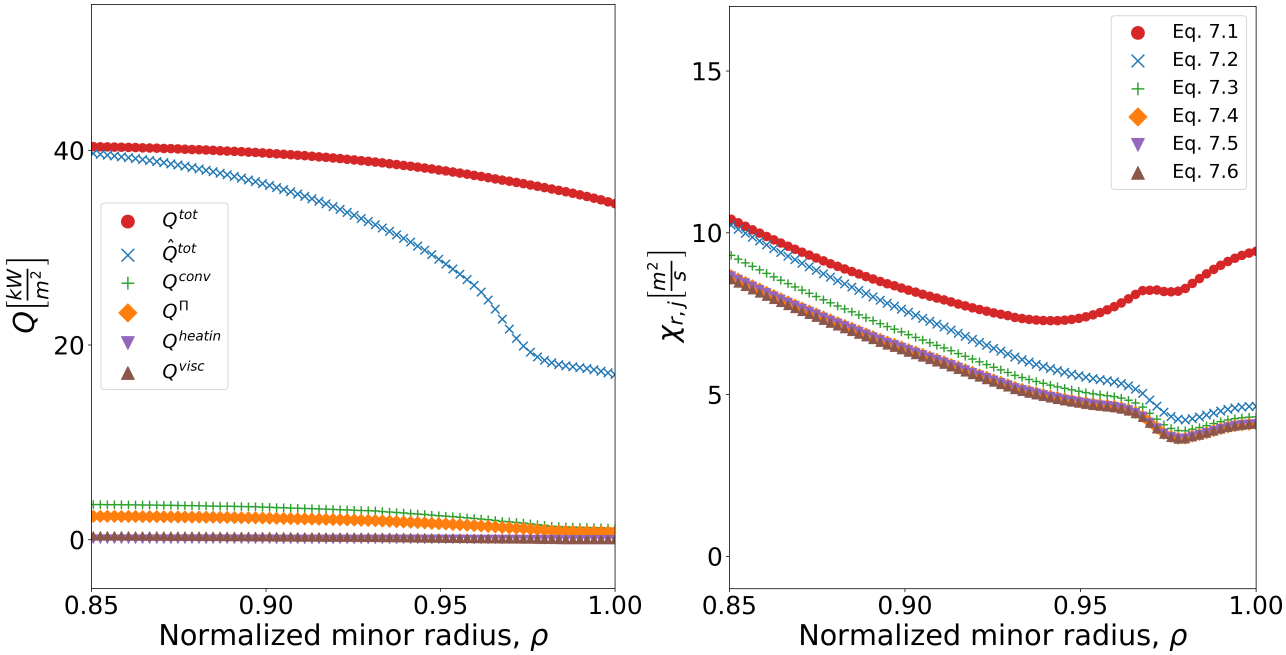

Figure 8.4: Left: Radial heat fluxes for shot 144977 in L-mode. Right: Inferred $\chi_{r,j}$ for shot 144977 in L-mode.

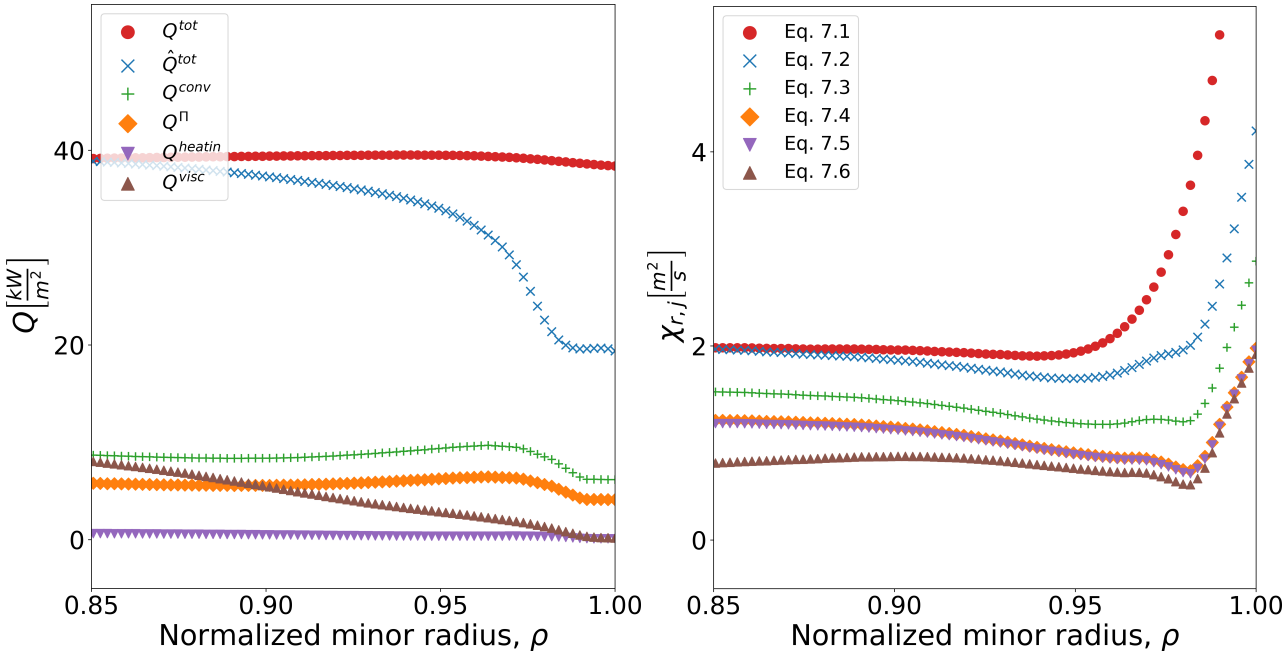

Figure 8.5: Left: Radial heat fluxes for shot 144977 in H-mode. Right: Inferred $\chi_{r,j}$ for shot 144977 in H-mode.

pressure tensor, are significant heat fluxes to be corrected for, at least in this H-mode timeslice. Figure 8.6 presents a comparison of the two timeslices in terms of the interpreted pinch velocity, $v_{j,\text{pinch}}$, and the radial ion diffusion coefficient, $D_{r,j}$. We note that the pinch velocity and diffusion coefficient are significantly reduced in the H-mode shot, as expected.

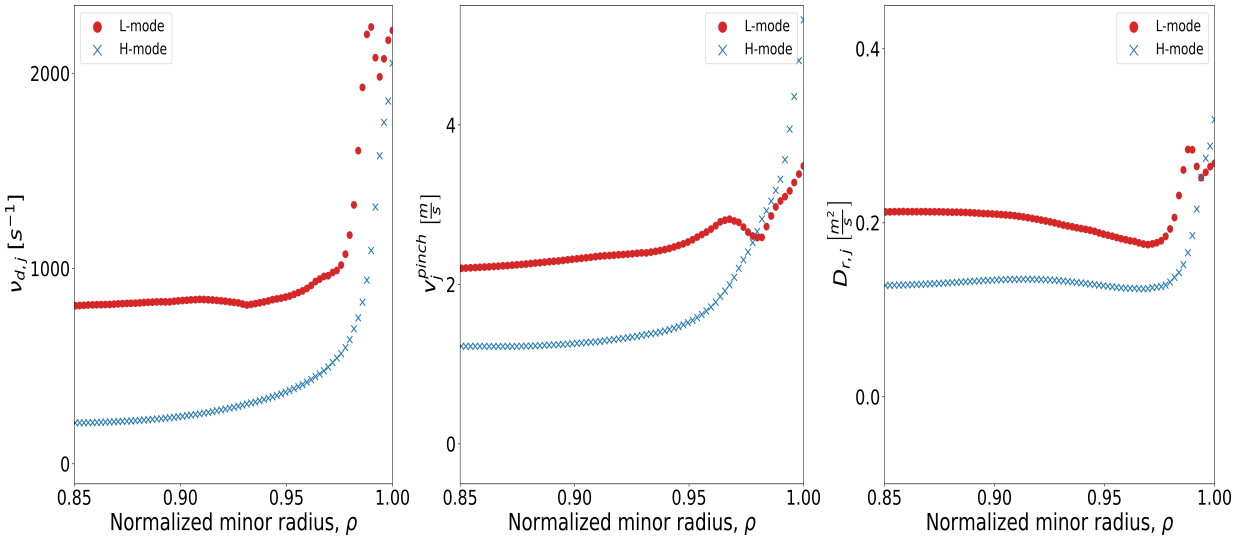

(a) (b) (c)

Figure 8.6: From left to right, comparisons of the ion pinch velocity, composite momentum transfer frequency, and effective diffusion coefficient for shot 144977 in L-mode and H-mode in the edge plasma.

8.4 QH-Mode

In this section, we will investigate the effects of our corrections on a few QH-mode shot timeslices. The specifications of shot 163477 at 1800 ms, around which the data are centered, are given in Table A.1. Shot 163477 is a highly shaped ($\delta^{\text{avg}} = 0.5$) plasma with counter-current neutral beam injection. This shaping and injection direction unlocks an operating regime characterized by H-mode-like confinement and edge pedestal but a lack

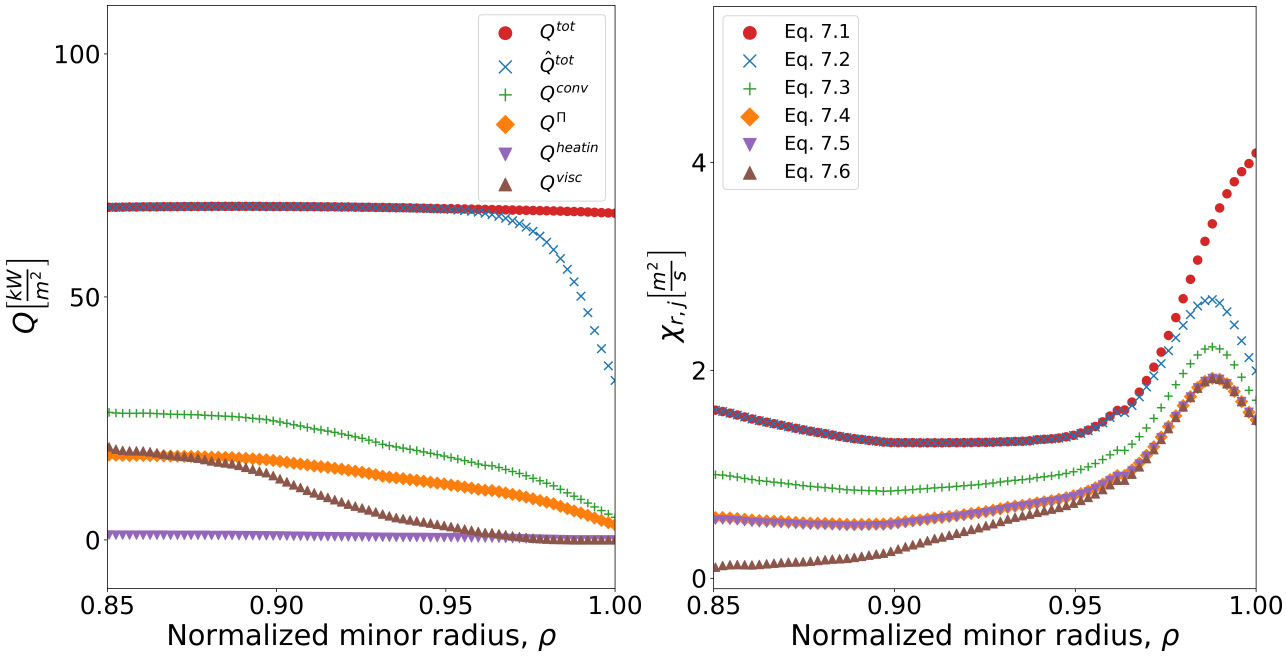

Figure 8.7: Left: Radial heat fluxes for shot 163477, a QH-mode shot, at 1800 ms. Right: Inferred $\chi_{r,j}$ for shot 163477 at 1800 ms.

of ELMs, making it a potential important operating regime for future reactors.

Figure 8.7 shows the radial ion heat fluxes and $\chi_{r,j}$ calculated for shot 163477. We note that correcting for the convective heat flux and and work done by the plasma on the pressure tensor substantially decrease $\chi_{r,j}$, and the viscous heating further reduces this value closer to the core, although it becomes negligible in the pedestal.

Figure 8.8 presents the radial ion heat fluxes and $\chi_{r,j}$ for shot 163518, a wide-pedestal QH-mode shot, at 2350 ms. One of the very interesting aspects of this shot is that the IOL occurs further into the core than in other shots analyzed. This shot is of very low collisionality in the edge; therefore, the implication from these results that a substantial amount of transport further toward the core (relative to most of the other shots, where we see IOL only beginning at $\rho > 0.9 \sim 0.95$) is occurring in a non-diffusive manner is quite

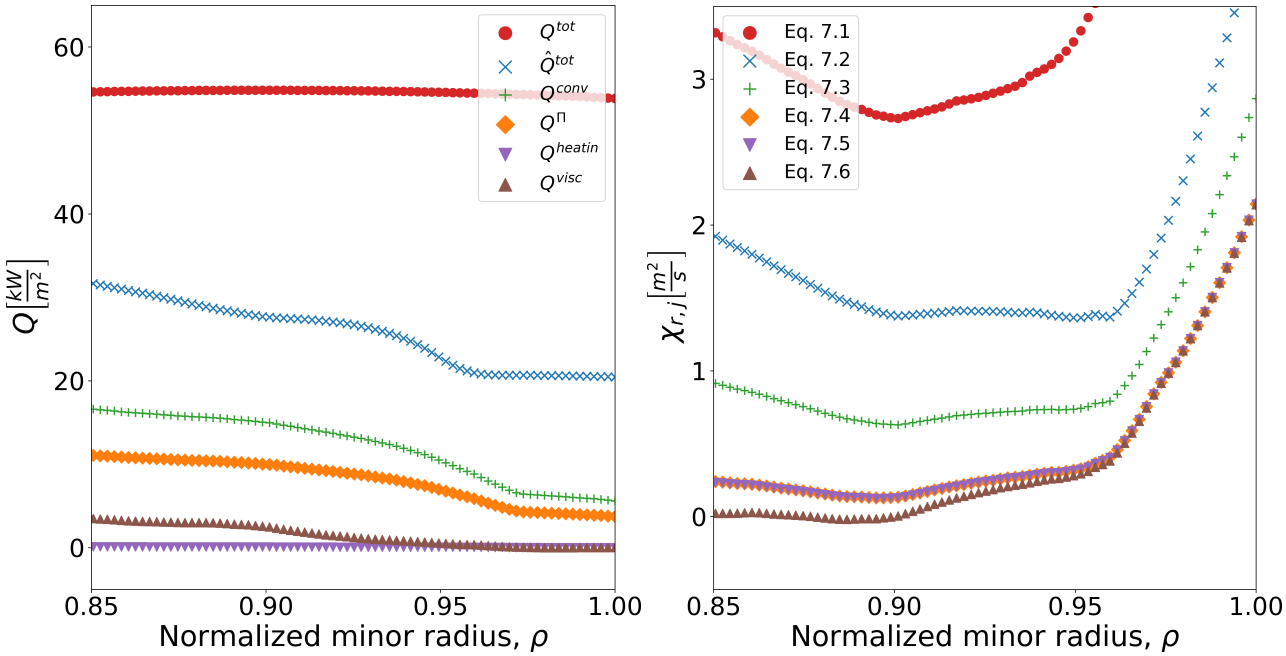

Figure 8.8: Left: Radial heat fluxes for shot 163518, a wide-pedestal QH-mode shot, at 2350 ms. Right: Inferred $\chi_{r,j}$ for shot 163518 at 2350 ms.

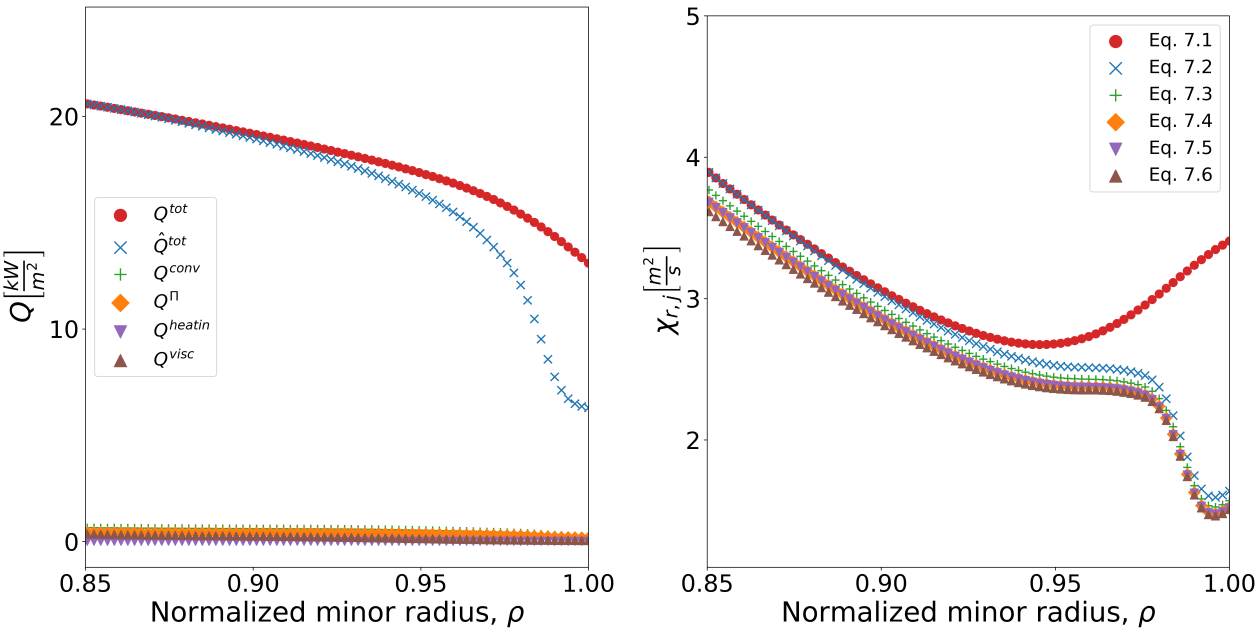

Figure 8.9: Left: Radial heat fluxes for shot 164336, a QH-mode shot, at 3740 ms. Right: Inferred $\chi_{r,j}$ for shot 164436 at 3740 ms.

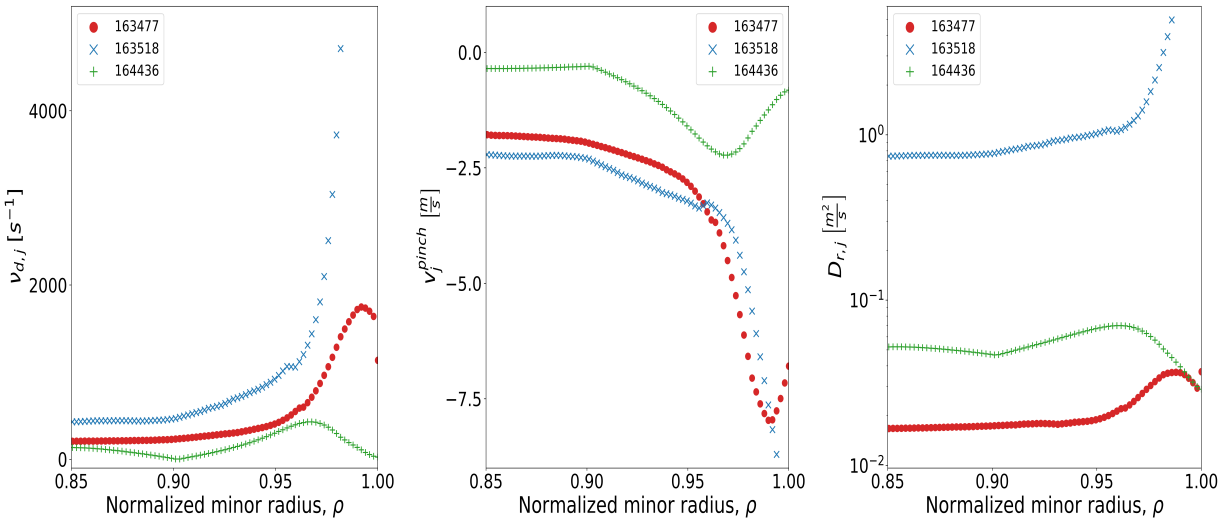

(a) (b) (c)

Figure 8.10: From left to right, comparisons of the ion pinch velocity, composite momentum transfer frequency, and effective diffusion coefficient for shots 163477, 163518, and 164436 in the edge plasma.

important. More specifically, ions are very likely to transport from closer to the core out of the plasma without experiencing a collision to put them on a different flux surface and thus a different orbit. This shot also demonstrates another example of viscous heating not necessarily being an important factor, as Q^{visc} is at least an order of magnitude lower than the convective and total heat fluxes.

Figure 8.9 presents the radial ion heat fluxes and $\chi_{r,j}$ for shot 164436, another QH-mode shot, at 3740 ms. In contrast to the other two shots analyzed in QH mode (and other shots analyzed previously), there is an essentially trivial amount of heat that is being transported out in a non-conductive (save for IOL) manner. As an example, at $\rho \approx 0.85$, only approximately $500\ W/m^2$ is being convected out, whereas the total radial ion heat flux at that flux surface is approximately $21\ kW/m^2$. We also note that IOL does not

become relatively important until the very edge, accounting for only approximately 25% of the radial ion heat flux at $\rho \approx 0.98$. However, we still see approximately half of the heat loss being from IOL at the separatrix.

Figure 8.10 presents the inferred $\nu_{d,j}$, v^{pinch}, and $D_{r,j}$ for the three QH-mode shots analyzed. Note that these results are being plotted in the same figures to save space. In the very far edge of shots 163477 and 163418, the rotational velocities decrease substantially, resulting in high amounts of drag and thus increased transport via the pinch velocity, being much higher than what we noticed in shots analyzed earlier in this chapter. In contrast, shot 164436's ion toroidal velocity does not decrease much, and the poloidal velocity is even increasing at the far edge (see Appendix A). This results in a smaller pinch velocity ($v^{pinch} \approx -2.25 m/s$ at $\rho \approx 0.97$) and modest D_r of $0.065 \frac{m^2}{s}$ at $\rho \approx 0.95$, compared $D_r \approx 1 \frac{m^2}{s}$ at $\rho \approx 0.95$ in the wide-pedestal shot (163518).

8.5 SH-Mode

Finally, we investigate an SH-mode shot. Figure 8.11 presents the results for the heat fluxes and $\chi_{r,j}$ for SH-mode shot 174783. We again note substantial IOL seemingly occurring further inward from the edge, but shot 174783 is relatively collisional, and IOL is likely overestimated in this analysis, i.e., in reality, significantly less energy is being transported out via IOL than these calculations may support. This is likely why we observe the potential for a nearly negative $\chi_{r,j}$ being inferred in this analysis. Figure 8.12 presents

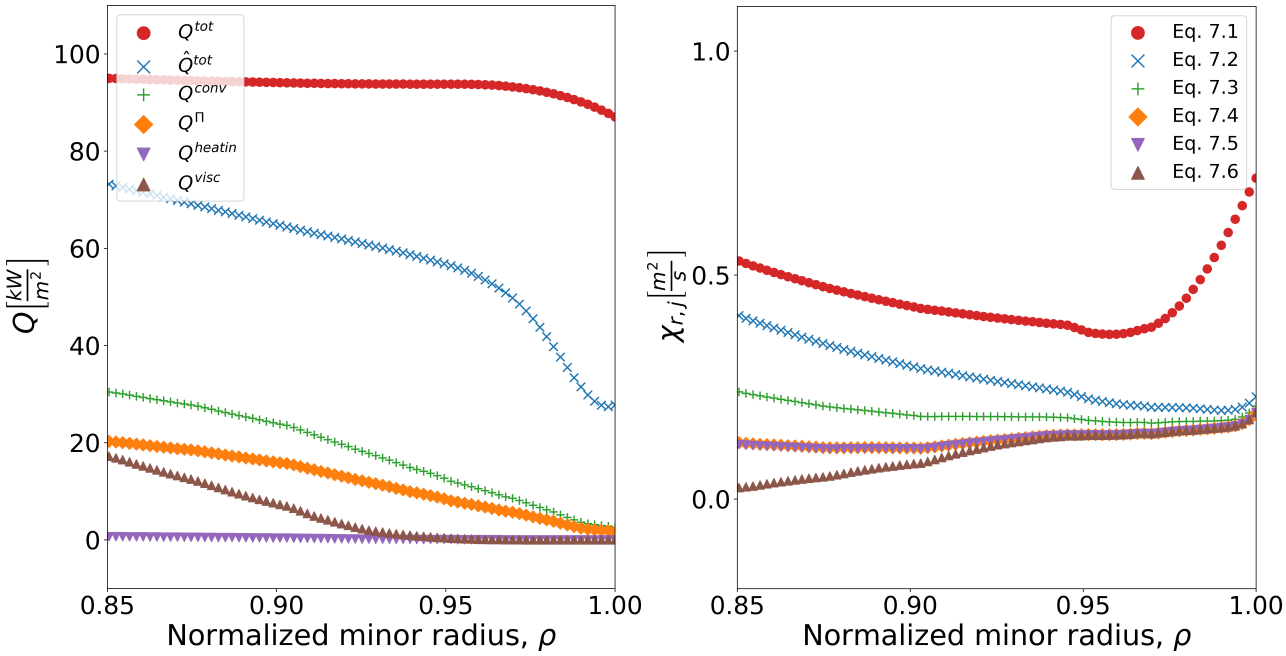

Figure 8.11: Left: Radial heat fluxes for shot 174783, an SH-mode shot, at 2100 ms. Right: Inferred $\chi_{r,j}$ for shot 174783 at 2100 ms.

the results for $\nu_{d,j}$, the pinch velocity and the diffusion coefficient for this timeslice. Note that the sharp peaking of the pinch velocity, drag frequency, and diffusion coefficient coincide with a change from decreasing toroidal rotation velocity to slightly increasing velocity at the very edge of the plasma. It is also important to note that the drag frequency is seen to be much higher in this shot, likely due to the high ion density in the edge. Given the expectation that future reactors will have very high temperatures and densities, this significantly increased pinch velocity may have important implications for edge transport in such reactors.

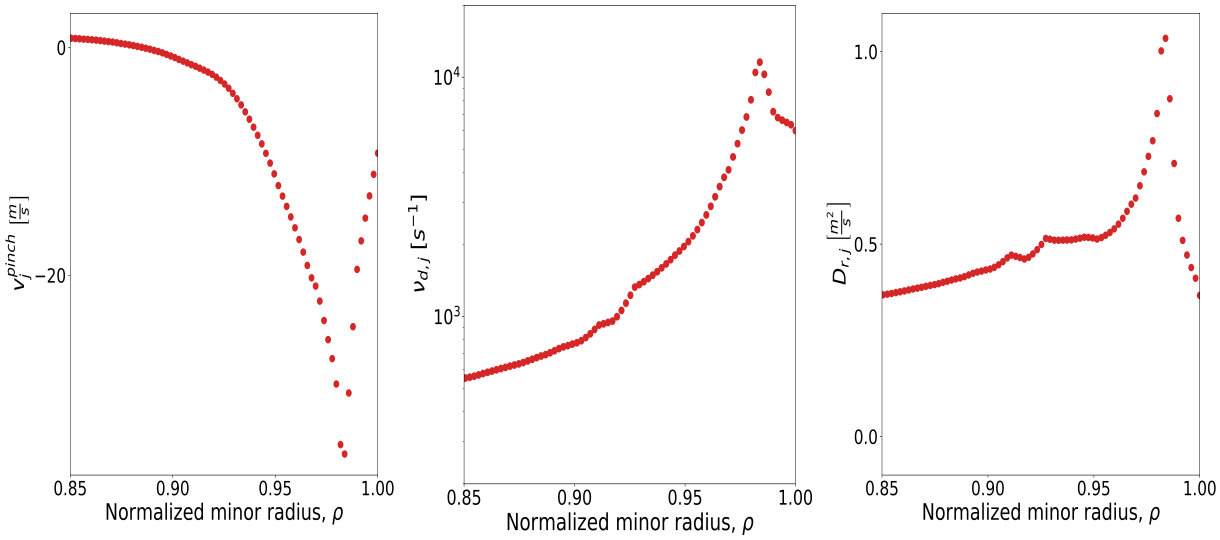

(a) (b) (c)

Figure 8.12: From left to right, comparisons of the ion pinch velocity, composite momentum transfer frequency, and effective diffusion coefficient for shot 174783 in the edge plasma.

8.6 Summary

This section presented a number of results using this improved framework for inferring radial diffusive particle and heat conductivity coefficients. Shots from various regimes (L-mode, H-Mode, RMP, QH-mode, and SH-mode) were presented, and the inferred heat conductivities were presented. It was demonstrated that correcting for the above non-conductive heat fluxes makes a significant difference in the inferred heat conductivity coefficients in the edge plasma. The most important result is that most of the above non-conductive phenomena significantly affect the interpreted $\chi_{r,i}$. In addition, it is found that viscous heating also significantly affects the results and will be an important area of future research. We want to again note briefly important limitations of this work. The IOL

calculation is an approximation based solely on conservation of energy and momentum and assumes a collisionless plasma. The calculation of the total heat flux also assumes thermal equilibrium with the impurity ions.

In the next section, an overview of theoretical models for the heat conductivity coefficient will be given. We will demonstrate, by analyzing a few of the above shots, that the interpretation methodology given above, when correcting for IOL and the various non-conductive heat fluxes, produces transport coefficients that are closer to theoretical estimates in the edge compared to the same inferred heat transport coefficients when not corrected.

CHAPTER 9

THEORETICAL COMPARISONS

The work done above is meant to demonstrate that there are multiple phenomena that must be corrected for when inferring experimental transport coefficients. We want to now demonstrate how the above inferred heat transport coefficients compare to theoretical models when we do and do not make the corrections for non-conductive phenomena. First, we will briefly review the theoretical models that are believed to most likely cause the majority of heat transport in the edge plasma.

In classical transport, magnetic field lines are assumed to be straight and uniform, and transport fluxes are assumed to be generated solely from collisions. In toroidal plasmas, additional parallel currents exist to balance perpendicular particle drifts caused by the curved magnetic fields. At higher temperatures in toroidal plasmas, i.e., less collisional plasmas, radial transport becomes dominated by "banana-plateau" transport as a result of large radial excursions following particle collisions. This transport fits under the category of "neoclassical" transport. The radial heat conduction obtained in neoclassical transport is given by the Chang-Hinton formula.

Additional transport likely exists as a result of turbulence from microinstabilities and fluctuations in the magnetic fields. One example that may be an important contributor to

anomalous ion transport in the edge is ion temperature gradient (ITG) modes. ITG modes become unstable at sufficiently large temperature gradient scale lengths. Similarly, electron temperature gradient (ETG) modes become unstable at sufficient scale lengths and can contribute to electron transport. It is generally believed, however, that ITG is suppressed in the edge pedestal.

9.1 Thermal Diffusivity

Neoclassical Ion Diffusivity

The Chang-Hington formula for neoclassical ion thermal diffusivity is given by

$$\chi_i^{neo} = \epsilon^{\frac{1}{2}} \rho_{i,\theta}^2 \nu_{i,i} [a_1 g_1 + a_2 (g_1 - g_2)] \tag{9.1}$$

where impurities, collisional and finite inverse aspect ratio effects are accounted for by the as, and the effect of the Shafranov shift is accounted for by the gs. These coefficients are given by

$$\begin{aligned} a_1 &= \frac{0.66(1+1.54\alpha) + (1.88\sqrt{\epsilon} - 1.54\epsilon)(1+3.75\alpha)}{1 + 1.03\sqrt{\mu_i^*} + 0.31\mu_i^*} \\ a_2 &= \frac{0.59\mu_i^*\epsilon}{1 + 0.74\mu_i^*\epsilon^{\frac{2}{2}}}[1 + \frac{1.33\alpha(1+0.60\alpha)}{1+1.79\alpha}] \\ g_1 &= \frac{1 + \frac{3}{2}(\epsilon^2 + \epsilon\Delta') + \frac{3}{8}\epsilon^3\Delta'}{1 + \frac{1}{2}\epsilon\Delta'} \\ g_2 &= \frac{\sqrt{1-\epsilon^2}(1 + \frac{\epsilon\Delta'}{2})}{1 + \frac{\Delta'}{\epsilon}(\sqrt{1-\epsilon^2} - 1)} \end{aligned} \tag{9.2}$$

where $\alpha = n_k Z_k^2 / n_i Z_i^2$, $\mu_i^* = \nu_{i,j} qR / \epsilon^{3/2} v_{th,i}$ and $\Delta' = d\Delta/dr$, with Δ being the

Shavranov shift. The $[a_1 g_1 + a_2(g_1 - g_2)]$ term results in enhanced radial transport.

Ion Temperature Gradient (ITG) Diffusivity

Neoclassical transport represents the minimum transport in a tokamak plasma. Many transport mechanisms accounting for anomalous transport beyond neoclassical transport have been proposed. Ion temperature gradient (ITG) modes represent a drift wave instability that is believed to be responsible for some amount of anomalous ion thermal transport in the core but is generally not viewed to be important in the pedestal except in certain situations [83]. The toroidal ITG modes become unstable for $R/L_{T_i} > (R/L_{T_i})_{\text{crit}}$ and produce thermal ion transport in the large aspect ratio, low beta limit. This condition can be approximated by

$$\left(\frac{R}{L_{T_i}}\right)_{\text{crit}} = max(0.8\frac{R}{L_{n_e}}, (1+\frac{1}{\tau})(1.33 + 1.91\frac{r}{q^2}\frac{dq}{dr})(1-1.15\epsilon)) \tag{9.3}$$

where $\tau = Z_{\text{eff}} T_e/T_i$. Two forms of the ion heat conduction coefficient are

$$\chi_i^{itg,3/2} = C_i q^2 \left(\frac{T_e}{eB}\right)\left(\frac{\rho_s}{L_{T_i}}\right)\left(\frac{R}{L_{T_i}}\right)^{3/2} \tag{9.4}$$

$$\chi_i^{itg,1/2} = C_i q \left(\frac{T_e}{eB}\right)\left(\frac{\rho_s}{L_{T_i}}\right)\left(\frac{R}{L_{T_i}}\right)^{1/2} \tag{9.5}$$

where $C_i = 0.014$ from Tore Supra experiments. These approximations were obtained using semi-quantitative knowledge of microturbulence (see discussion in [1]). Equation 9.4 assumes a characteristic time estimated as the inverse of the maximum growth rate $\gamma \approx$

$v_{th,j}(k_\perp \rho_j)/\sqrt{RL_{T_j}}$, whereas Equation 9.5 assumes one estimated as the inverse of the linear growth rate with $k_\perp \approx 1/2\rho_i$. However, it is very important to note that these estimates do not incorporate $E \times B$ shear, which suppresses turbulence in the edge.

Drift-Alfven Diffusivity

In collisional plasmas (e.g., in the edge plasma), drift-Alfven instabilities become important transport mechanisms. The ion heat conduction coefficient is given by

$$\chi_i^{da} = \chi_i^{gb} \chi_\perp / \sqrt{\mu} \tag{9.6}$$

where the "gyro-Bohm" heat conductivity is estimated as $\chi_i^{gb} = \rho_s^2 c_s / L_{p_i}$ using the gyro-Bohm scaling [84], $\mu \approx -\frac{L_{p_i}}{qR}\sqrt{\frac{m_i T_e}{m_e T_i}}$ and

$$\chi_\perp = \left[\frac{(1+\beta_n^2)^{-3} + \nu_n^2}{1 + \beta_n^2 + \nu_n^{\frac{4}{3}}}\right]^{1/2} \tag{9.7}$$

in which $\beta_n \equiv \left(\frac{m_i}{m_e}\right)^{1/2} \beta \frac{qR}{L_{p_i}}$, $\beta = \frac{2\mu_0 n_e T_e}{B^2}$, $\nu_n \equiv \left(\frac{m_i}{m_e}\right)^{1/4} \frac{(qRL_{p_i})^{1/2}}{\lambda_e}$, and $\lambda_e = v_{\text{th,e}}/\nu_{e,i}$.

9.2 Comparison of Theoretical Calculations of $\chi_{r,i}$

We want to now present a comparison of the above ion heat conductivity models calculated on data from a range of shots from DIII-D. In the following figures, the following nomenclature is utilized:

- $\chi_{r,j}$ is the ion heat conductivity without any corrections discussed in this thesis.

- $\chi_{r,j}^{\text{Corr}}$ is the ion heat conductivity with all corrections discussed in this thesis and a 2% asymmetry in the viscous heating assumed.

- $\chi_{r,j}^{\text{neo}}$ is the Chang-Hinton neoclassical ion thermal diffusivity given by Equation 9.1

- $\chi_{r,j}^{\text{gyro-Bohm}}$ is the "gyro-Bohm" ion thermal diffusivity given above.

- $\chi_{r,j}^{\text{DA}}$ is the drift-Alfven ion thermal diffusivity given by Equation 9.6

- $\chi_{r,j}^{\text{ITG-1/2}}$ and $\chi_{r,j}^{\text{ITG-3/2}}$ are the ITG ion thermal diffusivities given by Equation 9.5 and Equation 9.4, respectively

We first look at shot 144977, which includes an L-mode and H-mode phase. Figure 9.1 presents the calculated theoretical models for $\chi_{r,j}$, as well as the corrected and uncorrected inferred $\chi_{r,j}$. Note that in both time slices, the ITG modes were not unstable and did not produce transport. We note the expected significant decrease in heat transport in the edge characteristic of H-mode edges. We also note that drift-Alfven transport seems to significantly overpredict ion heat transport in this edge plasma in H-mode but appears to be of the right order of magnitude in L-mode, and neoclassical transport greatly underpredicts the inferred ion heat transport. However, it is unlikely that drift-Alfven transport is significant in this edge plasma for the H-mode timeslice due to the relatively low collisionality, as drift-Alfven instabilities are more important in collisional edge plasmas. It does not appear that good agreement between theory and experimental inference is obtained here.

Next, we look at shots 123301 and 123302, the comparison RMP shots with data around

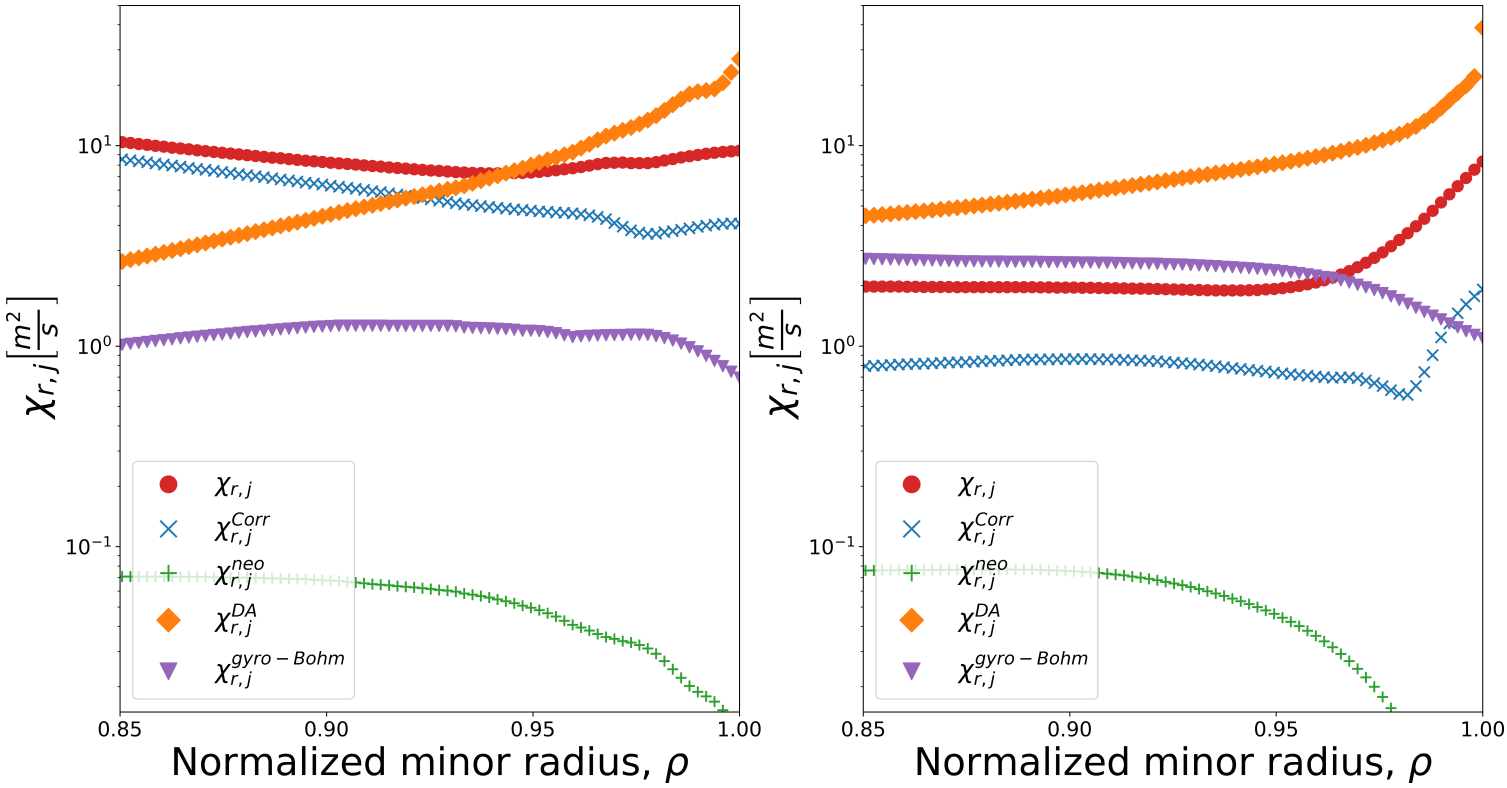

Figure 9.1: Comparison of theoretical expressions for $\chi_{r,i}$ calculated using data for shot 144977 in L-mode (left) and H-mode (right) as well as our inferred uncorrected ($\chi_{r,j}$) and corrected ($\chi_{r,j}^{\text{Corr}}$) ion heat diffusion coefficients. Note that ITG modes may be unstable and produce transport at these times in the edge according to Equation 9.3.

2800 ms. Figure 9.2 presents the calculated theoretical $\chi_{r,j}$ for the two timeslices. Note that the ITG modes are marginally unstable in both timeslices and may produce transport, although it is important to remember that $E \times B$ shear suppression is not incorporated into the formulas used, and thus, ITG modes may not actually produce transport here. We also note that neoclassical theory does not capture the increase in transport found at the very edge of the plasma very well in magnitude. However, we do see that the corrections to $\chi_{r,j}$ greatly decrease the magnitude of the inferred conductive radial heat transport and imply transport that matches the profile of neoclassical theory decently in both situations but that still remains an order of magnitude higher than transport predicted by neoclassical transport alone. In both timeslices, however, the inferred $\chi_{r,j}$ seems to diverge from neoclassical theory at the far edge. The profiles in both cases seem to approximately follow drift-Alfven transport at the far edge although at far lower magnitude. Although not shown, the H-mode timeslice becomes relatively collisional in the last few % of the plasma, possibly producing drift-Alfven transport; however, both plasmas are relatively collisionless prior to the very edge of the plasma.

Next, we look at shot 163477, one of the QH-mode shots analyzed previously. Note that the data are not plotted with a semi-log plot, as the corrected thermal conductivity coefficients are of the right order of magnitude in these QH-mode shots. Figure 9.3 presents the theoretical calculations of $\chi_{r,j}$ along with the uncorrected inferred $\chi_{r,j}$ and the corrected version, $\chi_{r,j}^{\text{Corr}}$. We note that this plasma is fairly collisionless in the edge at this timeslice,

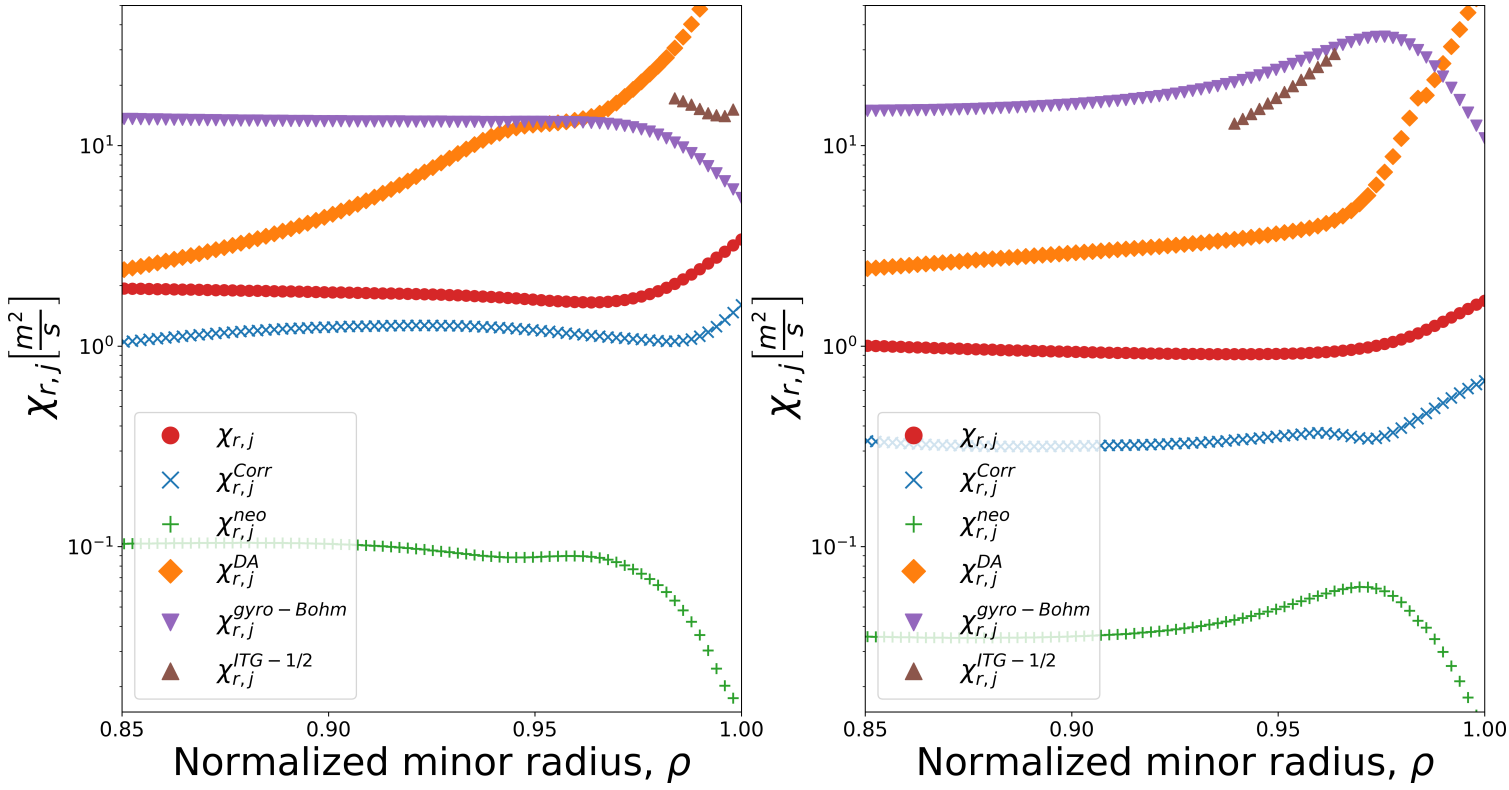

Figure 9.2: Comparison of theoretical expressions for $\chi_{r,i}$ calculated using data for the reference H-mode shot 123302 (left) and the RMP H-mode shot 123301 (right). Note that ITG modes may produce transport at these times in the far edge.

and thus, drift-Alfven transport is likely to not be a contributor to transport. ITG modes are marginally stable in this shot and therefore may produce transport, again with the caveat stated for the RMP comparison (i.e., the ITG formulations do not consider $E \times B$ sheer stabilization, which suppresses transport in the edge). When non-conductive transport mechanisms are not corrected for, we see that $\chi_{r,j}$ does not seem to have the correct magnitude of transport or a profile that is similar to any of the theoretical calculations. On the other hand, when our corrections are applied, the profile of $\chi_{r,j}^{\text{Corr}}$ is fairly similar to transport predicted to be driven by ITG modes although with a deviation in the magnitude.

Figure 9.4 presents the results for shot 164436, another QH-mode shot. We note similar trends of $\chi_{r,j}^{\text{ITG-3/2}}$ overpredicting transport, while $\chi_{r,j}^{\text{ITG-1/2}}$ may potentially be a candidate for properly estimating the heat transport in the edge here. Gyro-bohm transport also seems to be much lower than that found in shots analyzed above. We note that the decrease in transport seen at the far edge follows the drop offs in transport seen with gyro-bohm and ITG transport; however, such a drop off is not seen when non-conductive transport mechanisms are not corrected for. Figure 9.5 presents the results for shot 163518, the wide-pedestal QH-mode shot. This result is interesting, as we see decent agreement between neoclassical theory and our corrected $\chi_{r,j}$. Of course, one has to consider, here and throughout the results presented, the assumption on the viscous heating. These results may indicate that the 2% velocity asymmetry might be too strong of an assumption given that neoclassical theory represents the minimum transport that should be possible.

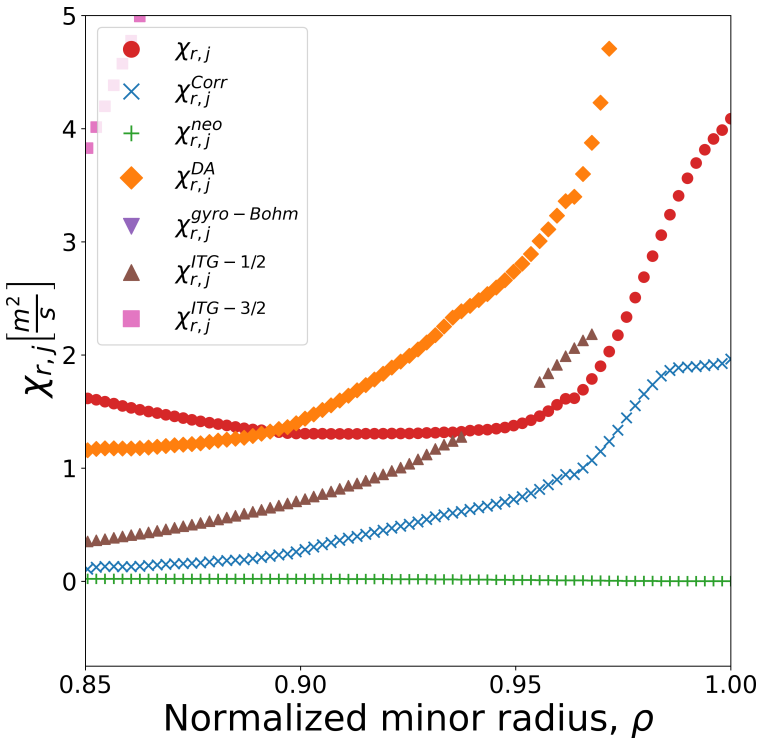

Figure 9.3: Theoretical expressions for QH-mode shot 163477 as well as the inferred corrected and uncorrected radial ion heat conductivity.

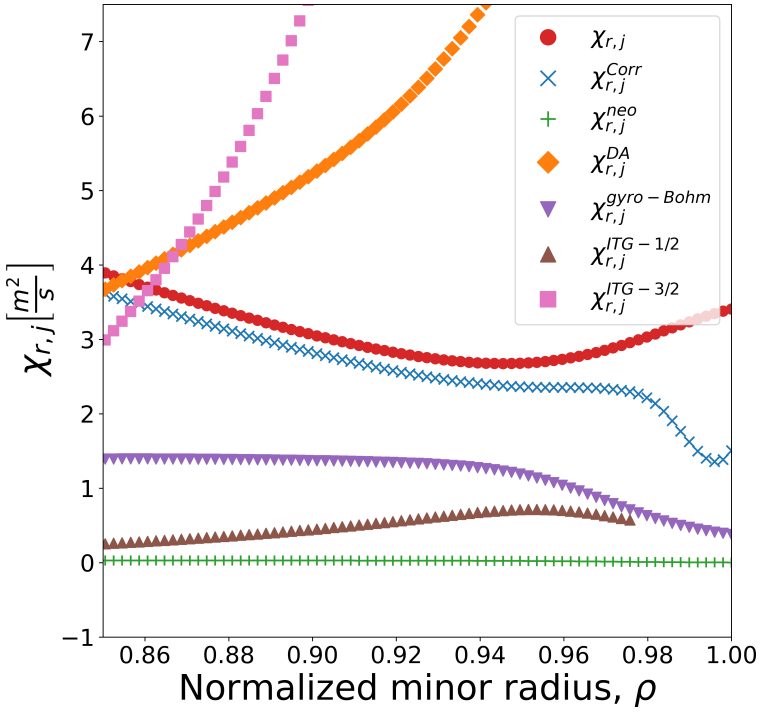

Figure 9.4: Theoretical expressions for QH-mode shot 164436 as well as the inferred corrected and uncorrected radial ion heat conductivity.

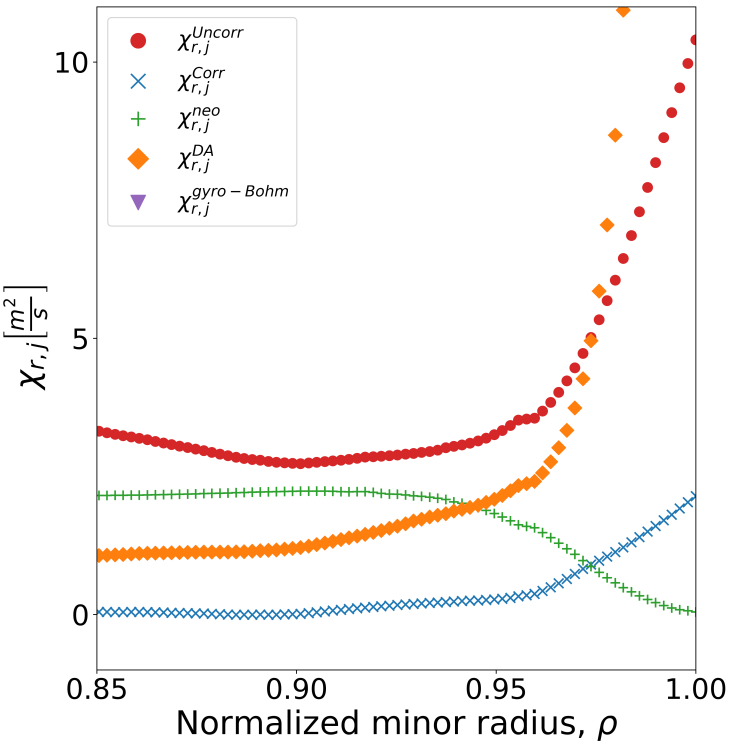

Figure 9.5: Theoretical expressions for the wide-pedestal QH-mode shot 163518 as well as the inferred corrected and uncorrected radial ion heat conductivity.

Finally, we observe the results for shot 174783, the SH-mode shot analyzed above. Figure 9.6 presents the results for the calculated theoretical $\chi_{r,j}$ and the inferred corrected and uncorrected $\chi_{r,j}$. It is interesting to note that all of the theoretical estimates, even neoclassical theory, seem to overestimate our inferred estimates of $\chi_{r,j}$, potentially indicating some missing physics in our model and/or an overestimate of the non-conductive heat flows (the latter being likely, as discussed in the previous chapter). Future work should look at exactly why theoretical estimates used in this work indicate such large heat transport.

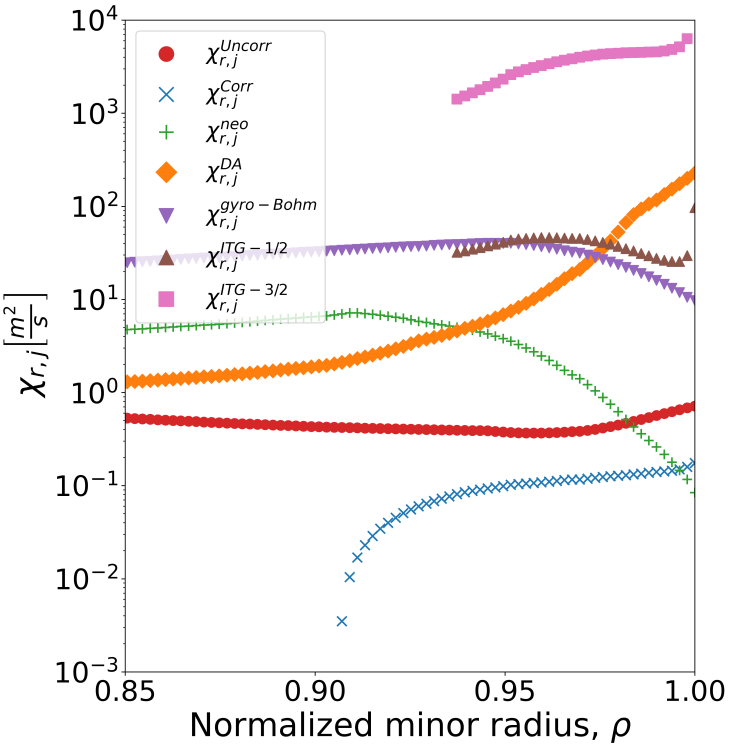

Figure 9.6: Theoretical expressions for SH-mode shot 174783 as well as the inferred corrected and uncorrected radial ion heat conductivity.

9.3 Summary

This section presented one of the main results of this dissertation. We presented the results for the corrected and uncorrected inferred ion thermal diffusion coefficients alongside theoretical calculations of various models of ion heat conductivity. It was found that correcting for non-conductive mechanisms such as IOL, viscous heating, inertial heating, and convective heating result in inferred transport coefficients that often better match theoretical calculations, although a good agreement in terms of magnitude is difficult to obtain. In general, it is seen that drift-Alfven transport is too high in almost all of the analyzed shots. ITG transport in general seems to significantly overpredict our inferred $\chi_{r,j}$ when

our corrections are considered, except in shot 164436, although we again note that our formulations do not incorporate $E \times B$ sheer suppression of turbulence. Neoclassical transport is generally seen to underestimate the inferred transport. Gyro-Bohm transport in general overpredicts transport in these shots, with the possible exception of shot 164436.

CHAPTER 10

CONCLUDING REMARKS

10.1 Conclusions

This thesis attempted to demonstrate that non-diffusive and non-conductive transport phenomena are important and should be considered when inferring transport coefficients in the edge plasma. Chapter 1 briefly introduced the field of nuclear fusion and discussed fusion reactors. That chapter discussed the basics of plasmas in tokamak reactors and briefly touched on the challenges facing future reactor operations. Chapter 2 presented the objectives of this thesis. That chapter discussed how the improved methodology developed in this research would be used to more accurately infer transport coefficients in the edge plasma. The background on how the GTEDGE2 code was used to obtain the results in this thesis was provided, including the basic equations governing the overarching process. Chapter 3 provided the literature review. It was shown that some work has been performed using interpretive codes such as GTEDGE to infer transport coefficients and compare with theoretical calculations; however, it was made clear that the work herein is somewhat unique in the field. No extensive bodies of work appear to exist showing the non-diffusive and non-conductive transport phenomena discussed herein applied to currently used codes and frameworks interpreting plasma properties.

Chapter 4 presented the Ion Orbit Loss framework used within this research. Ion orbit loss is an important non-diffusive particle transport mechanism that carries important implications for the transport in the edge plasma. Ion orbit loss is a transport mechanism whereby ions find themselves on orbits that, due to conservation of angular momentum, result in the ions being transported across the separatrix and out of the plasma. Particle-following work done by others has shown that approximately 50% of ions will return to the plasma on banana orbits but that the remainder are indeed lost from the plasma. That chapter also included a scan of toroidal magnetic field, radial electric field, and ion temperature values to demonstrate the main drivers of IOL. The chapter applied the IOL model to multiple shot regimes to demonstrate how readily ions appeared to fall onto these loss orbits, thereby creating significant differences in how much of the heat and particle fluxes can be considered to be diffusing out of the plasma. It was demonstrated that IOL could occur significantly inward ($\rho < 0.9$) in certain plasmas but also potentially only near the very edge ($\rho > 0.98$) in certain instances. Chapter 5 presented the theoretical framework utilized to extract the non-diffusive and non-conductive components of the total radial particle and total radial heat fluxes, respectively, so that one could interpret an effective diffusion coefficient $D_{;j}$ and heat conduction coefficient $\chi_{r,j}$. We showed that one can start from particle, energy, and momentum balance and establish a pinch-diffusion equation that has a diffusive and a non-diffusive component. We also noted how an effective momentum exchange frequency could be inferred from experimental data to obtain this

effective diffusion coefficient. It was also demonstrated how the balance equations lead to multiple non-conductive heat transport mechanisms that should be considered when inferring $\chi_{r,j}$.

Chapter 6 demonstrated how the work in previous chapters is utilized in the GTEDGE2 framework. The GTEDGE methodology has been benchmarked against other codes for inferring transport from experimental data, and the GTEDGE2 code builds upon that methodology by integrating a parallelized beam deposition code for neutral beam ion deposition and GTNEUTPY for neutrals recycling. The code without neutrals calculations can be run on a consumer laptop in on the order of seconds. The GTNEUTPY code can be run in on the order of a few minutes on a consumer laptop and does not require the laborious manual meshing process required of the original GTNEUT. This code can therefore provide results on much faster timescales compared to, e.g., particle-following and gyrokinetic codes. Chapter 7 utilized this framework in the GTEDGE2 code to infer transport coefficients in select shots to demonstrate that the non-conductive and non-diffusive transport mechanisms derived from the particle, energy, and momentum balance equations are at least as, if not more, important than the conductive and diffusive transport mechanisms. Looking at shot 123302, an H-mode shot, we saw that the convective heat flux, work done on the pressure tensor, and viscous heating constitute 20%, 14% and 5% of the total radial heat flux at the start of the edge region of the plasma. That chapter also demonstrated the potential magnitude of the viscous heating when varying the assumed asymmetries.

Viscous heating results from poloidal and toroidal asymmetries in the poloidal and toroidal rotation velocities. These asymmetries are experimentally very difficult to measure and are believed to be very small; however, we demonstrated that even a small ($\tilde{2}\%$) asymmetry can have substantial effects on the inferred $\chi_{r,j}$. We also demonstrated that this viscous heating is not always important, especially in shots with low rotation in the edge plasma, something that will be important in ITER and other future reactors run with low torque.

Chapter 8 presented the results of our inference of transport coefficients on a number of shot regimes for DIII-D plasmas. First, a set of matched RMP shots were analyzed. It was shown that the shot with I-coils activated saw substantially lower total radial ion heat flow and ultimately a lower conductive heat flux. The shot with the applied RMP (123301) also presented a higher pinch velocity but similar diffusion coefficient as compared to the reference H-mode shot. It also is of interest that the non-conductive heat flows are quite similar between RMP and non-RMP operation, indicating that the field perturbations produced by the I-coils may not drive or suppress non-conductive ion heat flows. Next, the results for shot 144977 were presented, and a comparison between L-mode and H-mode was provided. It was interesting to note that the total edge ion heat flux was similar between both timeslices but that H-mode saw significantly increased non-conductive ion heat flows. We also found significantly higher diffusive and non-diffusive particle transport, as expected.

We also looked at a pair of QH-mode shots as well. Shot 163477 demonstrated how

IOL is not always significant in the edge in the sense that ions may only become lost at the very edge of the plasma. We also saw how viscous heating may contribute only a minimal amount of radial ion heat flux out of the plasma. Furthermore, given the low rotation velocities, we saw increased drag and pinch diffusion, which is an important observation given that future tokamaks will likely operate with low rotation velocities. Finally, we presented the results for shot 174783, an SH-mode shot. The particle transport in this shot was noteworthy. Due to the high densities involved in the edge of this shot, a strong inward pinch velocity was found when the toroidal ion velocity went from slightly increasing to slightly decreasing when moving radially outward. This may have important implications in future reactors that will operate at high densities and temperatures.

10.2 Recommendations

The work described in this thesis provides a number of important lessons that can be applied in future research. Through the analysis using the GTEDGE2 code, it is demonstrated that radial ion transport in DIII-D is not governed solely by diffusive and conductive transport processes. In fact, non-diffusive and non-conductive particle and energy transport, respectively, is significant. This is important because it is often assumed that, e.g., particle transport in tokamaks is basically governed solely by short-range forces and thus is basically diffusive in nature. If one uses this assumption and attempts to model or predict such transport using, e.g., turbulence-based models, and one does not correct the total particle

and heat fluxes for non-diffusive and non-conductive transport phenomena, one would be attempting to obtain agreement to particle and heat fluxes that inherently result from transport that is diffusive and non-diffusive in nature.

The importance of the fact that transport is not solely diffusive in nature is seen in our comparisons with theoretical models. As an example, Figure 9.2 shows that our corrected $\chi_{r,j}$ in shot 123301, an RMP shot, results in a 75% reduction in the inferred conductive heat transport at $\rho \approx 0.95$ when considering all the corrections discussed in this thesis. It is also clear, similar to most shots analyzed in this research, that even with all of our corrections, we do not find satisfactory agreement between our inferred $\chi_{r,j}$ and theoretical models (although some agreement may have been found at the beginning of the edge region, i.e., $\rho \approx 0.85$, for QH-mode shot 163477). However, we demonstrated that the viscous heating can be, depending on the shot, highly sensitive to the poloidal and toroidal rotation velocity asymmetries, meaning that, for example, underprediction of transport by neoclassical theory may simply be the result of the lack of knowledge of the viscous heating. This is beyond the scope of this work given that such asymmetries are difficult to measure and are also potentially very small, though.

This work also showed the importance of two phenomena worth considering in future research. Ion orbit loss can be a significant driver of non-diffusive transport, especially in the edge plasma. IOL ultimately derives simply from conservation of energy and angular momentum. Therefore, if one is modeling a collisionless plasma, one must assume that

a substantial portion of ions will find themselves on loss orbits at the edge. As shown in certain shots, this may be true even before $\rho < 0.90$. Since the edge dictates the boundary condition for overall plasma performance, such calculation is important. The IOL calculation found in GTEDGE2 can be performed in less than a second and should be replicated in other edge codes. Regarding heating, it was shown that viscous heating may also be an important transport mechanism in tokamaks. Although future reactors are expected to be slowly rotating at the edge, even small asymmetries in the rotation velocities seem to drive non-trivial radial ion heat fluxes.

The use of the GTEDGE2 code for fast analysis of edge plasma performance is also recommended. The GTEDGE2 code, coupled to GTNEUTPY, can perform analyses on timeslices in on the order of minutes. The modules within the code can also be attached to other codes, such as any code requiring a quick estimate of loss orbits obtained by the IOL module.

empty

Appendices

APPENDIX A

SUPPLEMENTARY SHOT DATA

The following appendix provides supplementary data on the shots used in this thesis. Table A.1 provides a table of various 0-D values, including time id, operating mode, and plasma radius, for the shots analyzed. The figures for each time slice include the ion (n_j) and electron (n_e) densities; ion toroidal ($v_{\phi,j}$), ion poloidal ($v_{\theta,j}$), impurity toroidal ($v_{\phi,k}$), and impurity poloidal ($v_{\theta,k}$) rotation velocities; and the ion (T_j) and electron (T_e) temperatures in the edge plasma.

Table A.1: Shot Specifications

Shot	Time	Mode	a	B_ϕ	I_p	$n_{j,0}$	$n_{e,0}$	$T_{j,0}$	$T_{e,0}$	P_{NBI}
123301	2800 ms	RMP H-mode	0.6 m	1.98 T	1.78 MA	$1.75 \times 10^{19} m^{-3}$	$4.5 \times 10^{19} m^{-3}$	11.9 keV	3.5 keV	7.6 MW
123302	2810 ms	Ref. H-mode	0.6 m	1.98 T	1.50 MA	$4.6 \times 10^{19} m^{-3}$	$4.9 \times 10^{19} m^{-3}$	8.2 keV	3.4 keV	7.6 MW
144977	925 ms	L-mode	0.6 m	2.11 T	1.0 MA	$1.97 \times 10^{19} m^{-3}$	$2.27 \times 10^{19} m^{-3}$	1.6 keV	1.6 keV	3.3 MW
144977	3000 ms	H-mode	0.53 m	2.11 T	1.12 MA	$1.79 \times 10^{19} m^{-3}$	$2.05 \times 10^{19} m^{-3}$	2.4 keV	1.8 keV	2.2 MW
163477	1800 ms	QH-mode	0.59 m	2.11T	1.08 MA	$1.4 \times 10^{19} m^{-3}$	$3.2 \times 10^{19} m^{-3}$	9.1 keV	4.5 keV	6.1 MW
163518	2350 ms	QH-mode	0.59 m	2.09 T	-1.087 MA	$2.3 \times 10^{19} m^{-3}$	$4.9 \times 10^{19} m^{-3}$	7.3 keV	4.3 keV	5.2 MW
164436	3740 ms	QH-mode	0.57 m	2.0 T	1.07 MA	$2.9 \times 10^{19} m^{-3}$	$3.1 \times 10^{19} m^{-3}$	0.5 keV	1.7 keV	1.5 MW
170672	1900 ms	Neg. Tri.	0.6 m	2.0 T	0.89 MA	$3.6 \times 10^{19} m^{-3}$	$5.2 \times 10^{19} m^{-3}$	4.2 keV	4.9 keV	5.9 MW
174783	2100 ms	SH-mode	0.6 m	2.2 T	2.0 MA	$5.9 \times 10^{19} m^{-3}$	$7.7 \times 10^{19} m^{-3}$	13 keV	5.7 keV	14 MW

Shot 123301 - 2800 ms

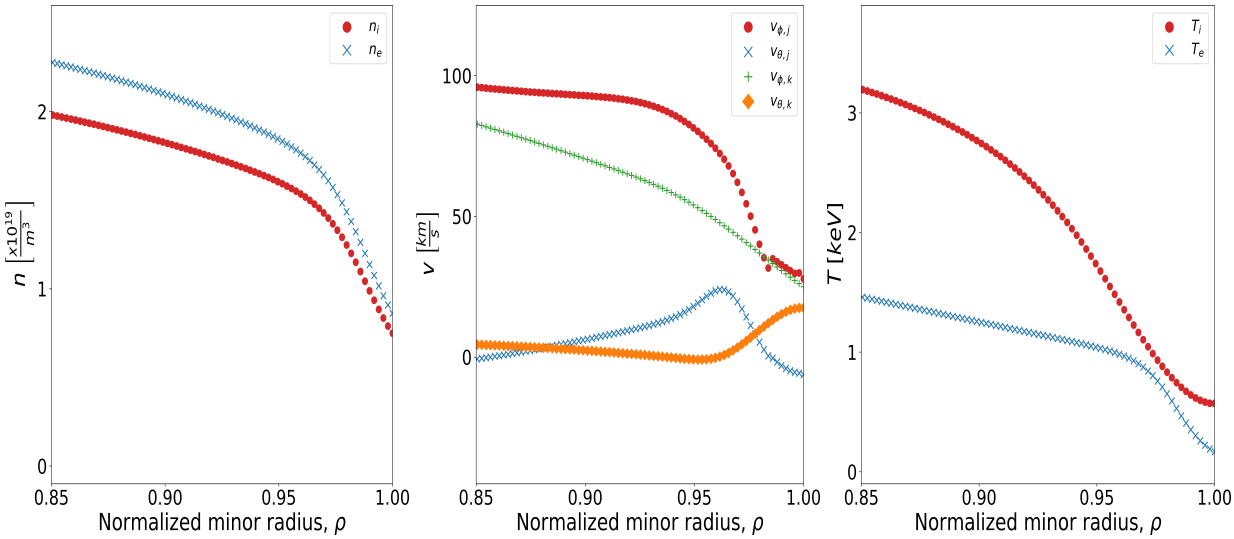

(a) (b) (c)

Figure A.1: From left to right: Plasma densities, rotation velocities, and temperatures for matched RMP shot 123301 at 2800ms

Shot 123302 - 2810 ms

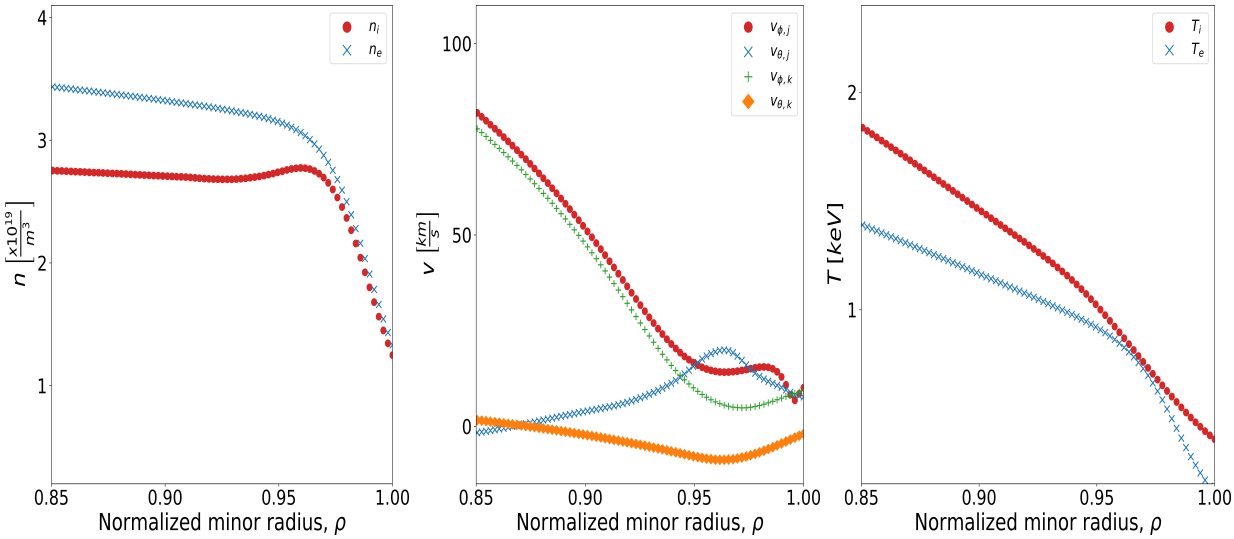

(a) (b) (c)

Figure A.2: From left to right: Plasma densities, rotation velocities, and temperatures for matched RMP shot 123302 at 2800ms

Shot 144977 - 925 ms - L-Mode

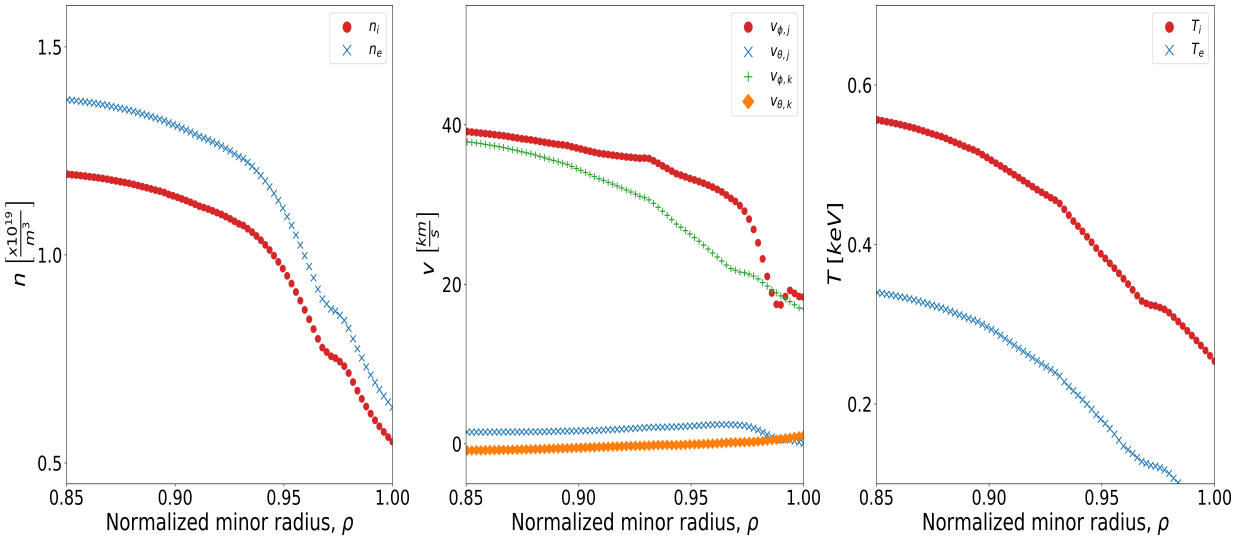

(a) (b) (c)

Figure A.3: From left to right: Plasma densities, rotation velocities, and temperatures for H-mode shot 144977 at 925 ms in L-mode

Shot 144977 - 3000 ms - H-Mode

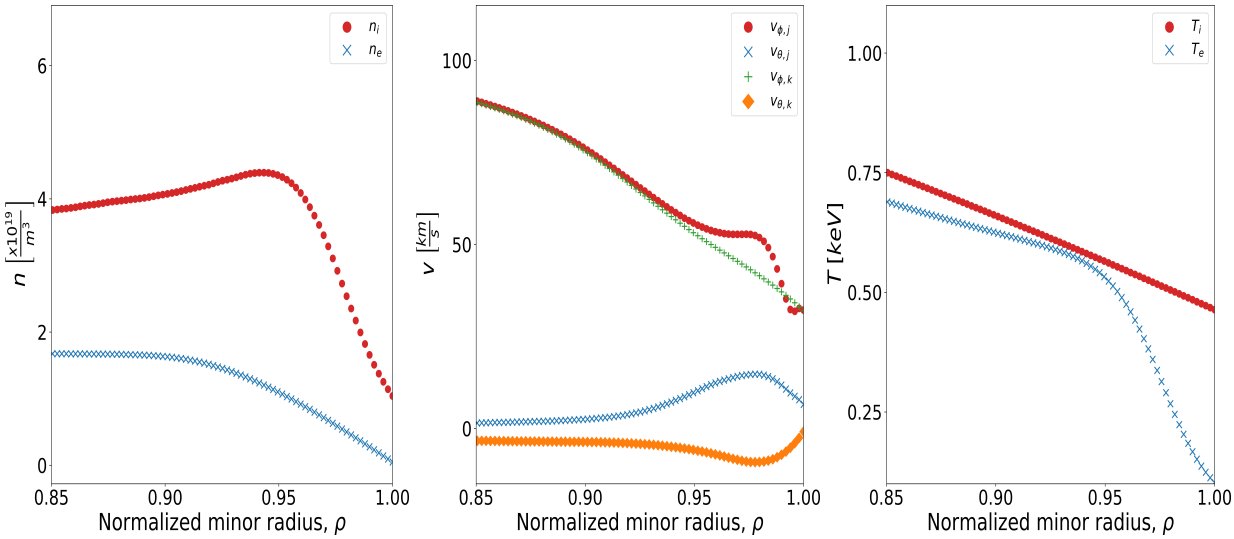

(a) (b) (c)

Figure A.4: From left to right: Plasma densities, rotation velocities, and temperatures for H-mode shot 144977 at 3000 ms in H-mode

Shot 163477 - 1800 ms

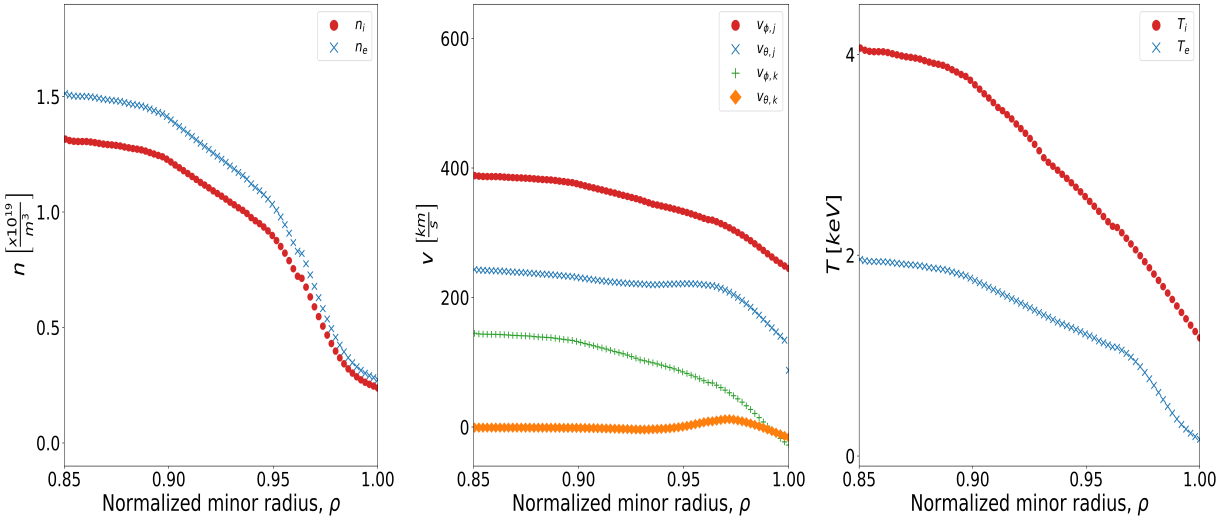

(a) (b) (c)

Figure A.5: From left to right: Plasma densities, rotation velocities, and temperatures for QH-mode shot 163477 at 1800 ms

Shot 163518 - 2350 ms

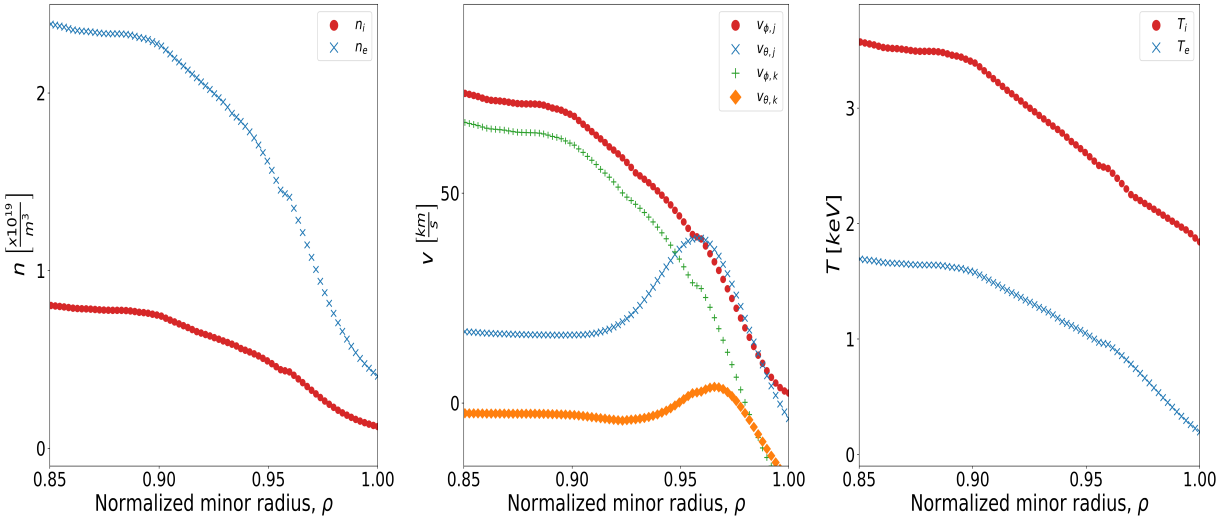

(a) (b) (c)

Figure A.6: From left to right: Plasma densities, rotation velocities, and temperatures for QH-mode shot 163518 at 2350 ms

Shot 164436 - 3740 ms

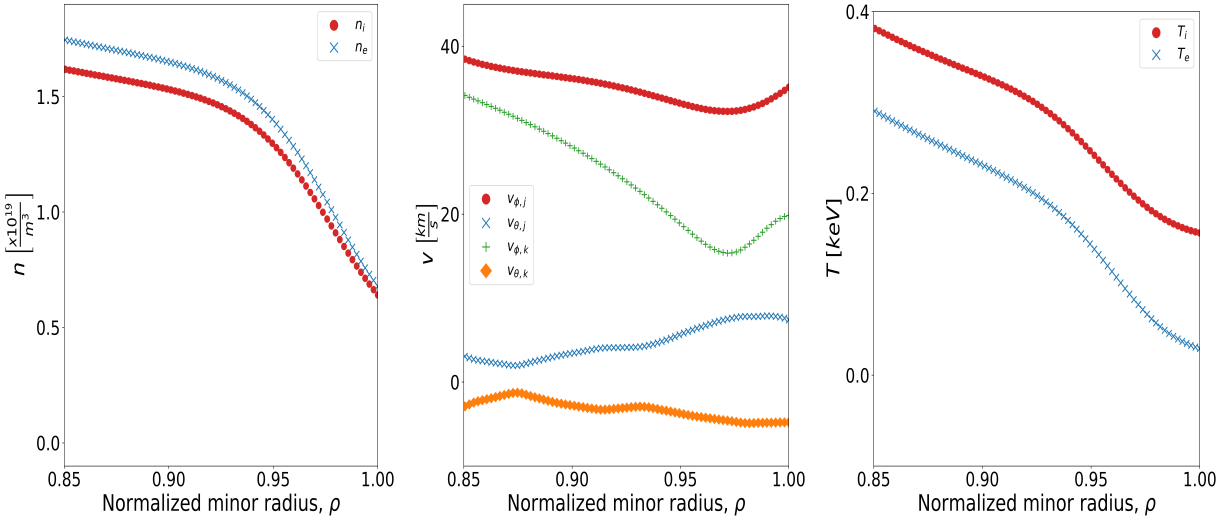

(a) (b) (c)

Figure A.7: From left to right: Plasma densities, rotation velocities, and temperatures for QH-mode shot 164436 at 3740 ms

Shot 170672 - 1900 ms

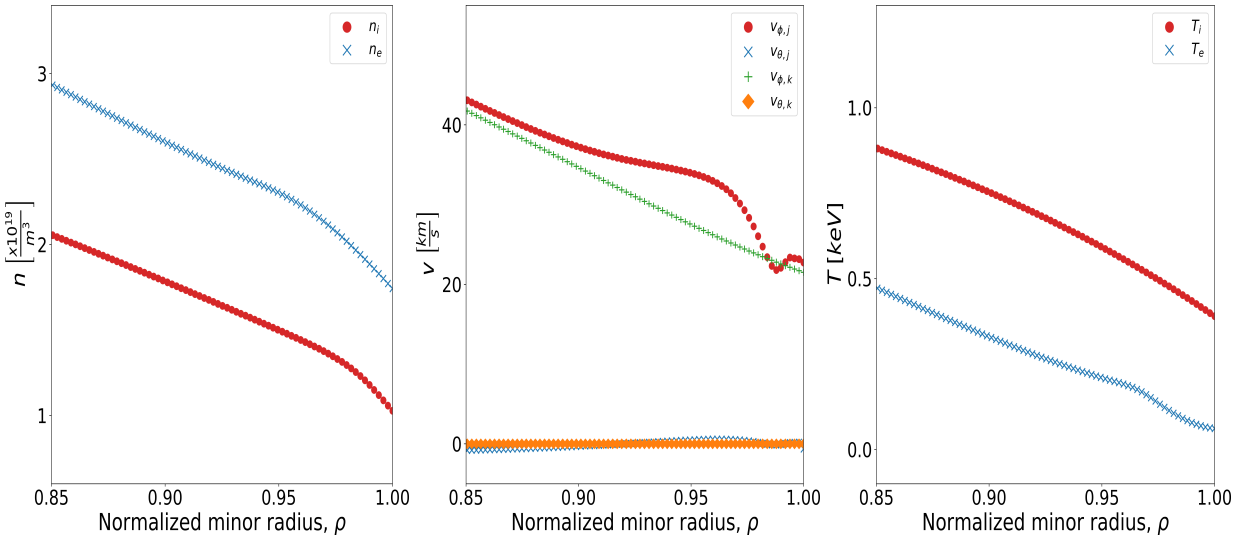

(a) (b) (c)

Figure A.8: From left to right: Plasma densities, rotation velocities, and temperatures for negative triangularity shot 170672 at 1900 ms.

Shot 174783 - 2100 ms

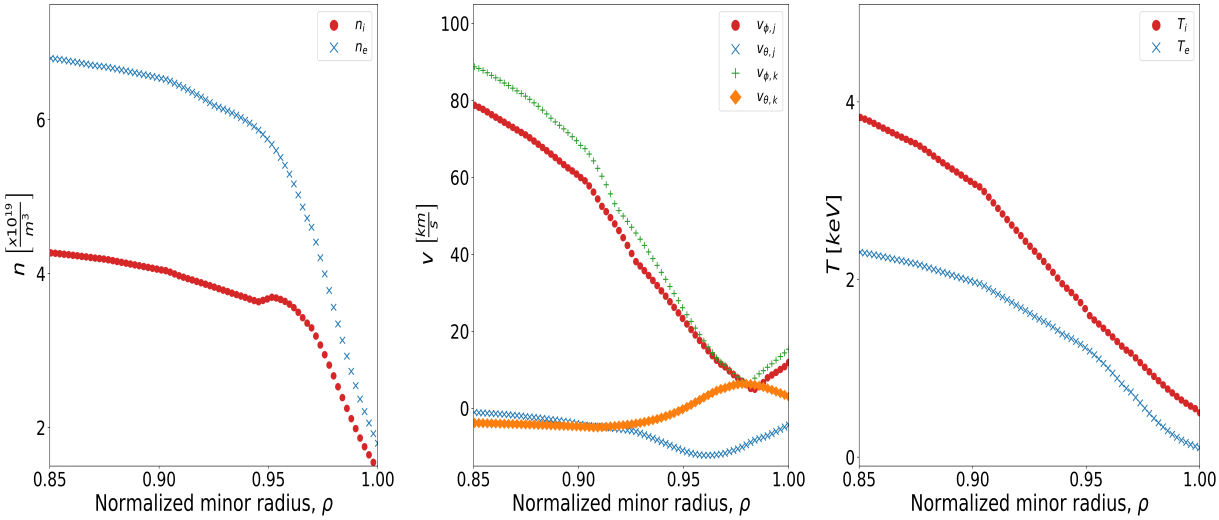

(a) (b) (c)

Figure A.9: From left to right: Plasma densities, rotation velocities, and temperatures for SH-mode shot 174783 at 2100 ms.

APPENDIX B

GTEDGE2 USER MANUAL

The following is a user guide for the GTEDGE2 Python package. GTEDGE2 calculates various plasma values from experimentally obtained and inferred values. GTEDGE2 starts with background plasma values (e.g., main ion and electron densities, rotation velocities, flux values, and NBI parameters) in 0-, 1-, or 2-D and computes cross sections; IOL values for thermalized ions, NBI ions, alphas, etc.; impurity radiation; NBI heating and fueling; neutrals recycling (when coupled to NeutPy); and radial transport values.

B.1 Installation from PyPi

GTEDGE2 can be installed in the usual manners: from PyPi using pip and from GitHub (https://github.com/gt-frc/gt3).

B.1.1 Installing via pip

Pip, the Python management system, can be used to install GTEDGE2 as a package to your Python 3 environment.

Install python as follows:

```
$ pip install gt3
```

To install the development version, use

```
$ pip install git+https://github.com/gt-frc/gt3@development
```

B.1.2 Installing via Git

GTEDGE2 can also be installed from GitHub via git:

```
$ git clone https://github.com/gt-frc/gt3.git
```

B.1.3 Neutrals Calculations

GTEDGD2 utilizes NeutPy (https://github.com/gt-frc/neutpy) for the calculation of the neutral particles recycling from the wall. NeutPy is an optional dependency. NeutPy also requires the Triangle 2D meshing package (see the NeutPy GitHub for details).

To install NeutPy

```
$ pip install neutpy
```

B.2 Preparing Input Files

An example of a GTEDGE2 input file can be found at the Fusion Research Center GitHub (https://github.com/gt-frc/gt3). See the development branch for examples of input fles. Input files go into an `inputs` directory immediately below your current working directory (CWD). A configuration file for each shot is required. GTEDGE2 uses the `configparser`

package to parse a configuration; thus, please use the format found in the example input files.

B.2.1 Example GTEDGE2 Shot Configuration

An example GTEDGE2 shot configuration file is show below:

```
[1DProfiles]

ne_file          = inputs/175826_2010/gt3_175826_2010_ne.dat
nD_file          = inputs/175826_2010/gt3_175826_2010_ni.dat
Te_file          = inputs/175826_2010/gt3_175826_2010_Te.dat
Ti_file          = inputs/175826_2010/gt3_175826_2010_Ti.dat
er_file          = inputs/175826_2010/gt3_175826_2010_Er.dat
fz1_file         = inputs/175826_2010/gt3_175826_2010_fz1.dat
fracz_file       = inputs/175826_2010/gt3_175826_2010_fracz.dat
exlti_file       = inputs/175826_2010/gt3_175826_2010_exlti.dat
exlte_file       = inputs/175826_2010/gt3_175826_2010_exlte.dat
exlni_file       = inputs/175826_2010/gt3_175826_2010_exlni.dat
vpolC_file       = inputs/175826_2010/gt3_175826_2010_vpolC.dat
vtorC_file       = inputs/175826_2010/gt3_175826_2010_vtorC.dat
vpolD_file       = inputs/175826_2010/gt3_175826_2010_vpolD.dat
vtorD_file       = inputs/175826_2010/gt3_175826_2010_vtorD.dat
q_file           = inputs/175826_2010/gt3_175826_2010_q.dat
zbar2_file       = inputs/175826_2010/gt3_175826_2010_zbar2.dat
beams_json       = inputs/175826_2010/gt3_175826_2010_beams.json
beams_out_json   = inputs/175826_2010/gt3_175826_2010_beamOut.json
neutfile_loc     = inputs/175826_2010/gt3_175826_2010_neutsOut.json

[2DProfiles]

psirz_file       = inputs/175826_2010/gt3_175826_2010_psirz.txt

[Wall]

wall_file        = inputs/175826_2010/gt3_diiid_wall.dat

[Plasma]

BT0 = -1.899
R_loss = 0.5
```

```
pfr_ni_val = 1.0E14
pfr_ne_val = 1.0E14
pfr_Ti_val = 0.002
pfr_Te_val = 0.002

[Mesh]

thetapts_approx = 30
rhopts = 201
edge_rho = 0.8
rhopts_edge = 100
rhopts_core = 10
sollines_psi_max = 1.07
num_sollines = 6
xi_ib_pts = 10
xi_ob_pts = 10
core_pol_pts = 30
numcos = 8


[Misc]
verbose = 1
d3d_iter = 1
```

Table B.1: GTEDGE2 File Specifications

Variable	**Description**	**Format**	**Units**	**Notes**
ne_file	Electron Density	(rho, val)	$\frac{\#}{m^3}$	1-D Values
nD_file	Main Ion Density	(rho, val)	$\frac{\#}{m^3}$	1-D Values
Te_file	Electron Temperature	(rho, val)	keV	1-D Values
Ti_file	Main Ion Temperature	(rho, val)	keV	1-D Values
er_file	Radial Electric Field	(rho, val)	$\frac{kV}{m}$	1-D Values
fracz_file	Charge Fraction	(rho, val)	1	1-D Values
vpolC_file	Poloidal Carbon Velocity	(rho, val)	$\frac{m}{s}$	1-D Values
vtorC_file	Toroidal Carbon Velocity	(rho, val)	$\frac{m}{s}$	1-D Values
beams_json	NBEAMS Input	(rho, val)	N/A	JSON Format
beams_out$_{json}$	NBEAMS Output	(rho, val)	N/A	JSON Format
neutfile_loc	Location of NeutPy Output	(rho, val)	N/A	JSON Format
psirz_file	RZ psi data	(R, Z, val)	1	Can be unnormalized
wall_file	Vessel Boundary	(R, Z)	1	R,Z values defining the vessel wall
BT0	Total Magnetic Field (Magnetic Axis)	val	T	None

Table B.2: GTEDGE2 File Specifications (cont.)

Variable	**Description**	**Format**	**Units**	**Notes**
R_loss	IOL Return Fraction	$0 < x < 1$	N/A	Estimated number of ions on loss orbits that re-enter plasma
pfr_ni_val	Ion Density In PFR	val	$\frac{\#}{m^3}$	Estimate of ion density in the private flux region
pfr_ne_val	Electron Density In PFR	val	$\frac{\#}{m^3}$	Estimate of electron density in the private flux region
pfr_ti_val	Ion Temperature In PFR	val	keV	Estimate of ion temperature in the private flux region
pfr_te_val	Electron Temperature In PFR	val	keV	Estimate of electron temperature in the private flux region

B.3 Running GTEDGE2

The `gt3` object can be instantiated with

```
from GT3 import gt3

plasma = gt3(inputFile=<filename>)
```

where `<filename>` is an input file as described above. In general, you'll want to execute the full radial transport code:

```
plasma.run_radial_transport()
```

The `gt3` object can take kwargs, which can be found in the `gt3.py` file or in subsection B.4.1.

A `gt3` object can essentially be considered as the full plasma results for a single time slice.

Radial transport results, neutral beam heating, etc. can be obtained via the `gt3` object.

B.4 Objects

B.4.1 Submodule: GT3

The `GT3` module holds the `gt3` object.

Attributes

gt3.iolFlag
: A boolean indicating whether to apply the Ion Orbit Loss module (see subsection B.4.4) results to the radial transport calculations. Default: *True*.

gt3.neutFlag
: A boolean indicating whether to apply the Neutrals module (see subsection B.4.6)

results to the radial transport calculations. This is helpful when examining whether neutral particle interactions are important in sensitivity studies. Default: *True*.

gt3.verbose
A boolean indicating whether to increase the verbosity of the code. Default: *False*.

gt3.beamPowerFracOverride
A `list` or `None` for providing an overwrite of the Neutral Beam Injector module's (see subsection B.4.5) neutral beam injector power fraction. This is useful when the default DIII-D power fraction split is not accurate for a given shot. Should be modified via `gt3.override_NBI_Pwrfrac(<list>)`. Default: *None*.

gt3.ntrl_cpu_override
A `int` or `False` for providing a limit on the number of CPUs that NeutPy will utilize. By default, NeutPy will utilize all CPUs available. Note that NeutPy can use multiple processors but does not gain much beyond about 12 cores. Default: *False*.

gt3.neutpyLoaded
Boolean indicating whether NeutPy was able to be loaded.

gt3.core
The attached `Core` instance (see subsection B.4.3).

gt3.inp
The attached `ReadInfile` instance (see subsection B.4.2).

gt3.iol
The attached `IOL` instance (see subsection B.4.4).

gt3.nbi
The attached `BeamDeposition` instance (see subsection B.4.5).

gt3.imp
The attached `ImpRad` instance (see **??**).

gt3.ntrl
The attached `Neutrals` instance (see subsection B.4.6).

gt3.rtrans
The attached `RadialTransport` instance (see subsection B.4.7).

gt3.run_SOL(self)
Run the `SOL` module to calculate scrape-off layer values. Attaches an SOL instance to the `gt3` instance.

gt3.run_SOL(self)

Run the `SOL` module to calculate scrape-off layer values. Attaches an SOL instance to the `gt3` instance.

gt3.run_IOL(self)

Run the `IOL` module to calculate the Ion Orbit Loss loss fractions. Attaches an IOL instance to the `gt3` instance.

gt3.run_NBI(self)

Run the `NBI` module to calculate the neutral beam injector deposition profiles and relevant sources. Attaches a `BeamDeposition` instance to the `gt3` instance.

gt3.run_NBI(self, reRun=False)

Run the `NBI` module to calculate the neutral beam injector deposition profiles and relevant sources. Attaches a `BeamDeposition` instance to the `gt3` instance. If a `gt3.nbi` instance already exists but you would like the re-run the computation, set `reRun=True`.

gt3.run_impurities(self)

Run the `Impurity Radiation` module to calculate values related to impurity radiation. Attaches an `ImpRad` instance to the `gt3` instance. Currently requires L_z interpolators to be located in the `Lz_interpolators` folder shipped with GTEDGE2.

gt3.run_neutrals(self, reRun=False)

Run the `Neurals` module to run NeutPy. Attaches a `Neutrals` instance to the `gt3` instance. If a `gt3.neuts` instance already exists but you would like to re-run NeutPy, set `reRun=True`.

gt3.override_ntrl_cpus(self, num)

Set the NeutPy CPU limit.

gt3.run_radial_transport(self, nbiReRun=False, ntrlReRun=False)

Run the `Radial Transport` module. Attaches a `RadialTransport` instance to the `gt3` instance. If a `gt3.rtrans` instance already exists but you would like to re-run NeutPy and/or the `Beam Deposition` module, set `ntrlReRun=True` and/or `nbiReRun=True`.

gt3.disable_IOL(self)

Disable the Ion Orbit Loss module. This is useful when comparing a shot with and without IOL effects.

gt3.disable_neutrals(self)

Disable the Neutrals module. This is useful when comparing a shot with and without neutral particle effects.

B.4.2 Module: ReadInfile

The `ReadInFile` module is responsible for parsing input data based on the **inputFile** argument passed to GTEDGE2. The module reads in various values using the `configparser` standard python package. The constructor takes in kwargs that allow the input files to be manipulated, e.g., by scaling or shifting profiles and 0-D values.

B.4.3 Core

The `Core` module provides the background plasma generated from the input files. The workflow for `Core` is shown in Figure B.1. The `Core` submodule first uses the supplied 2D psi data to calculate various plasma parameters, including the location of the magnetic axis, geometric axis, strike points, X-points, triangularity, etc. The plasma is then meshed according to the number of rho, theta points given in the shot input file. Using this meshing, various interpolators are generated. These interpolators include **core.r2sa**, which interpolates a given r value to the surface area at that r value, **core.r2vol**, which interpolates a given r value to the plasma volume at that r value, and many others.

Using these calculations, 1D and 2D profiles of various plasma profiles are generated based on the input data and interpolators. These profiles utilize the `OneDProfile` and `TwoDProfile` classes. These classes provide numerous calculation and plotting abilities, augmenting the standard `numpy` ndarray object.

Finally, various cross-sections are calculated using empirical fits.

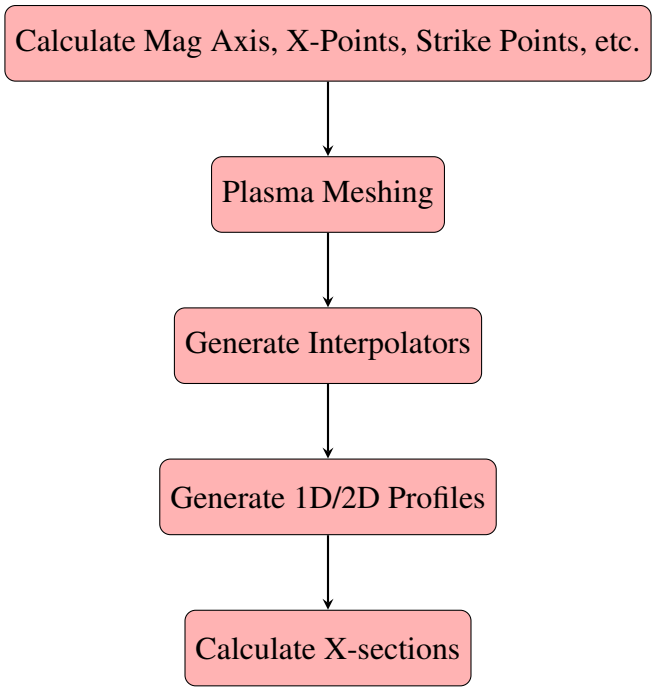

Figure B.1: GTEDGE2's GT3 Core workflow.

Attributes

core.inp
: The `ReadInfile` instance attached to this `gt3` instance.

core.wall_line
: The `Shapely` wall line providing the boundary of the plasma vessel.

core.pts
: The `Points` instance for this background plasma. Includes the coordinates of the inboard midplane (**core.pts.ibmp**), outboard midplane (**core.pts.obmp**), inferred top of the plasma (**core.pts.top**), inferred bottom of the plasma (**core.pts.bottom**), the x-point(s) (**core.pts.xpt**), the PlasmaAxis object (**core.pts.axis**), and the StrikePoints object (**core.pts.strike**).

core.lines
: The `DivertorLines` instance for this background plasma. Includes `Shapely.LineString` or `ShapelyLineRing` versions of the Last Closed Flux Surface (LCFS) (**core.lines.sep** and **core.lines.sep_closed**), the divertor legs (**core.lines.div**), and the line connecting the inboard strike point to the outboard strike point (**core.lines.ib2ob**).

core.R0_a
: The major radius of the magnetic axis as inferred from psi data.

core.R0_g
: The major radius of the geometric axis as inferred from psi data.

core.rhopts
The number of rho values in the main computational grid.

core.thetapts
The number of theta values in the main computational grid.

core.theta, core.rho
Main rho,theta computational grid initialized using the `numpy` `meshgrid` class.

core.kappa_vals
The elongation of the plasma as calculated at the $\psi_{norm} = 0.95$ flux surface (**core.kappa_vals.sep**) and near the magnetic axis (**core.kappa_vals.axis**).

core.tri_vals
The triangularity of the plasma as calculated at the $\psi_{norm} = 0.95$ flux surface (**core.tri_vals.sep**) and near the magnetic axis (**core.tri_vals.axis**).

core.a
The inferred plasma radius.

core.R, core.Z
Main R,Z computational grid generated by drawing flux surfaces using `Shapely` and utilizing important plasma points.

core.r2sa, core.rho2sa, core.psinorm2sa
Interpolators for interpolating from r, ρ, and ψ_{norm} values to the plasma surface area.

core.r2vol, core.rho2vol, core.psinorm2vol
Interpolators for interpolating from r, ρ, and ψ_{norm} values to the plasma volume.

core.izn_rate
Ionization rates with neutral particles entering the plasma. Initially is zeroed out and is populated once the NeutPy package is run.

core.cool_rate
Cooling rate from interaction with neutral particles entering the plasma. Initially is zeroed out and is populated once the NeutPy package is run.

core.n
A `DensityProfiles` object containing particle densities (in $\frac{\#}{m^3}$). Depending on what input data are given, main ion, electron, carbon, tungsten, alphas, neutrals (slow, fast, and total), and other densities are provided. By default, all attributes are `TwoDProfile` instances, except for neutral densities, which are `OneDProfile` instances.

core.T
A `TemperatureProfiles` object containing particle temperatures (in J, eV, and keV). Only ion, electron, carbon, and neutrals temperatures are currently supported. Temperatures are given as `TwoDProfile` instances.

core.E_r
A `TwoDProfile` instance of the radial electric field.

core.E_pot
A `TwoDProfile` instance of the radial electric potential.

core.v
A `VectorialProfiles` instance providing rotation data for main ion and carbon impurities.

core.B
A `VectorialBase` instance providing magnetic field data (in T). The poloidal

magnetic field is accessed with **core.B.pol**, the toroidal field is accessed with **core.B.tor**, and the total field is accessed with **core.B.tot**.

core.update_ntrl_data(self, data)

When `NeutPy` is run or if neutrals data are to be updated manually, this function will set neutral densities and temperatures, along with ionization and cooling rates.

B.4.4 Ion Orbit Loss

The Ion Orbit Loss subroutine calculates the Ion Orbit Loss (IOL) loss rates based on truncated maxwellian distributions. This submodule calculates these loss fractions following the physics discussed in chapter 4. The submodule provides thermalized and fast loss fractions for particle, energy, and momentum in both 2D and 1D.

Attributes

iol.forb_d_therm, iol.eorb_d_therm, iol.morb_d_therm

The differential particle number, energy, and momentum loss fractions for the thermalized main ion species on the 2D computational grid.

iol.forb_d_therm_1D, iol.eorb_d_therm_1D, iol.morb_d_therm_1D

The differential particle number, energy, and momentum loss fractions for the thermalized main ion species in 1D.

iol.forb_c_therm, iol.eorb_c_therm, iol.morb_c_therm

The differential particle number, energy, and momentum loss fractions for the thermalized carbon impurities on the 2D computational grid.

iol.forb_c_therm_1D, iol.eorb_c_therm_1D, iol.morb_c_therm_1D

The differential particle number, energy, and momentum loss fractions for the thermalized carbon impurities in 1D.

iol.forb_a_therm, iol.eorb_a_therm, iol.morb_a_therm

The differential particle number, energy, and momentum loss fractions for the thermalized alpha particles on the 2D computational grid.

iol.forb_a_therm_1D, iol.eorb_a_therm_1D, iol.morb_a_therm_1D

The differential particle number, energy, and momentum loss fractions for the thermalized alpha particles in 1D.

iol.forb_a_fast, iol.eorb_a_fast, iol.morb_a_fast

The differential particle number, energy, and momentum loss fractions for the fast alpha particles on the 2D computational grid.

iol.forb_a_fast_1D, iol.eorb_a_fast_1D, iol.morb_a_fast_1D

The differential particle number, energy, and momentum loss fractions for the fast alpha particles in 1D.

iol.forb_d_nbi, iol.eorb_d_nbi, iol.morb_d_nbi

The differential particle number, energy, and momentum loss fractions for the neutral-beam-injected ions on the 2D computational grid.

iol.forb_d_nbi_1D, iol.eorb_d_nbi_1D, iol.morb_d_nbi_1D

The differential particle number, energy, and momentum loss fractions for the neutral-

beam-injected ions in 1D.

iol.plot_F_i(self), iol.plot_E_i(self), iol.plot_M_i(self)

Plots the differential main ion particle, energy, and momentum loss fractions in 1D.

iol.plot_all_i(self) Plots all loss fractions on one graph in 1D

B.4.5 Beam Deposition

The `BeamDeposition` class utilizes a re-written version of the NBEAMS [79] FORTRAN code. The `BeamDeposition` class acts as a wrapper around multiple `Beam` classes. The `BeamDeposition` takes as input `ReadInfile` and `Core` instances, with an optional `IOL` instance. The class generates a meshing specifically for the neutral beam deposition (with a radial spacing lower than the main computational grid given the more intensive computations involved).

Note that given the computationally intensive nature of the `BeamDeposition` class, once run, `BeamDeposition` will output a JSON-formatted file (filename defined in the shot input configuration) with the results of the shot run. To overwrite this and force a rerun, a **reRun** flag is available.

The workflow for `BeamDeposition` is shown in Figure B.2.

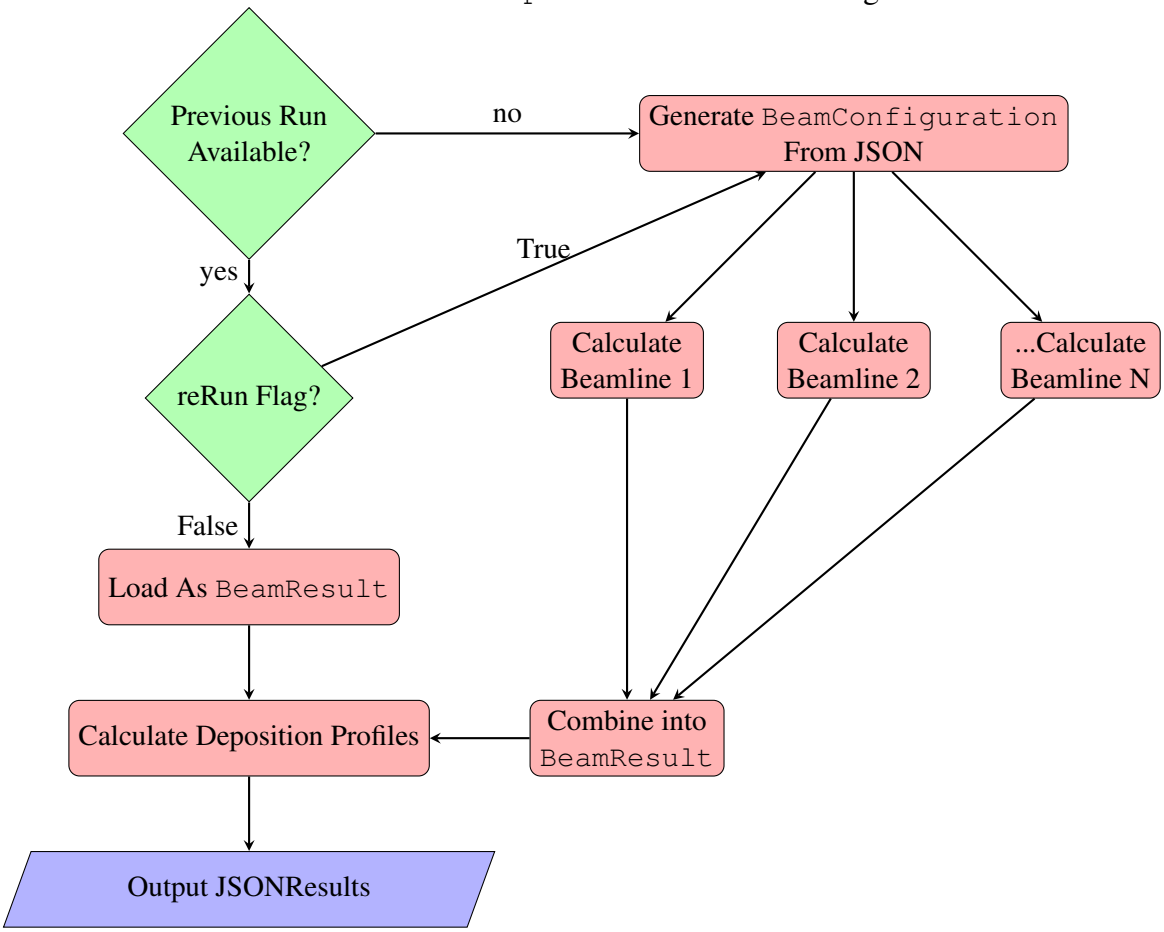

Figure B.2: GTEDGE2's GT3 BeamDeposition workflow.

B.4.6 Neutrals Recycling

The `Neutrals` class is coupled to the GTNEUTPY neutrals recycling code based on the transmission-and-escape probability method. If `NeutPy` is not installed, this module will be unavailable for use in subsequent computations. The `Neutrals` class first attempts to open a previously run neutrals recycling calculation to load ionization rates and neutral density. If a previous run has not been found or the $\mathbf{ntrl.reRun}$ method in `Neutrals` is invoked, `NeutPy` will be run. `NeutPy` uses Bohm diffusion to estimate the densities and temperatures in the SOL and PFR.

Attributes

ntrl.core
The `Core` instance for this run.

ntrl.data
The data provided from the `NeutPy` run or from a previous saved file.

ntrl.inp
The `ReadInFile` instance for this run.

ntrl.npi
The `NeutPy` instance for this run if not using data from a previous safe file.

ntrl.reRun(self, cpus=False, *args, **kwargs)
A method for forcing `NeutPy` to be run. **cpus** sets the number of cpus to use. This is also set in the `NeutPy` main configuration file.

B.4.7 Radial Transport

The `RadialTransport` class performs the 1.5D calculations for inferring many radial transport properties.

Underlying Physics

The `RadialTransport` class utilizes flux-surface-averaged values, generally obtained with the $\mathbf{fsa}()$ method attached to most quantities used within. The radial particle flux is inferred in 1D slab geometry using the `SciPy ODE` integrator as follows:

$$\frac{d\hat{\Gamma}_i}{dr} = n_e(r)\nu_{ion}(r) + n_e(r)\nu_{cx}(r) + S_{nbi} - \hat{\Gamma}_i\frac{dF_{iol}}{dr}$$

using the NBI and neutrals ionization sources from the `BeamDeposition` and `Neutrals` classes. The IOL differential loss fractions are taken from the `IOL` class for thermalized and nbi ions. Calculations are made separately with and without IOL corrections to facilitate comparisons. Next, the radial momentum balance terms are calculated to facilitate further calculations such as the intrinsic rotation. The momentum balance is also used to calculate the ion toroidal velocity using perturbation theory if this value is not given beforehand.

Momentum balance is then used to calculate the poloidal ion velocity if not provided as well.
Various collision rates are then calculated. The drag frequency is calculated from

$$n_j^0 m_j \nu_{jk}^0 (1 + \frac{\nu_{d,j}}{\nu_{jk}^0} v_{\phi,j}^0 - v_{\phi,k}^0) = n_j^0 e_j E_\phi^A + e_j B_\theta^0 \Gamma_{r,j} + M_{\phi,j}^0$$

The pinch velocity is also calculated in this class.
The ion and electron radial heat fluxes are calculated similarly to the radial ion particle flux:

$$\frac{\partial Q_i^{tot}}{\partial r} = -\frac{\partial}{\partial t}\left(\frac{3}{2} n_i T_i\right) + q_{nbi} - \frac{3}{2}(T_i - T_0^c) n_i n_0^c < \sigma v >_{cx+el} - q_{ie}$$

$$\frac{\partial Q_e^{tot}}{\partial r} = -\frac{\partial}{\partial t}\left(\frac{3}{2} n_e T_e\right) + q_{nbe} + q_{ie} - n_e n_0 < \sigma v >_{ion} E_{ion} - n_e n_z L_z$$

The radial heat fluxes are calculated as follows:

$$Q_i^{\text{conv}} = \frac{3}{2} \hat{\Gamma}_{r,i} T_i^{\text{exp}}$$

$$Q_i^{\Pi} = \hat{\Gamma}_{r,i} T_i^{\text{exp}}$$

$$Q_i^{\text{in}} = \frac{1}{2} n_i m_i \left(\vec{V}_i \cdot \vec{V}_i\right) V_{r,i} = \frac{1}{2} \hat{\Gamma}_{r,i} m_j \vec{v}^2$$

$$Q_i^{\text{visc}} = \frac{1}{R_0} V_{\phi,i}^0 V_{\phi,i}^s [\eta_0 f_p V_{r,i}^0 - \eta_{4,i}(2V_{\phi,i}^0 + \frac{1}{2} V_{\theta,i}^0] - \frac{1}{2} V_{\theta,i}^0 V_{\theta,i}^s [\eta_{0,i} V_{r,i}^0 + \eta_{4,i}(V_{\phi,i}^0 + \frac{1}{2} V_{\theta,i}^0)]$$

where

$$\eta_{0,i} = \frac{n_i m_i V_{\theta,i} q R \epsilon^{-3/2} \nu_i^*}{(1 + \epsilon^{-3/2} \nu_i^*)(1 + \nu_i^*)}$$

$$\eta_{4,i} = \frac{n_i T_i}{\Omega_i}$$

in which $\Omega_i = Z_i e B / m_i$, $\nu^* = \nu_{90} q R_{0,a} / V_{th,i}$, and $\epsilon = a/R_0$.
The conductive heat flux is given by

$$q^{\text{cond}} = \hat{Q}^{\text{tot}} - Q^{\text{conv}} - Q^{\Pi} - Q^{\text{heatin}} - Q^{\text{visc}}$$

$\chi_{r,j}$ and $D_{r,j}$ are calculated as follows:

$$\chi_i = \frac{q_i^{\text{cond}} \left(-\frac{1}{T_i} \frac{\partial T_i}{\partial r}\right)^{-1}}{n_i T_i} = \frac{q_i^{cond} L^{-1}}{n_i T_i}$$

$$D_j = \frac{m_j T_j \nu_{j,k}}{(e_j B_\theta)^2} \left[1 + \frac{\nu^*_{d,j}}{\nu_{j,k}} - \frac{Z_j}{Z_i} \right]$$

Attributes

To be added...

REFERENCES

[1] W. M. Stacey, *Fusion Plasma Physics*. John Wiley & Sons, 2012.

[2] V. D. Shafranov, B. Bondarenko, G. A. Goncharov, O. A. Lavrent'ev, A. D. Sakharov, *et al.*, "On the history of the research into controlled nuclear fusion", *Physics-Uspekhi*, vol. 44, no. 8, pp. 835–843, 2001.

[3] M. D. Hill, "BURN CONTROL MECHANISMS IN TOKAMAK FUSION REACTORS", PhD thesis, 2019.

[4] F. Wagner *et al.*, "Regime of Improved Confinement and Hihg Beta in Neutral-Beam-Heated Divertor Discharges of the ASDEX Tokamak", *Physical Review Letters*, vol. 49, no. 19, 1982.

[5] A. E. Hubbard, "Physics and scaling of the H-mode plasma", *Plasma Physics and Controlled Fusion*, vol. 42, A15–A30, 2000.

[6] D. N. Hill, "A review of ELMs in divertor tokamaks", *Journal of Nuclear Materials*, pp. 182–198, 1997.

[7] J. Stober *et al.*, "Type II ELMy H modes on ASDEX Upgrade with good confinement at high density", *Nuclear Fusion*, vol. 41, 2001.

[8] K. H. Burrell *et al.*, "Quiescent double barrier high-confinement mode plasmas in the DIII-D tokamak", *Physics of Plasmas*, vol. 8, no. 5, 2001.

[9] K. H. Burrell *et al.*, "Advances in understanding quiescent H-mode plasmas in DIII-D", *Physics of Plasmas*, vol. 12, 2005.

[10] A. M. Garofalo *et al.*, "The quiescent H-mode regime for high performance edge localized mode-stable operation in future burning plasmas", *Physics of Plasmas*, vol. 22, 2015.

[11] W. M. Solomon *et al.*, "Access to a New Plasma Edge State with High Density and Pressures using the Quiescent H Mode", *Physical Review Letters*, vol. 113, 2014.

[12] P. B. Snyder *et al.*, "A first-principles predictive model of the pedestal height and width: development, testing and ITER optimization with the EPED model", *Nuclear Fusion*, vol. 51, no. 10, 2011.

[13] J. R. Walk *et al.*, "Characterization of the pedestal in Alcator C-Mod ELMing H-modes and comparison with the EPED model", *Nuclear Fusion*, vol. 52, no. 6, 2012.

[14] K. Li *et al.*, "Study of H-mode pedestal model for helium plasmas in DIII-D", *Nuclear Fusion*, vol. 61, no. 9, 2021.

[15] P. B. Snyder *et al.*, "Super H-mode: theoretical prediction and initial observations of a new high performance regime for tokamak operation", *Nuclear Fusion*, vol. 55, 2015.

[16] P. B. Snyder *et al.*, "High fusion performance in Super H-mode experiments on Alcator C-Mod and DIII-D", *Nuclear Fusion*, vol. 59, 2019.

[17] M. Knolker *et al.*, "On the stability and stationarity of the Super H-mode combined with an ion transport barrier in the core", *Plasma Physics and Controlled Fusion*, vol. 63, 2021.

[18] M. Knolker *et al.*, "Optimizing the Super H-mode pedestal to improve performance and facilitate divertor integration", *Physics of Plasmas*, vol. 27, 2020.

[19] W. M. Stacey, "Sensitivity of the interpretation of the experimental ion thermal diffusivity to the determination of the ion conductive heat flux", *Physics of Plasmas*, vol. 21, no. 4, p. 042 508, 2014.

[20] J. Mandrekas, "GTNEUT: A code for the calculation of neutral particle transport in plasmas based on the transmission and escape probability method", *Computer Physics Communications*, p. 36, 2004.

[21] W. Stacey, "Thermal transport analysis of the edge region in the low and high confinement stages of a DIII-D discharge", *Physics of Plasmas*, vol. 14, no. 1, 2007.

[22] J. E. Kinsey *et al.*, "Burning plasma projections using drift-wave transport models and scalings for the H-mode pedestal", *Nuclear Fusion*, vol. 43, 2003.

[23] R. Aymar *et al.*, "Overview of ITER-FEAT - The future international burning plasma experiment", *Nuclear Fusion*, vol. 41, no. 10, 2001.

[24] T. H. Osborne *et al.*, "H-mode pedestal characteristics, ELMs, and energy confinement in ITER shape discharges on DIII-D", *Plasma Physics and Controlled Fusion*, vol. 40, no. 845, 1998.

[25] J. Callen *et al.*, "Analysis of pedestal plasma transport", *Nuclear Fusion*, vol. 50, no. 064004, 2010.

[26] W. Stacey and R. Groebner, "Thermal transport in the DIII-D edge pedestal", *Physics of Plasmas*, vol. 13, p. 072 510, 2006.

[27] W. M. Stacey, "Ion Particle Transport in the Tokamak Edge Plasma", *Contributions to Plasma Physics*, vol. 48, no. 1, pp. 94–98, 2008.

[28] W. M. Stacey and T. E. Evans, "Investigation of background edge thermal transport in ELMing and ELM-suppressed H-modes in DIII-D", *Physics of Plasmas*, vol. 13, p. 112 506, 2006.

[29] W. Stacey, "Comparison of theoretical and experimental heat diffusivities in the DIII-D edge plasma", *Physics of Plasmas*, vol. 15, p. 052 503, 2008.

[30] Y. Fuji, K. Itoh, A. Fukuyama, and S.-I. Itoh, "Transport Modeling of L/H Transition in Tokamaks", *Fusion Science and Technology*, vol. 27, no. 3T, 1995.

[31] W. M. Stacey and B. A. Grierson, "Interpretation of rotation and momentum transport in the DIII-D edge plasma and comparison with neoclassical theory", *Nuclear Fusion*, vol. 54, p. 073 021, 2014.

[32] W. Stacey, "The effects of rotation, electric field, and recycling neutrals on determining the edge pedestal density profile", *Physics of Plasmas*, vol. 17, p. 052 506, 2010.

[33] W. Stacey and R. Groebner, "Force balance and ion particle transport differences in high and low confinement tokamak edge pedestals", *Physics of Plasmas*, vol. 17, p. 112 512, 2010.

[34] W. M. Stacey and T. E. Evans, "The role of radial particle pinches in ELM suppression by resonant magnetic perturbations", *Nuclear Fusion*, vol. 51, 2011.

[35] W. M. Stacey, "On the physics of the pressure and temperature gradients in the edge of tokamak plasmas", *Nuclear Fusion*, vol. 58, 2018.

[36] W. Stacey, J. Boedo, T. Evans, B. Grierson, and R. Groebner, "Intrinsic rotation produced by ion orbit loss and X-loss", *Physics of Plasmas*, vol. 19, p. 112 503, 2012.

[37] W. M. Stacey, "Extended fluid transport theory in the tokamak plasma edge", *Nuclear Fusion*, vol. 57, 2017.

[38] W. M. Stacey, "A Particle-, Momentum-, and Energy-Conserving Fluid Transport Theory for the Tokamak Plasma Edge", *Fusion Science and Technology*, vol. 75, pp. 251–263, 2019.

[39] W. M. Stacey *et al.*, "Non-diffusive transport in the tokamak edge pedestal", *Nuclear Fusion*, vol. 52, p. 114 020, 2012.

[40] W. Stacey, "X-transport of ions in diverted tokamaks, with application to DIII-D", *Physics of Plasmas*, vol. 18, p. 122 504, 2011.

[41] W. Stacey, "The effect of rotation and viscous heating on the interpretation of experimental heat diffusivities in the edge pedestal", *Physics of Plasmas*, vol. 17, 2010.

[42] R. W. King, "Rotation calculation in tokamak plasma", PhD thesis, 2019.

[43] W. M. Stacey and T. M. Wilks, "Inclusion of ion orbit loss and intrinsic rotation in plasma fluid rotation theory", *Physics of Plasmas*, vol. 23, 2016.

[44] D. J. Battaglia *et al.*, "Kinetic neoclassical transport in the H-mode pedestal", *Physics of Plasmas*, vol. 21, 2014.

[45] J. Seo *et al.*, "Intrinsic momentum generation by a combined neoclassical and turbulence mechanism in diverted DIII-D plasma edge", *Physics of Plasmas*, vol. 21, 2014.

[46] W. M. Stacey, "A fluid model for the edge pressure pedestal height and width in tokamaks based on the transport constraint of particle, energy, and momentum balance", *Physics of Plasmas*, vol. 23, 2016.

[47] R. Brzozowski III *et al.*, "A geometric model of ion orbit loss under the influence of a radial electric field", *Physics of Plasmas*, vol. 26, p. 042 511, 2019.

[48] E. Viezzer *et al.*, "Investigation of inter-ELM ion heat transport in the H-mode pedestal of ASDEX Upgrade plasmas", *Nuclear Fusion*, vol. 57, 2017.

[49] E. Viezzer *et al.*, "Ion heat transport dynamics during edge localized mode cycles at ASDEX Upgrade", *Nuclear Fusion*, vol. 58, 2018.

[50] M. Rosenbluth, R. Hazeltine, and F. Hinton, "Plasma Transport in Toroidal Confinement Systems", *The Physics of Fluids*, vol. 15, no. 1, p. 116, 1972.

[51] R. Hazeltine and F. Hinton, "Collision-dominated plasma transport in toroidal confinement systems", *The Physics of Fluids*, vol. 16, no. 11, p. 1883, 1973.

[52] C. Chang and F. Hinton, "Effect of finite aspect ratio on the neoclassical ion thermal conductivity in the banana regime", *The Physics of Fluids*, vol. 25, p. 1493, 1982.

[53] C. Chang and F. Hington, "Effect of impurity particles on the finite-aspect ratio neoclassical ion thermal conductivity in a tokamak", *The Physics of Fluids*, vol. 29, p. 3314, 1986.

[54] J. Conner and H. R. Wilson, "Survey of theories of anomalous transport", *Plasma Physics and Controlled Fusion*, vol. 36, p. 719, 1994.

[55] T. Luce, C. Petty, and J. de Haas, "Inward Energy Transport in Tokamak Plasmas", *Physical Review Letters*, vol. 68, no. 1, 1992.

[56] S. R. Haskey *et al.*, "Collisionality Dependence of Ion Thermal Transport in the Pedestal Regionon DIII-D", Unpublished, 2021.

[57] B. Coppi, M. N. Rosenbluth, and R. Z. Sagdeev, "Instabilities due to Temperature Gradients in Complex Magnetic Field Configurations", *The Physics of Fluids*, vol. 10, no. 3, 1966.

[58] W. Horton and R. D. Estes, "Fluid simulation of ion pressure gradient driven drift modes", *Plasma Physics*, vol. 22, 1980.

[59] D. R. Baker *et al.*, "Comparison of gyrokinetic stability code calculated critical ion temperature gradients and growth rates to DIII-D measured gradients and diffusivities", *Physics of Plasmas*, vol. 10, 2003.

[60] D. R. Baker *et al.*, "Thermal diffusivities in DIII-D show evidence of critical gradients", *Physics of Plasmas*, vol. 8, no. 9, 2001.

[61] B. N. Rogers, J. F. Drake, and A. Zeiler, "Phase Space of Tokamak Edge Turbulence, the L-H Transition, and the Formation of the Edge Pedestal", *Physical Review Letters*, vol. 81, no. 20, 1998.

[62] W. Kerner, Y. Igitkhanov, G. Janeschitz, and O. Pogutse, "The Scaling of the Edge Temperature in Tokamaks Based on the Alfven Drift - Wave Turbulence", *Contributions to Plasma Physics*, vol. 38, pp. 118–123, 1998.

[63] J. Callen, "Paleoclassical electron heat transport", *Nuclear Fusion*, vol. 45, p. 1120, 2005.

[64] S. P. Smith *et al.*, "Comparisons of paleoclassical based pedestal model predictions of electron quantities to measured DIII-D H-mode profiles", *Nuclear Fusion*, vol. 52, 2012.

[65] M. Kotschenreuther *et al.*, "Gyrokinetic analysis and simulation of pedestals to identify the culprits for energy losses using fingerprints", *Nuclear Fusion*, vol. 59, 2019.

[66] W. Dorland, F. Jenko, M. Kotschenreuther, and B. N. Rogers, "Electron Temperature Gradient Turbulence", *Physical Review Letters*, vol. 85, no. 26, 2000.

[67] J. C. DeBoo *et al.*, "Search for a critical electron temperature gradient in DIII-D L-mode discharges", *Nuclear Fusion*, vol. 45, 2005.

[68] W. Horton *et al.*, "Electron transport and the critical temperature gradient", *Physics of Plasmas*, vol. 11, 2004.

[69] W. M. Stacey, "The effect of ion orbit loss and X-loss on the interpretation of ion energy and particle transport in the DIII-D edge plasma", *Physics of Plasmas*, vol. 18, no. 10, p. 102 504, 2011.

[70] T. M. Wilks and W. M. Stacey, "Improvements to an ion orbit loss calculation in the tokamak edge", *Physics of Plasmas*, vol. 23, p. 122 505, 2016.

[71] W. M. Stacey and T. E. Evans, "Investigation of background edge thermal transport in ELMing and ELM-suppressed H-modes in DIII-D", *Physics of Plasmas*, vol. 13, p. 112 506, 2006.

[72] T. M. Wilks, W. M. Stacey, and T. E. Evans, "Calculation of the radial electric field from a modified Ohm's law", *Physics of Plasmas*, vol. 24, 2017.

[73] T. E. Evans, K. H. Burrell, M. E. Fenstermacher, R. A. Moyer, T. H. Osborne, M. J. Schaffer, W. P. West, L. W. Yan, J. A. Boedo, E. J. Doyle, G. L. Jackson, I. Joseph, C. J. Lasnier, A. W. Leonard, T. L. Rhodes, P. R. Thomas, J. G. Watkins, and L. Zeng, "The physics of edge resonant magnetic perturbations in hot tokamak plasmas", *Physics of Plasmas*, vol. 13, no. 5, 2006.

[74] W. M. Stacey, "Recent Developments in Plasmas Edge Theory", *Contributions to Plasma Physics*, vol. 56, no. 6-8, pp. 495–503, 2016.

[75] W. M. Stacey, A. W. Bailey, D. J. Sigmar, and K. C. Shaing, "Rotation and imporuty transport in a tokamak plasma with directed neutral-beam injection", *Nuclear Fusion*, vol. 25, no. 4, p. 463, 1985.

[76] C. Bae, W. M. Stacey, and W. M. Solomon, "Extension of neoclassical rotation theory for tokamaks to realistically account for the geometry of magnetic flux surfaces", *Nuclear Fusion*, vol. 53, no. 4, p. 043 011, Mar. 2013.

[77] D. S. W.M. Stacey, "Viscous effects in a collisional tokamak plasma with strong rotation", *The Physics of Fluids*, vol. 28, 1985.

[78] W. Stacey, R. Johnson, and J. Mandrekas, "A neoclassical calculation of toroidal rotation profiles and comparison with DIII-D measurements", *Physics of Plasmas*, vol. 13, 2006.

[79] J. Mandrekas, *Physics Models and User's Guide for the Neutral Beam Module of the SuperCode*, https://w3.pppl.gov/ntcc/NBEAMS/nbeams.pdf. Accessed: 09-03-2020.

[80] M. E. Austin *et al.*, "Achievement of Reactor-Relevant Performance in Negative Triangularity Shape in the DIII-D Tokamak", *Phys. Rev. Lett.*, vol. 122, 2019.

[81] D.-D. Team, "DIII-D Capabilities and Toolsfor Plasma Science Research", General Atomics, Tech. Rep., 2019.

[82] J.-P. Floyd, "Evolution of edge pedestal transport between ELMS in DIII-D", PhD thesis, Georgia Institute of Technology, 2014.

[83] D. R. Hatch *et al.*, "Direct gyrokinetic comparison of pedestal transport in JET with carbon and ITER-like walls", *Nuclear Fusion*, vol. 59, 2019.

[84] T. Onjun *et al.*, "Comparison of low confinement mode transport simulations using the mixed Bohm/gyro-Bohm and the Multi-Mode-95 transport model", *Physics of Plasmas*, vol. 8, 2001.

VITA

Jonathan J. Roveto was born in Fresno, California. After graduating from Edison High School in 2004, he enrolled at California State University - Fresno, better known as Fresno State, in Fresno, California. There, he earned a Bachelor's degree in Physics, graduating in 2008. He remained there and went on to achieve a Master' degree in Physics in 2010. His Master's thesis topic was a hotly debated subject at the time: entropic gravity. He also received the College of Science Graduate Student of the Year award in 2010. After completing his Master's degree, he taught at Lemoore Community College in Lemoore, California for a year. Upon acceptance to the Georgia Institute of Technology, better known as Georgia Tech, in Atlanta, Georgia, he began his time at the Fusion Research Center under Weston M. Stacey. He simultaneously worked on a DOD grant under Dr. Shodine. Upon completion of the grant, he began working full time as an academic editor while continuing his work at the Fusion Research Center helping develop the GTEDGE2 code. He received his Ph.D. in Nuclear Engineering with a specialization in Nuclear Enterprise Management in 2021.